

This is the accepted manuscript made available via CHORUS. The article has been published as:

## Higher-order corrections to timelike jets

W. T. Giele, D. A. Kosower, and P. Z. Skands

Phys. Rev. D **84**, 054003 — Published 6 September 2011

DOI: [10.1103/PhysRevD.84.054003](https://doi.org/10.1103/PhysRevD.84.054003)

# Higher-Order Corrections to Timelike Jets

W. T. Giele<sup>1</sup>, D. A. Kosower<sup>2</sup>, P. Z. Skands<sup>3</sup>

<sup>1</sup> Theoretical Physics, Fermilab, MS106, Batavia 60510-0500, USA

<sup>2</sup> Institut de Physique Théorique, CEA-Saclay, F-91191 Gif-sur-Yvette cedex, France

<sup>3</sup> Theoretical Physics, CERN, CH-1211 Geneva 23, Switzerland

## Abstract

We present a simple formalism for the evolution of timelike jets in which tree-level matrix element corrections can be systematically incorporated, up to arbitrary parton multiplicities and over all of phase space, in a way that exponentiates the matching corrections. The scheme is cast as a shower Markov chain which generates one single unweighted event sample, that can be passed to standard hadronization models. Remaining perturbative uncertainties are estimated by providing several alternative weight sets for the same events, at a relatively modest additional overhead. As an explicit example, we consider  $Z \rightarrow q\bar{q}$  evolution with unpolarized, massless quarks and include several formally subleading improvements as well as matching to tree-level matrix elements through  $\alpha_s^4$ . The resulting algorithm is implemented in the publicly available VINCIA plugin<sup>1</sup> to the PYTHIA8 event generator.

## 1 Introduction

The experimental program now underway at the Large Hadron Collider (LHC) will make extensive demands on theorists' ability to predict background processes, governed by Standard-Model physics. These predictions require perturbative computations in the electroweak sector, and call on both perturbative and nonperturbative physics in quantum chromodynamics. The dependence on nonfactorized and nonperturbative QCD is not yet amenable to a first-principles calculation, and must therefore rely on experimental measurements of the parton distribution functions, as well as models for hadronization and the underlying event. An appropriate choice of observables — infrared- and collinear-safe ones — can minimize (but not eliminate) the dependence on these models. The factorizable perturbative component of the backgrounds can be computed systematically.

An essential class of observables for new-physics searches are multi-jet differential cross sections, typically with events also required to include decay products of one or more electroweak vector bosons. Jet shapes and jet substructure observables are also important, both from a calibration point of view as well as to search for decays of boosted objects [1, 2]. The two basic approaches to computing perturbative contributions are via a fixed-order expansion in powers of the strong coupling  $\alpha_s$ , and in a parton-shower approach which resums leading (LL) and possibly next-to-leading logarithms (NLL) of large ratios of scales multiplying the strong coupling. The former approach can be carried out using widely-available tools to leading order (LO) in  $\alpha_s$  for essentially any jet multiplicity, for a growing list of processes to

---

<sup>1</sup>Available from the web site: <http://projects.hepforge.org/vincia/>

next-to-leading order (NLO), and for a select list to next-to-next-to-leading order (NNLO). It sacrifices a detailed picture of each event, and of jet substructure, in favor of a systematically improved description of the “hard” or wide-angle radiation reflected in the several jets. The parton-shower approach (see [3] for a recent review) favors developing an accurate picture of the “soft” or “collinear” radiation that dresses the hard event, thereby providing an event-by-event description of jet substructure as well as allowing the incorporation of a nonperturbative model for the final-state hadrons.

From a theoretical point of view, the two approaches correspond to summing up different but overlapping sets of contributions to the short-distance perturbative matrix elements. Simply adding the two would yield an overcounting of the common contributions, and the separation of the two sets is somewhat delicate. The recent decade has seen the appearance of a number of strategies for combining or “matching” these two approaches for general final states. These can be broadly described as “slicing”, “subtraction”, or “unitarity” approaches.

In a slicing approach, the phase space for multiple emissions is separated into two regions. In one, the calculation uses the leading-order matrix element; in the other, the leading-log approximation as given by a parton shower. The schemes introduced by Mangano (MLM) in the days of the top quark discovery and formalized later [4,5], and by Catani, Krauss, Kuhn, and Webber (CKKW) [6] are examples of a slicing approach. The CKKW approach has been implemented within the SHERPA framework [7]; the MLM one, using ALPGEN [8] interfaced [9, 10] to both PYTHIA [11] and HERWIG [12]. Refined versions of the CKKW method have since been introduced by Lönnblad [13, 14] in the context of the color-dipole model [15, 16] and implemented in the ARIADNE generator [17], as well as by Mrenna and Richardson [18] using MADGRAPH [19], again interfaced to HERWIG and PYTHIA. The original strategy [20, 21] for matching in HERWIG, for one emission beyond a basic process, also follows this approach and may be seen as a precursor to the CKKW formalism.

In a subtractive approach, the shower approximation is subtracted from the exact fixed-order matrix element, and two classes of events are generated: standard events and counter-events. The latter may have negative weights. The MC@NLO program built on HERWIG is an example of subtractive matching to one loop [22]. Other subtraction implementations include a SHERPA implementation [23] and one by Dinsdale, Ternick, and Weinzierl (DTW) [24] based on the Catani-Seymour (CS) method [25] of fixed-order calculations. Finally, the MENLOPS scheme [26] probably represents the most advanced current matching method, combining POWHEG (a unitarity-based variant of MC@NLO, see below) with a slicing-based matching for multijet emissions.

Note, however, that in both slicing and subtraction, any subleading divergencies in the matched matrix elements beyond one additional parton are not regulated by the (LL) shower, and hence all the multileg schemes — MLM, CKKW, and MENLOPS — are forced to introduce a “matching scale” below which only the pure LL shower is used. While such schemes therefore guarantee the rates of hard additional jets to be correct to LO, the same is not guaranteed for jet substructure, which can be explicitly sensitive to multiparton correlations below the matching scale and beyond LL [27].

In a unitarity approach, to maintain a sequence of unit-weight events, the selection of branching events is modified by a veto depending on the ratio of the exact matrix element to the shower approximation. Since the correction is applied on the splitting probability itself, it is automatically resummed to all orders by the shower Sudakovs, with real and virtual corrections canceling order by order in perturbation theory. Indeed, the original approach to matching, carried out for one additional emission beyond a basic process in PYTHIA [28, 29],

follows this approach. It is also used in POWHEG [30], there combined with a subtractive matching to NLO. The proposal of matching by Sudakov reweighting by Nagy and Soper [31] is also within this class. However, the unitary approach to matching has so far only been worked out for a single emission. We shall here generalize it to an arbitrary number of emissions, arriving at the equivalent to MENLOPS but based on unitarity instead of slicing for the additional emissions. This will allow us to extend the matching over all of phase space, and should therefore result in a more accurate modeling not only of jet rates but also of jet substructure.

Most showers, with the exception of ARIADNE and the Winter–Krauss shower [32], are based on collinear factorization, which is to say  $1 \rightarrow 2$  branching in shower evolution. (PYTHIA 8 combines a  $1 \rightarrow 2$  splitting probability with a  $2 \rightarrow 3$  phase-space mapping.) In the present paper, we continue the development of a leading-log (LL) parton shower [33] based on dipole antennæ, that is  $2 \rightarrow 3$  branching. We choose a simpler context than hadron collisions, that of electron–positron collisions. This allows us to set aside the questions of initial-state emission as well as those of the underlying event.

In sec. 2, we describe in greater detail the ingredients needed for such a shower, as well as our normalization conventions, and compare the origins of different singularities and corresponding logarithms in different shower formalisms. We also discuss the different matching approaches in more detail. In sec. 3, we discuss the evolution integral, and show how to cast it in a general form whose specializations correspond to a wide variety of interesting evolution variables. We then solve the resulting evolution equation. In sec. 4, we discuss the shower algorithm, as well as improvements that can be made to its logarithmic accuracy. In sec. 5, we discuss the details of matching the dipole-antenna shower to tree-level matrix elements, at both leading and subleading color. The procedure we use to evaluate the remaining perturbative uncertainties is described in sec. 6, and in sec. 7, we comment on hadronization; in sec. 8, we compare the results of running the unitarity-based approach implemented in VINCIA to LEP data and to PYTHIA 8. We make some concluding remarks in sec. 9.

## 2 Nomenclature and Conventions

In this section, we introduce the basic elements of our perturbative formalism, which is largely based on ref. [33]. First, in sec. 2.1, we illustrate how the KLN theorem may be used to rewrite the coefficients of perturbation theory as the expansion of an all-orders Markov chain, using NLO as an explicit example. Then, in sec. 2.2, we briefly describe each of the ingredients that enter our dipole-antenna shower formalism.

### 2.1 Perturbation Theory with Markov Chains

Consider the Born-level cross section for an arbitrary hard process,  $H$ , differentially in an arbitrary infrared-safe observable  $\mathcal{O}$ ,

$$\left. \frac{d\sigma_H}{d\mathcal{O}} \right|_{\text{Born}} = \int d\Phi_H |M_H^{(0)}|^2 \delta(\mathcal{O} - \mathcal{O}(\{p\}_H)) , \quad (1)$$

where the integration runs over the full final-state on-shell phase space of  $H$  (this expression and those below would also apply to hadron collisions were we to include integrations over the parton distribution functions in the initial state), and the  $\delta$  function projects out a 1-dimensional slice defined by  $\mathcal{O}$  evaluated on the set of final-state momenta which we denote

$\{p\}_H$  (without the  $\delta$  function, the integration over phase space would just give the total cross section, not the differential one).

To make the connection to parton showers, and to discuss all-orders resummations in that context, we may insert an operator,  $\mathcal{S}$ , that acts on the Born-level final state *before* the observable is evaluated, i.e.,

$$\left. \frac{d\sigma_H}{d\mathcal{O}} \right|_{\mathcal{S}} = \int d\Phi_H |M_H^{(0)}|^2 \mathcal{S}(\{p\}_H, \mathcal{O}) . \quad (2)$$

Formally, this operator — the evolution operator — will be responsible for generating all (real and virtual) higher-order corrections to the Born-level expression. The measurement  $\delta$  function appearing explicitly in eq. (1) is now implicit in  $\mathcal{S}$ . (Ultimately, non-perturbative corrections can also be included.)

Algorithmically, we shall cast  $\mathcal{S}$  as an iterative Markov chain, with an evolution parameter that formally represents the factorization scale of the event, below which all structure is summed over inclusively. As the Markov chain develops, the evolution parameter will go towards zero, and the event structure will become more and more exclusively resolved. A transition from a perturbative evolution to a non-perturbative one can also be inserted, at an appropriate scale, typically around 1 GeV. This scale thus represents the lowest perturbative scale that can appear in the calculations, with all perturbative corrections below it summed over inclusively.

It is instructive to begin by considering the first-order expansion the operator must have in order to agree with NLO perturbation theory,

$$\begin{aligned} \mathcal{S}^{(1)}(\{p\}_H, \mathcal{O}) &= \left( 1 + \frac{2\text{Re}[M_H^{(0)} M_H^{(1)*}]}{|M_H^{(0)}|^2} \right) \delta(\mathcal{O} - \mathcal{O}(\{p\}_H)) \\ &+ \int \frac{d\Phi_{H+1}}{d\Phi_H} \frac{|M_{H+1}^{(0)}|^2}{|M_H^{(0)}|^2} \delta(\mathcal{O} - \mathcal{O}(\{p\}_{H+1})) , \end{aligned} \quad (3)$$

with  $M_H^{(1)}$  the one-loop amplitude and the ratio  $d\Phi_{H+1}/d\Phi_H$  in the second line representing the phase space of one additional final-state particle; we shall return to the associated factorization below. The two correction terms are separately divergent and hence eq. (3) only has a symbolic formal meaning. It requires a regulator for actual calculations. Introducing the factorization scale mentioned above, and introducing an  $n+1 \rightarrow n$  mapping of momenta by summing inclusively over all emissions below it, we obtain, instead, the first-order expansion corresponding to an evolution from the starting scale,  $s$  (the c.m. energy squared), down to the scale  $Q_E^2$ ,

$$\begin{aligned} \mathcal{S}^{(1)}(\{p\}_H, s, Q_E^2, \mathcal{O}) &= \left( 1 + \frac{2\text{Re}[M_H^{(0)} M_H^{(1)*}]}{|M_H^{(0)}|^2} + \int_0^{Q_E^2} \frac{d\Phi_{H+1}}{d\Phi_H} \frac{|M_{H+1}^{(0)}|^2}{|M_H^{(0)}|^2} \right) \delta(\mathcal{O} - \mathcal{O}(\{p\}_H)) \\ &+ \int_{Q_E^2}^s \frac{d\Phi_{H+1}}{d\Phi_H} \frac{|M_{H+1}^{(0)}|^2}{|M_H^{(0)}|^2} \delta(\mathcal{O} - \mathcal{O}(\{p\}_{H+1})) , \end{aligned} \quad (4)$$

where the factorization scale,  $Q_E$  (a.k.a. the “evolution scale”), separates resolved from unresolved regions. This expression is well-defined if the functional form of  $Q_E$  properly separates singular from non-singular regions, i.e., is “infrared sensible” [34]. (Corrections to

this expression arising from scales below  $Q_E$  will be taken into account by eventually letting  $Q_E \rightarrow 0$ .) Due to the KLN theorem [35, 36], the real and virtual singularities must be equal and of opposite sign, thus we can rewrite

$$\frac{2\text{Re}[M_H^{(0)} M_H^{(1)*}]}{|M_H^{(0)}|^2} = K_H^{(1)} - \int_0^s \frac{d\Phi_{H+1}}{d\Phi_H} \frac{|M_{H+1}^{(0)}|^2}{|M_H^{(0)}|^2}, \quad (5)$$

where  $K_H^{(1)}$  is a non-singular function when the regulator is removed, allowing us to express eq. (4) as

$$\begin{aligned} \mathcal{S}^{(1)}(\{p\}_H, s, Q_E^2, \mathcal{O}) &= \left( 1 + K_H^{(1)} - \int_{Q_E^2}^s \frac{d\Phi_{H+1}}{d\Phi_H} \frac{|M_{H+1}^{(0)}|^2}{|M_H^{(0)}|^2} \right) \delta(\mathcal{O} - \mathcal{O}(\{p\}_H)) \\ &+ \int_{Q_E^2}^s \frac{d\Phi_{H+1}}{d\Phi_H} \frac{|M_{H+1}^{(0)}|^2}{|M_H^{(0)}|^2} \delta(\mathcal{O} - \mathcal{O}(\{p\}_{H+1})) . \end{aligned} \quad (6)$$

In this form, the NLO correction to the total cross section is given solely by the term  $K_H^{(1)}$ , with the remaining terms having been written in an explicitly unitary construction.

We can also rewrite the exact ratio  $|M_{H+1}|^2/|M_H|^2$  as a process-dependent term whose integral is non-singular, plus a sum over universal singular ones,

$$\frac{d\Phi_{H+1}}{d\Phi_H} \frac{|M_{H+1}^{(0)}|^2}{|M_H^{(0)}|^2} = \frac{d\Phi_{H+1}}{d\Phi_H} K_{H+1}^{(0)} + \sum_r \frac{d\Phi_{H+1}^{[r]}}{d\Phi_H} S_r, \quad (7)$$

where  $r$  runs over “radiators”, whose precise definition, such as partons or dipoles, depends on the chosen decomposition of the singular structures in  $|M_{H+1}|^2$ , and the superscript  $^{[r]}$  on the phase space factors indicate that each radiator may in principle be associated with a different phase space factorization.

By the simple rewritings above, we have now obtained a form of the expansion in which the singularity and unitarity structure of  $\mathcal{S}$  are both explicitly manifest. Deviations from unitarity are associated solely with the non-singular term  $K_H^{(1)}$ , and deviations from the universal radiation functions are associated solely with the non-singular term  $K_{H+1}^{(0)}$ . In both cases, the generalization to higher orders is straightforward.

In traditional parton showers, all the non-singular terms are dropped, and hence *only* the unitary singular structure remains,

$$\begin{aligned} \mathcal{S}^{(1)}(\{p\}_H, s, Q_E^2, \mathcal{O}) &= \left( 1 - \sum_r \int_{Q_E^2}^s \frac{d\Phi_{H+1}^{[r]}}{d\Phi_H} S_r \right) \delta(\mathcal{O} - \mathcal{O}(\{p\}_H)) \\ &+ \sum_r \int_{Q_E^2}^s \frac{d\Phi_{H+1}^{[r]}}{d\Phi_H} S_r \delta(\mathcal{O} - \mathcal{O}(\{p\}_{H+1})) . \end{aligned} \quad (8)$$

Exponentiating the leading singularities, we may replace them by the Sudakov factor,

$$\Delta(\{p\}, s, Q_j^2) = \exp \left[ - \sum_r \int_{Q_j^2}^s \frac{d\Phi_{H+1}^{[r]}}{d\Phi_H} S_r \right]. \quad (9)$$

We thereby obtain the all-orders pure-shower Markov chain,

$$\begin{aligned} \mathcal{S}(\{p\}_H, s, Q_E^2, \mathcal{O}) = & \underbrace{\Delta(\{p\}_H, s, Q_E^2) \delta(\mathcal{O} - \mathcal{O}(\{p\}_H))}_{H+0 \text{ exclusive above } Q_E} \\ & + \underbrace{\sum_r \int_{Q_E^2}^s \frac{d\Phi_{H+1}^{[r]}}{d\Phi_H} S_r \Delta(\{p\}_H, s, Q_{H+1}^2) \mathcal{S}(\{p\}_{H+1}, Q_{H+1}^2, Q_E^2, \mathcal{O})}_{H+1 \text{ inclusive above } Q_E} . \end{aligned} \quad (10)$$

The shower may exponentiate the entire set of universal singular terms, or only a subset of them (for example, the terms leading in the number of colors  $N_c$ ). More on the Markov formalism can be found in ref. [33]. We hope this brief introduction serves to put the developments below in context, and note that we will return to the restoration of the finite terms in the section on matching.

## 2.2 Dipole-Antenna Showers

In leading-log dipole-antenna showers, the fundamental step is a Lorentz invariant  $2 \rightarrow 3$  branching process by which two on-shell “parent” partons are replaced by three on-shell “daughter” partons. This  $2 \rightarrow 3$  process makes use of three ingredients:

1. An *antenna function* that captures the leading tree-level singularities of QCD matrix elements. This is the equivalent of the splitting functions used in traditional parton showers, with some important differences, as we discuss below.
2. A *kinematics map*, specifying how the post-branching momenta are related to the pre-branching ones. This is the equivalent of the “recoil strategy” of traditional parton showers.
3. An antenna *phase space* — an exact, momentum-conserving and Lorentz-invariant factorization of the pre- and post-branching phase spaces. Traditional parton showers, on the other hand, are based on a phase-space factorization which is only exact in the collinear limit, and momentum conservation may only be imposed *a posteriori*.

In the following paragraphs, we present the notation and normalization conventions that we shall use in the rest of the article for each of these pieces.

**Factorization:** Labeling the three daughter partons  $i$ ,  $j$ , and  $k$ , we write the integral over a three-body matrix element corresponding to that final state in factorized form as follows,

$$|M_3(p_i, p_j, p_k)|^2 d\Phi_3 = |M_2(s)|^2 d\Phi_2 \frac{|M_3(p_i, p_j, p_k)|^2 d\Phi_3}{|M_2(s)|^2 d\Phi_2} , \quad (11)$$

where the two-parton matrix element we have introduced corresponds to the “parent” configuration, in which we label the partons  $I$  and  $K$ . The branching process represented by this factorization is thus  $IK \rightarrow ijk$ , with total Lorentz invariant  $s_{ijk} = s_{IK} = s$ . The  $|M_3|^2/|M_2|^2$  factor in eq. (11) represents the evolution kernel, whose (negative) exponential is the Sudakov form factor, cf. eq. (9).

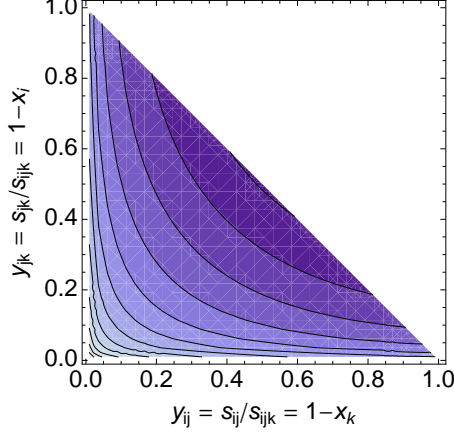


Figure 1: Contours of constant value of the antenna function,  $\bar{a}_{ijk}^0$  for  $q\bar{q} \rightarrow qg\bar{q}$  derived from  $Z$  decay as function of the two phase-space invariants, with an arbitrary normalization and a logarithmic color scale. Larger values are shown in lighter shades. The (single) collinear divergences sit on the axes, while the (double) soft divergence sits at the origin.

**Phase Space:** The dipole-antenna *phase-space measure* is thus [33]

$$\frac{d\Phi_3}{d\Phi_2} = ds_{ij} ds_{jk} \frac{d\phi}{2\pi} \frac{1}{16\pi^2 \sqrt{\lambda(s, m_I^2, m_K^2)}} , \quad (12)$$

where the Källén function,

$$\lambda(s, m_I^2, m_K^2) = s^2 + m_I^4 + m_K^4 - 2sm_I^2 - 2sm_K^2 - 2m_I^2m_K^2 , \quad (13)$$

in the denominator reduces to  $\sqrt{\lambda} = s$  for massless particles.

**Antenna Function:** The ratio of matrix elements appearing in the integrand of eq. (11) is then decomposed into a symmetry factor, a coupling factor, a color factor, and an *antenna function*,

$$\frac{|M_3(p_i, p_j, p_k)|^2}{|M_2(s)|^2} = S_{IK \rightarrow ijk} g^2 \mathcal{C}_{ijk} \bar{a}_{ijk}^0(s, s_{ij}, s_{jk}) , \quad (14)$$

where  $S$  takes into account potential identical-particle factors as well as the possible presence of more than one antenna in the parent ( $IK$ ) configuration,  $g^2$  is the relevant coupling factor,  $\mathcal{C}_{ijk}$  is a color factor, and  $\bar{a}_{ijk}^0$  is a generic color- and coupling-stripped dipole-antenna function, with superscript 0 to denote a tree-level quantity. The three-particle matrix element is averaged azimuthally (over  $\phi$ ). Note that our use of lower-case letters for the antenna function is intended to signify that it corresponds to what is called a *sub-antenna* in ref. [37] for which lower-case letters are likewise used<sup>2</sup>.

For illustration, contours of constant value of  $\bar{a}_{qg\bar{q}}^0(s, s_{qg}, s_{g\bar{q}})$  as derived from  $Z$  decay are shown in fig. 1, over the  $2 \rightarrow 3$  phase space, with an arbitrary normalization and a logarithmic

<sup>2</sup>Thus, in the notation of ref. [37], our dipole-antenna functions would be  $\bar{a}_3^0 = A_3^0$ ,  $\bar{d}_3^0 = d_3^0$ ,  $\bar{e}_3^0 = \frac{1}{2}E_3^0$ ,  $\bar{f}_3^0 = f_3^0$ , and  $\bar{g}_3^0 = \frac{1}{2}G_3^0$ .



color scale. This function is called  $A_3^0$  in ref. [37] and is identical to the radiation function used for  $q\bar{q} \rightarrow qg\bar{q}$  splittings in ARIADNE. One clearly sees the large enhancements towards the edges of phase space, with a double pole (the overlap of two singularities, usually called soft *and* collinear) sitting at the origin, and single singularities (soft *or* collinear) localized on the axes.

Writing the coupling factor as  $g^2 = 4\pi\alpha_s$  and combining it with the phase space factor, eq. (12), we have the following antenna function normalization

$$a_{IK \rightarrow ijk}^0(s, s_{ij}, s_{jk}) \equiv \frac{1}{\sqrt{\lambda(s, m_I^2, m_K^2)}} \frac{\alpha_s}{4\pi} C_{ijk} \bar{a}_{ijk}^0(s, s_{ij}, s_{jk}) . \quad (15)$$

That is, we use the notation  $\bar{a}$  for the coupling- and color-stripped antenna function, and the notation  $a$  for the “dressed” antenna function, i.e., including its coupling, color, and phase-space prefactors.

Note that  $g^2 \times (\text{phase-space normalization})$  leads to a factor  $\alpha_s/(4\pi)$  independently of the type of branching. As we believe that the formalism becomes more transparent if the origin of each factor is kept clear throughout, we shall therefore use this factor for *all* branchings, instead of the more traditional convention of using  $\alpha_s/(2\pi)$  for some branchings and  $\alpha_s/(4\pi)$  for others. Obviously, this convention choice will be compensated by our conventions for the color factors and antenna-function normalizations, such that the final result remains independent of this choice.

**Color Factor:** For color factors, we shall systematically adopt a convention optimized for shower applications, in which the color factor tends to  $N_C$  in the large- $N_C$  limit whenever a new color line is created (rather than to  $N_C/2$  as is the case for  $C_F$  in the standard normalization) and to unity when no new color lines are created (rather than  $1/2$  which is the case for  $T_R$  in the standard normalization). That is, we shall use

$$C_A = N_C = 3 , \quad (16)$$

$$\hat{C}_F = \frac{N_C^2 - 1}{N_C} = 8/3 = 2C_F , \quad (17)$$

$$\hat{T}_R = 1 = 2T_R . \quad (18)$$

With all other normalizations fixed, the normalization of the antenna functions is now also unique. Indeed, with this choice, the radiation functions will turn out to be normalized in a way that makes their similarities more readily apparent. Another useful thing about this normalization is that the color factors now have a very simple interpretation. They provide a one-to-one count of the number of new color degrees of freedom that have been summed over in any given process. This gives a simpler counting and interpretation than in the standard normalization. Of course, the fact that there are only  $N_C^2 - 1 = 8$  gluons, leads to corrections of order  $1/N_C^2$ , and here again it is trivial to let the “naïve” color-line creation factor  $C_A$  be replaced by  $\hat{C}_F$  for, e.g.,  $q\bar{q} \rightarrow qg\bar{q}$ , without artificially having to compensate by a factor of 2 in the radiation function — the eikonal part of the radiation function now remains invariant (as noted above in the discussion of the normalization of the radiation functions), and the difference in color factor is explicitly subleading, as it should be. A final argument is the question of which color factor to use, e.g., for a  $qg \rightarrow qgg$  emission. In the standard normalization, this could lead to confusion, since one parent would seem to “want”  $C_F$  and

the other  $C_A$ , which differ by a more than a factor of 2. In the normalization used here, the difference between  $\hat{C}_F$  and  $C_A$  is explicitly subleading in color, and hence it is clear that either of them could be used without any possibility for ambiguity at the leading-color (LC) level, again placing the proper difference in the proper place.

To preempt confusion and illustrate how simple the translation between these convention choices is, consider the dipole-antenna function for gluon emission off a  $q\bar{q}$  pair used in the ARIADNE generator [17]. As the symmetry factor is unity, this is just the matrix element squared for  $Z \rightarrow 3$  divided by the one for  $Z \rightarrow 2$  multiplied by the aforementioned phase-space factor,

$$\frac{|M(Z \rightarrow qg\bar{q})|^2}{16\pi^2 s |M(Z \rightarrow q\bar{q})|^2} = \frac{1}{s} \frac{2\alpha_s}{3\pi} \frac{(1 - y_{ij})^2 + (1 - y_{jk})^2}{y_{ij}y_{jk}}, \quad (19)$$

where  $y_{ij} = s_{ij}/s = 1 - x_k$ . The factor  $2\alpha_s/(3\pi)$  in the first equation can be rewritten in two ways

$$\frac{2\alpha_s}{3\pi} = \frac{4}{3} \frac{\alpha_s}{2\pi} = C_F \frac{\alpha_s}{2\pi} \quad \text{or} \quad \frac{2\alpha_s}{3\pi} = \frac{8}{3} \frac{\alpha_s}{4\pi} = \hat{C}_F \frac{\alpha_s}{4\pi}; \quad (20)$$

it is purely for our own convenience that we choose the latter normalization.

In a similar vein one could rewrite the DGLAP splitting kernels [38], which are used in traditional parton showers [11, 12, 39, 40], as

$$\frac{P_{qI \rightarrow q_i g_j}^0(z)}{s_{ij}} = \frac{1}{s_{ij}} \frac{\alpha_s}{2\pi} C_F \frac{1+z^2}{1-z} = \frac{1}{s} \frac{\alpha_s}{4\pi} \hat{C}_F \frac{1+z^2}{y_{ij}(1-z)}, \quad (21)$$

$$\frac{P_{gI \rightarrow g_i g_j}^0(z)}{s_{ij}} = \frac{1}{s_{ij}} \frac{\alpha_s}{2\pi} N_C \frac{(1-z(1-z))^2}{z(1-z)} = \frac{1}{s} \frac{\alpha_s}{4\pi} 2N_C \frac{(1-z(1-z))^2}{y_{ij}z(1-z)}, \quad (22)$$

where the gluon radiation function has absorbed a factor of 2 on the r.h.s. of the last line, due to the normalization choice. We note that, although these expressions look quite different from the dipole formula, eq. (19), they lead to identical singularities. This was shown in ref. [29] by identifying  $z$  as the Lorentz invariant energy fraction taken by the quark,  $z = x_i/(x_i + x_k)$ , and adding the radiation from the antiquark,  $\bar{q}_K \rightarrow g_j \bar{q}_k$ .

**Shared Singularities:** This examination of the different presentations of singularities brings us to the issue of “shared singularities”. In traditional parton showers, as we have just seen, the full leading-log radiation pattern can only be obtained after summing over pairs of partons (which each radiate as independent monopoles), and care must be taken in the construction of the shower to make this sum approximately coherent to reproduce the correct singular behavior for soft wide-angle radiation. This *dipole* singularity is the simplest case of what we shall generally refer to as a shared — or multipole — singularity below; radiation whose full singularity structure (in a particular phase-space limit) can only be recovered after summing over two or more radiators.

A chain of such uniquely labeled and color ordered gluons, which could, e.g., represent a shower “event record” at a given point during its evolution, is illustrated in fig. 2. Below the schematic drawing we give an overview of how the full collinear singularity of parton  $I$ , and the full soft singularity of the  $IK$  pair, would be obtained for five different kinds of parton shower models, as follows.

In a traditional parton shower, the full collinear singularity of each parton is contained in the DGLAP splitting kernel,  $P(z)$ , that generates radiation off that parton. Since no other

	Coll( $I$ )	Soft( $IK$ )
<i>Parton Shower (DGLAP)</i>	$a_I$	$a_I + a_K$
<i>Coherent Parton Shower (HERWIG [12, 41], PYTHIA6 [11])</i>	$\Theta_I a_I$	$\Theta_I a_I + \Theta_K a_K$
<i>Global Dipole-Antenna (ARIADNE [17], GGG [37], WK [32], VINCIA)</i>	$a_{IK} + a_{HI}$	$a_{IK}$
<i>Sector Dipole-Antenna (LP [42], VINCIA)</i>	$\Theta_{IK} a_{IK} + \Theta_{HI} a_{HI}$	$a_{IK}$
<i>Partitioned-Dipole Shower (SK [23], NS [43], DTW [24], PYTHIA8 [39], SHERPA)</i>	$a_{I,K} + a_{I,H}$	$a_{I,K} + a_{K,I}$

	Coll( $I$ )	Soft( $IK$ )
<i>Parton Shower (DGLAP)</i>	$a_I$	$a_I + a_K$
<i>Coherent Parton Shower (HERWIG [12, 41], PYTHIA6 [11])</i>	$\Theta_I a_I$	$\Theta_I a_I + \Theta_K a_K$
<i>Global Dipole-Antenna (ARIADNE [17], GGG [37], WK [32], VINCIA)</i>	$a_{IK} + a_{HI}$	$a_{IK}$
<i>Sector Dipole-Antenna (LP [42], VINCIA)</i>	$\Theta_{IK} a_{IK} + \Theta_{HI} a_{HI}$	$a_{IK}$
<i>Partitioned-Dipole Shower (SK [23], NS [43], DTW [24], PYTHIA8 [39], SHERPA)</i>	$a_{I,K} + a_{I,H}$	$a_{I,K} + a_{K,I}$

Figure 2: Schematic overview of how the full collinear singularity of parton  $I$  and the soft singularity of the  $IK$  pair, respectively, originate in different shower types. ( $\Theta_I$  and  $\Theta_K$  represent angular vetos with respect to partons  $I$  and  $K$ , respectively, and  $\Theta_{IK}$  represents a sector phase-space veto, see text.)

radiators share that collinear direction, there is no double counting at the LL level. (The kernel  $P(z)$  constitutes a complete subtraction term for the collinear singularities in real-emission contributions to an NLO calculation.) However, in this approach, the soft (eikonal) singularity between the  $IK$  pair must be obtained by summing the radiation functions of partons  $I$  and  $K$  together, and therefore it is essential in this type of approach that both the radiation functions and the shower phase-space factorization represent a correct partitioning of the soft region, with no so-called dead or double-counted zones.

In the early eighties it was shown [41] that additional coherence effects can also be taken into account in this language, albeit approximately, by imposing angular ordering during shower evolution. This effectively represents a first step towards treating color-connected partons as multipoles in the shower context; partons  $I$  and  $K$  now effectively acquire some knowledge of each other, via their relative opening angle, and hence they no longer act as completely independent emitters. This improvement is denoted “Coherent Parton Showers” in the table in fig. 2. As indicated by the appearance of the  $\Theta$  function in the collinear term in such approaches, it is important to construct the angular ordering in such a way that the effect of the veto disappears in the collinear limit.

In this paper, we follow the dipole-antenna approach to color coherence. This is motivated by the observation that, whereas the collinear singularities are associated with single

logarithms, the parametrically larger double logarithms arise from soft (eikonal) factors. It therefore makes sense to change the underlying picture to a dual one in which parton *pairs* are the fundamental entities. Such pairs appear in the fixed-order literature under the name of *antennæ* and in the shower one, under the name of *dipoles*. The latter term, however, usually means something else again in the fixed-order literature. To avoid confusion, we therefore call these pairs *dipole-antennæ*. In this picture, the roles of soft and collinear singularities are interchanged, with respect to the parton picture. The soft double logarithms between neighboring partons now come from a single term, which is thus guaranteed to be neither over- nor under-counted as no other pairs become doubly singular in the same phase-space region. The single logarithmic *collinear* radiation off a given gluon must now be partitioned among the two neighboring antennæ that share it. (Note that quarks are still unambiguous in this picture.) The gluon case is represented by the line labeled “Global Dipole-Antenna” in the table in fig. 2.

There is considerable freedom in how to partition the collinear radiation, because terms can be shuffled back and forth “across the gluon” while maintaining their sum constant. Two convenient examples are furnished by ARIADNE [17] and by Gehrmann et al. (GGG) [37], which use different decompositions (see ref. [42] for some additional discussion of this point).

The first important point concerns what to compare; obviously, the individual shower functions differ by collinear singular terms. Thus, if we naively subtract the ARIADNE functions for  $qg \rightarrow qgg$  and  $gg \rightarrow ggg$  [17] from the corresponding GGG ones<sup>3</sup> [37], we obtain

$$\begin{aligned}\delta_{\text{GGG-AR}}^{qg} &= \frac{1}{s} \left( \frac{2y_{ik}}{y_{ij}y_{jk}} + \frac{y_{ij}y_{ik}}{y_{jk}} + \frac{y_{ik}y_{jk} + y_{jk}^2}{y_{ij}} + \frac{5}{2} + \frac{1}{2}y_{jk} \right) - \frac{1}{s} \left( \frac{(1-y_{ij})^3 + (1-y_{jk})^2}{y_{ij}y_{jk}} \right) \\ &= \frac{1}{s} \left( \frac{1-2y_{ij}}{y_{jk}} - y_{ij} + \frac{5}{2} - \frac{1}{2}y_{jk} \right),\end{aligned}\tag{23}$$

$$\begin{aligned}\delta_{\text{GGG-AR}}^{gg} &= \frac{1}{s} \left( \frac{2y_{ik}}{y_{ij}y_{jk}} + \frac{y_{ij}y_{ik}}{y_{jk}} + \frac{y_{jk}y_{ik}}{y_{ij}} + \frac{8}{3} \right) - \frac{1}{s} \left( \frac{(1-y_{ij})^3 + (1-y_{jk})^3}{y_{ij}y_{jk}} \right) \\ &= \frac{1}{s} \left( \frac{1-2y_{jk}}{y_{ij}} - y_{ij} + \frac{1-2y_{ij}}{y_{jk}} - y_{jk} + \frac{8}{3} \right),\end{aligned}\tag{24}$$

which differ by gluon-collinear singular terms. However, when we sum over the two possible orderings of the gluons in eq. (23) and the three orderings in eq. (24), the discrepancies become collinear-finite,

$$\Delta_{\text{GGG-AR}}^{qg} = \delta_{\text{GGG-AR}}^{qg} + (j \leftrightarrow k) = \frac{6}{s},\tag{25}$$

$$\Delta_{\text{GGG-AR}}^{gg} = \delta_{\text{GGG-AR}}^{gg} + (j \leftrightarrow k) + (i \leftrightarrow j) = \frac{12}{s}.\tag{26}$$

We see that, once summed over permutations, the ARIADNE functions have substantially smaller finite terms than the GGG ones. The ARIADNE shower is accordingly somewhat softer than the default VINCIA one, which uses the GGG functions, but the singular terms

---

<sup>3</sup>Note that, in the shower context, different color orderings of the final state are represented as separate events, wherefore the shower function should only contain *one* of the permutations, corresponding to what GGG label a *sub-antenna*.

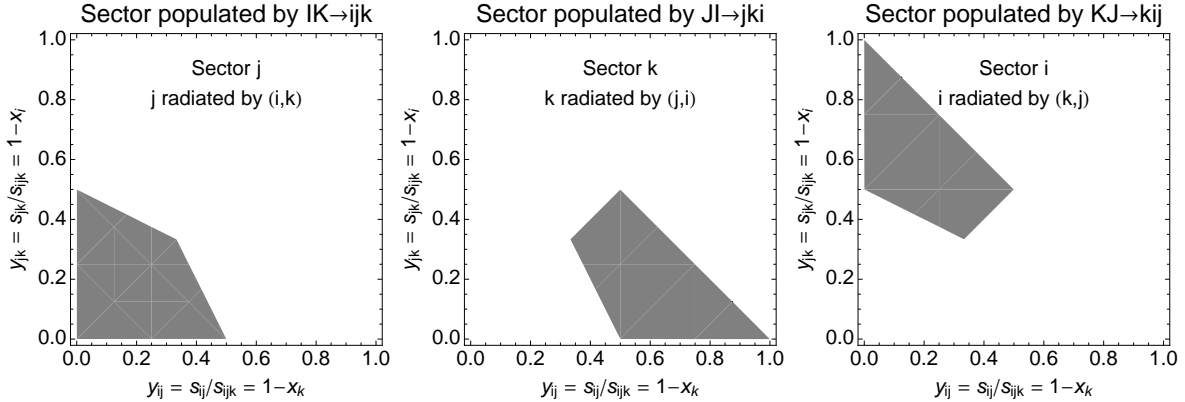


Figure 3: The three phase-space sectors in a color-singlet  $g_i g_j g_k$  configuration, using  $p_\perp$  as the discriminator for which sector a given emission/clustering/history belongs to.

are the same, in spite of the apparently singular differences between the individual shower functions.

We shall usually choose the partitioning of GGG, which makes the collinear terms of the gluon antennae appear almost identical to those involving quarks in our parametrization, thus emphasizing their similarities. Note that for shower applications, the partitioning must be done in such a way that the resulting shower functions are positive definite. This is indeed the case for all the functions we consider in this paper — a counter example is given in ref. [44], where the positive-definite ARIADNE antenna functions are repartitioned à la GGG in a way that introduces negative regions in the individual  $gg \rightarrow ggg$  shower functions, while maintaining their sum constant.

A different approach to the issue of how to partition the collinear singularities is to retain the full collinear singularity of the gluon in *both* of the neighbouring antennae, and combine this with phase-space vetos that allow only one or the other antenna to contribute to each given phase-space point, a possibility we have labeled “Sector Dipole-Antenna” in the table in fig. 2. The distinction between global and sector antennae is thus that in the former, several antennae (two that are singular, and possibly more that are non-singular) are summed over all of phase space, in a way such that their *sum* reproduces the full collinear singularity, and in the latter case every single term contains the full singularities, but only one term (the most singular) is allowed to contribute to any given phase-space point. An illustration of the sectors appropriate to one color ordering in the decay of a scalar,  $H^0 \rightarrow g_a g_r g_b$ , is given in fig. 3. This approach has been suggested for use in NLO fixed-order calculations, and can be used with VINCIA as well. Larkoski and Peskin (LP) [42] have also considered these kinds of antennae, including polarization effects.

Finally, a different approach, which also treats dipole coherence exactly, consists of systematically partitioning both the soft and collinear singularities of  $I$  and  $K$  into four terms, two of which treat parton  $I$  as the emitter, with  $K$  and  $H$  acting as spectator/recoiler, respectively, and the other two terms treating parton  $K$  as the emitter, now with partons  $I$  and  $L$  acting as spectator/recoiler, respectively. Catani and Seymour [25, 45] labeled this a *dipole* model, but as this usage differs from an older use of the term dipole in parton-shower calculations to describe the sum of two such terms (in the context of the Lund dipole [15, 16]),

we avoid confusion by referring to the CS type as a *partitioned-dipole* shower and to the Lund-dipole/antenna type as a *dipole-antenna* shower. In the case of partitioned dipoles, the radiation off parton  $I$  is split into two terms (“sides”), each of which contains “half” of the collinear singularity of parton  $I$  and “half” of the soft singularity with either of the neighboring partons, e.g.,

$$a_{I,K} = \frac{1}{2}\text{Coll}(I) + \frac{1}{2}\text{Soft}(IK) , \quad (27)$$

where the subscripts are intended to denote that this is the term for  $I$  emitting and  $K$  recoiling. There are thus a total of 4 radiation functions involving partons  $I$  and  $K$ , but these terms can now all be constructed explicitly so as to have the correct limiting behaviors. Obviously, there is some ambiguity concerning which functional form to choose for how to divide up the radiation among the various terms, which is why “half” is in quotation marks. Recently, Nagy and Soper (NS) presented a proposal [46] for turning the CS subtraction scheme into a parton shower; several groups have since developed CS-style showers, most notably Dinsdale, Ternick, and Weinzierl [24] and the SHERPA group [23]. Although not based on the CS formalism, we note that the  $p_\perp$ -ordered showers in PYTHIA 8 are also closely related to this approach.

**Kinematics Map:** The *kinematics map* specifies the details of how to reconstruct the parent momenta  $IK$  from the daughter momenta  $ijk$  and is equivalent to what is referred to as the “recoil strategy” in parton shower language. In an old-fashioned parton shower [47], or a Catani-Seymour one [23–25, 31, 46], for instance, the recoil strategy usually implies classifying either  $I$  or  $K$  as the *emitter* and the other as the *recoiler*, with the recoiler being constrained to experience a momentum change only along its direction of motion in some frame (e.g., the rest frame of the emitter + recoiler), say,  $p_i||p_I$ . In dipole-antenna approaches,  $I$  and  $K$  can be allowed to share the emitter/recoiler roles more smoothly over the resolved parts of phase space, with a clear distinction only being made in the strictly singular limits.

In principle, allowing recoils also outside the  $2 \rightarrow 3$  process itself, i.e., involving other partons than  $I$  and  $K$ , could be imagined, as long as the leading singular limits are respected. This would change the subleading properties of the resulting shower approach, which might be deemed desirable in some contexts, although it of course would not alter the formal level of precision. However, it does make the formalism more cumbersome, and hence we shall here restrict our attention to “local” recoil strategies, i.e., involving only the partons  $I$  and  $K$ . With this restriction in mind, the constraints that must be fulfilled to obey the singular limits and viable functional forms the kinematics map were discussed in refs. [17, 33, 37, 48, 49] (including  $2 \rightarrow n$  generalizations in refs. [48, 49]).

For illustration, fig. 4 shows the branching phase space together with examples of the orientation of the post-branching partons in the CM of the branching antenna for various phase-space points, using an antenna-like kinematics map, the “ARIADNE angle”, according to which the two parents share the transverse component of recoil. We shall return to kinematics maps later, but for the present merely note that the difference between an emitter-recoiler picture and the map used in fig. 4 is just an overall rotation (about an axis perpendicular to the paper), which vanishes in the soft and collinear limits.

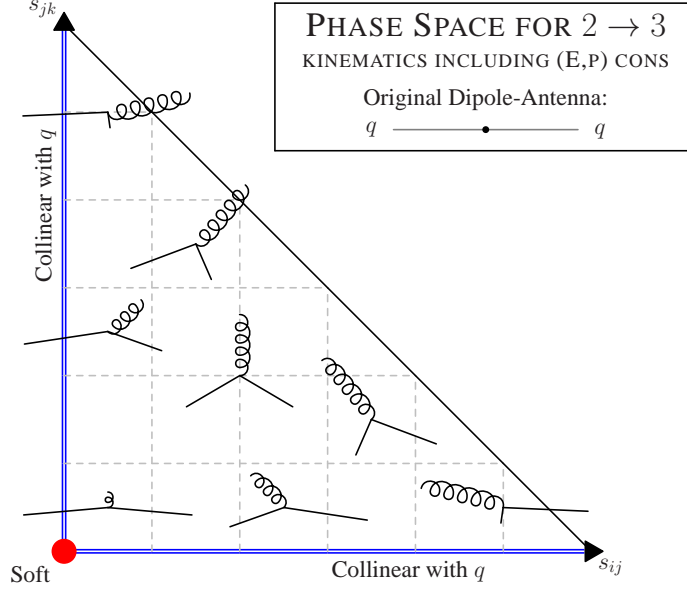


Figure 4: Illustration of the branching phase space, eq. (12), for  $q\bar{q} \rightarrow qg\bar{q}$ , with the original dipole-antenna oriented horizontally, an antenna-like kinematics map (the “ARIADNE angle”) in which the two parents share the transverse component of recoil, and  $\phi$  chosen such that the gluon is radiated upwards.

### 3 A Shower Generator Based on Dipole-Antennæ

A parton shower algorithm can be constructed from knowledge of the Sudakov form factor  $\Delta(Q_{E1}^2, Q_{E2}^2)$  representing the probability that no branching occurs between the scales  $Q_{E1}^2$  and  $Q_{E2}^2$ . The Sudakov form factor is in turn given by the exponential of a branching integral,

$$\Delta = \exp(-\mathcal{A}), \quad (28)$$

where, following the conventions laid down in the previous section, the integral  $\mathcal{A}$  of an antenna function over the  $2 \rightarrow 3$  antenna phase space is

$$\mathcal{A} = \int ds_{ij} ds_{jk} \frac{\alpha_s \mathcal{C}_{ijk} \bar{a}(s, s_{ij}, s_{jk}, m_i^2, m_j^2, m_k^2)}{4\pi \sqrt{\lambda(s, m_i^2, m_k^2)}} \stackrel{m \rightarrow 0}{=} \int ds_{ij} ds_{jk} a(s, s_{ij}, s_{jk}). \quad (29)$$

(We have suppressed the trivial integration over  $\phi$ .) Here, we have set all masses to zero, which approximation we adopt throughout this paper. Performing such integrals over all of phase space yields exactly the subtraction terms used in antenna-based fixed-order calculations, see, e.g., ref. [37]. (If the approach relies on phase-space vetos, such as in the case of sector antennæ, we can treat these as step functions that are part of the antenna function  $a$ , so that eq. (29) remains valid). Within the shower algorithm, we need to evaluate the integral for a range of scales, and then invert the function to write the lower scale as a function of the Sudakov form factor. The two-dimensional nature of the integral means that we have to define



coordinates, of which one will be the evolution scale of the shower. We can use this to our advantage, as we will see below, to allow for a number of different evolution variables within the same formalism. A functional inversion that is both flexible and efficient is accomplished by first using a simple overestimate of the antenna function, and then vetoing to obtain the exact result.

### 3.1 The Evolution Integral

In eq. (29) we left the integration boundaries unspecified. For showering purposes, what is needed is not the integral over the entire phase space, but over a region bounded by two values of the *evolution variable*,

$$\mathcal{A}(s, Q_{E1}^2, Q_{E2}^2) = \int_{Q_{E2}^2}^{Q_{E1}^2} ds_{ij} ds_{jk} a(s, s_{ij}, s_{jk}) \quad ; \quad Q_{E2}^2 < Q_{E1}^2, \quad (30)$$

which represents the integrated tree-level splitting probability when going *from* the scale  $Q_{E1}$  *to* the (lower) scale  $Q_{E2}$ . This is the fundamental building block which we shall later exponentiate and invert in order to find the evolution equation, but first we need to recast it so that the evolution variable appears explicitly as an integration variable.

We do this by a change of variables from the original invariants to a new set, one of which is the evolution variable,  $Q_E$ , and the other we may label  $\zeta$ , since it will play a role similar to, but not identical with, that of the  $z$  variable of traditional collinear-based shower algorithms. That is, our generic evolution integral will have the form

$$\mathcal{A}(s, Q_{E1}^2, Q_{E2}^2) = \int_{Q_{E2}^2}^{Q_{E1}^2} dQ_E^2 d\zeta |J| a(s, s_{ij}, s_{jk}), \quad (31)$$

where  $|J|$  is the Jacobian associated with the transformation from  $(s_{ij}, s_{jk})$  to  $(Q_E^2, \zeta)$ .

One immediate difference between our approach and traditional collinear-based formalisms is that there is here no explicit dependence on the precise definition of  $\zeta$ ; it merely serves to (re)parametrize phase space, and from a set of generated  $(Q_E^2, \zeta)$ , the set of invariants  $(s_{ij}, s_{jk})$  may be obtained without ambiguity. By contrast, in classic parton-shower approaches one would usually start from the collinear-limit splitting functions  $P(z)$  or similar objects, and since these are only accompanied by an unambiguous definition of  $z$  in the collinear limit, the precise definition of  $z$  away from this limit (energy or light-cone momentum fraction? in which frame? with finite-momentum recoils?) results in an ambiguity which is not present in our treatment.

There *is* of course a dependence on the functional form of  $Q_E$ , which formally enters starting from second order in the expansion for an IR safe observable (for IR sensitive ones,  $Q_E$  is needed as a regulator already at first order). Much effort has gone into debating and examining the vices and virtues of individual choices. Our stance is to order preferably in the inverse of the radiation function, since it is the singularities of this function which drive the logarithms; i.e., in  $p_\perp$  for gluon emission and in the invariant  $m_{q\bar{q}}$  for gluon splitting to  $q\bar{q}$ . Here, however, since we start directly from eq. (30), the phase-space factorization expressed in eq. (12) is preserved for *any* choice of  $Q_E$  and  $\zeta$ , and so rather than restrict ourselves to one specific form, we may instead seek a general solution to the evolution integral which will apply to a continuous class of Lorentz invariant evolution variables. By varying this unphysical parameter (which effectively amounts to changing the factorization scheme since the evolution



variable is what separates “resolved” from “unresolved” parts of the calculation at any given stage of the evolution) we obtain an estimate of the amount of scheme dependence which is generated by this variable — a dependence that higher-order matching will explicitly reduce, as we shall see below. The remaining variation can then be interpreted as an uncertainty estimate.

We stress that we here only give the *possibility* to vary this choice — further studies would be required to determine what a sensible *range* of variation would be, in the context of uncertainty estimates, in the same way that one discusses variations of other unphysical parameters for uncertainty estimates. The latter is obviously an art, not an exact science, but an art for which we can at least furnish the tools.

### 3.2 Trial Functions

To simplify the equations, we shall make use of the veto algorithm to replace the integrand,  $a$ , by a simpler function,  $a_{\text{trial}}$ , which we shall call the “trial function”. Provided our trial function is larger than the actual integrand, the veto algorithm will allow us to recover the exact integral post facto, and if the overestimates are not extremely wild, only a small loss of efficiency should result. We will choose the trial function to have the same leading (double) singularities as the full antenna function. It will thus provide us with a simple Lorentz-invariant phase-space generator which is pre-weighted to take into account these leading double-logarithmic singularities of QCD; we may then reweight back down to more exact expressions efficiently. These more exact expressions may be complete matrix elements or dipole-antenna splitting functions, depending on what is available at a given order in perturbation theory. The overestimating function we shall use for all branchings is the following, with a normalization depending on whether the trial process is gluon emission or gluon splitting to  $q\bar{q}$ ,

$$a_{\text{trial-emit}} = \frac{\hat{\alpha}_s}{4\pi s_{ijk}} C_A \quad \bar{a}_{\text{trial-emit}} = \frac{\hat{\alpha}_s}{4\pi s_{ijk}} C_A \frac{2s_{ijk}}{s_{ij}s_{jk}} \quad \begin{cases} q\bar{q} \rightarrow qg\bar{q} \\ qg \rightarrow qgg \text{ \& c.c.} \\ gg \rightarrow ggg \end{cases} \quad (32)$$

$$a_{\text{trial-split}} = \frac{\hat{\alpha}_s}{4\pi s_{ijk}} n_f \hat{T}_R \quad \bar{a}_{\text{trial-split}} = \frac{\hat{\alpha}_s}{4\pi s_{ijk}} n_f \hat{T}_R \frac{s_{ijk}}{s_{ij}s_{jk}} \quad \begin{cases} qg \rightarrow q\bar{q}'q' \text{ \& c.c.} \\ gg \rightarrow g\bar{q}q + \bar{q}qg \end{cases} \quad (33)$$

where  $n_f$  is the number of kinematically accessible flavours and  $\hat{\alpha}_s$  is a parameter representing a “trial”  $\alpha_s$ ; it should be greater than or equal to the latter. We will explain its use further in sec. 4. For comparison, the Eikonal (soft) approximation for gluon emission is

$$\bar{S}_{\text{emit}}(s, s_{ij}, s_{jk}) = \frac{2(s - s_{ij} - s_{jk})}{s_{ij}s_{jk}} = \frac{s - s_{ij} - s_{jk}}{s} \bar{a}_{\text{trial-emit}}(s, s_{ij}, s_{jk}) , \quad (34)$$

such that our approximation coincides with the Eikonal in the soft limit,  $s_{ij} \rightarrow 0$  and  $s_{jk} \rightarrow 0$ , and is larger than the Eikonal everywhere else. Obviously, the normalization factor can be adjusted should extreme variations exceeding these upper bounds be deemed interesting to study; however we have not found that to be necessary in connection with any of the studies in this paper. Note also that using the Eikonal for gluon splitting is likely to give a very large overestimate over most of phase space, as compared to the physical antenna functions (which only generate single logs, while the Eikonal generates double logs), thus leading to low

efficiency in the subsequent veto step. This may therefore be a technical point to improve on in future work, but for the time being we prefer the simplicity of having the same functional form to work with for all trials. Let us emphasize that the veto algorithm ensures that there is no trace of the overestimator present in the final results, either in tree-level expansions or in the Sudakov exponentials. The only sensitivity to the overestimator is in the *speed* of the calculation, which we have tested to be comparable to that of standalone PYTHIA 8.

Inserting the trial function  $a_{\text{trial-emit}}$  from eq. (32) and the Jacobian for the transformation from  $(s_{ij}, s_{jk})$  to arbitrary  $(Q_E^2, \zeta)$ , eq. (30) then becomes

$$\mathcal{A}_{\text{trial-emit}}(s, Q_{E1}^2, Q_{E2}^2) = \frac{C_A}{4\pi} \int_{Q_{E2}^2}^{Q_{E1}^2} dQ_E^2 d\zeta |J| \frac{2\hat{\alpha}_s}{s_{ij}s_{jk}}, \quad (35)$$

where we have kept  $\hat{\alpha}_s$  inside the integral since the renormalization scale may vary over phase space. The last remaining step before we can solve this equation is now to rewrite the term  $|J|/(s_{ij}s_{jk})$  in terms of  $Q_E$  and  $\zeta$  for a sufficiently general class of functional forms of  $Q_E$ .

We shall start by specifying  $\zeta$ . In principle, one could define a different  $\zeta$  for each possible choice of  $Q_E$ , but this would be cumbersome and would not lead to any significant gains. We have therefore settled on one particular form for  $\zeta$  to use for all evolution variables in this paper. There are two requirements for such a  $\zeta$  definition:

- It should be linearly independent of any  $Q_E$  that we would conceivably consider. I.e.,  $\zeta$  should not itself be a candidate for an evolution variable.
- Curves of constant  $\zeta$  should intersect curves of constant  $Q_E$  once and only once for all  $Q_E > 0$ , such that the Jacobian is well-defined.

A  $\zeta$  definition that fulfills these conditions for the entire class of  $Q_E$  variables we shall consider is the following simple ratio of invariants, illustrated in fig. 5:

$$\zeta = \frac{s_{ij}}{s_{ij} + s_{jk}} \quad \Rightarrow \quad 1 - \zeta = \frac{s_{jk}}{s_{ij} + s_{jk}}. \quad (36)$$

We emphasize again that all we have done so far is recast the Lorentz invariant phase space in terms of two new variables which are, themselves, arbitrary. There is no explicit dependence on the particular form of  $\zeta$ . (There is a dependence on  $Q_E$  of course, but only through the boundaries of the integral.)

To compute the Jacobian, we will need the derivatives,

$$\frac{\partial \zeta}{\partial s_{ij}} = \frac{s_{jk}}{(s_{ij} + s_{jk})^2} = \frac{\zeta(1 - \zeta)}{s_{ij}} \quad , \quad \frac{\partial \zeta}{\partial s_{jk}} = \frac{-s_{ij}}{(s_{ij} + s_{jk})^2} = \frac{-\zeta(1 - \zeta)}{s_{jk}}. \quad (37)$$

The Jacobian is,

$$\det \left( \frac{\partial \{s_{ij}, s_{jk}\}}{\partial \{Q_E^2, \zeta\}} \right) = \det^{-1} \left( \frac{\partial \{Q_E^2, \zeta\}}{\partial \{s_{ij}, s_{jk}\}} \right) = \frac{s_{ij}s_{jk}}{\zeta(1 - \zeta)} \left[ s_{ij} \frac{\partial Q_E^2}{\partial s_{ij}} + s_{jk} \frac{\partial Q_E^2}{\partial s_{jk}} \right]^{-1}. \quad (38)$$

Inserting this in eq. (35) we get a master equation for evolution in an arbitrary variable  $Q_E$  (for trials distributed according to the function  $\bar{a}_{\text{trial-emit}}$ ):

$$\mathcal{A}_{\text{trial-emit}}(s, Q_{E1}^2, Q_{E2}^2) = \frac{C_A}{4\pi} \int_{Q_{E1}^2}^{Q_{E2}^2} dQ_E^2 \int_{\zeta_{\min}(Q_E^2)}^{\zeta_{\max}(Q_E^2)} d\zeta \frac{2\hat{\alpha}_s}{\zeta(1 - \zeta)} \left[ s_{ij} \frac{\partial Q_E^2}{\partial s_{ij}} + s_{jk} \frac{\partial Q_E^2}{\partial s_{jk}} \right]^{-1}, \quad (39)$$

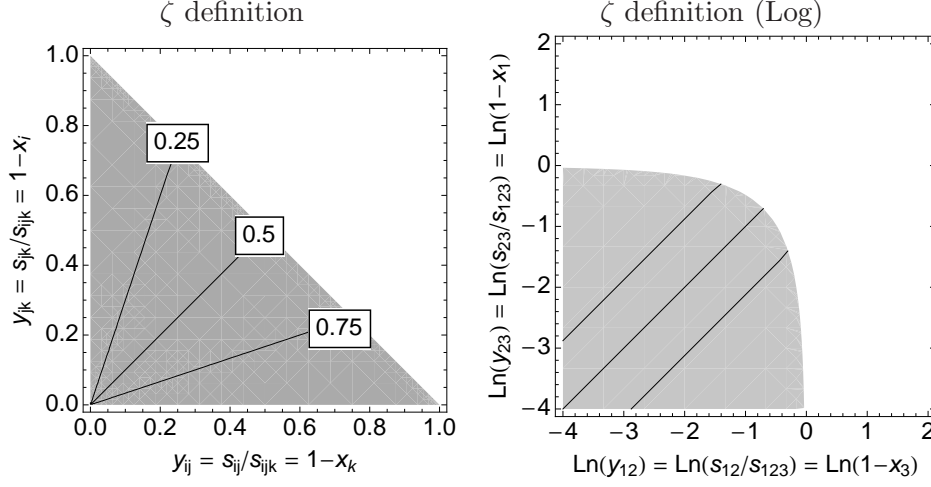


Figure 5: Illustration of the  $\zeta$  definition, eq. (36). The physical phase space, shown in grey, is the same on both panes, and the  $\zeta$  definition is also the same, but on the left the phase space is shown on a linear scale in the branching invariants and on the right on a logarithmic one.

where the function in square brackets represents the leftovers from the Jacobian, and the functions  $\zeta_{\min}(Q_E^2)$  and  $\zeta_{\max}(Q_E^2)$  re-express the phase-space triangle in terms of  $Q_E$  and  $\zeta$ . Given any specific form of  $Q_E$  these three functions can be derived, and hence a particular evolution equation obtained.

### 3.3 Evolution Variables

Given the structure of eq. (39), one sees that the evolution integral will become particularly simple for any evolution variable which satisfies the following simple differential equation,

$$Q_E^2(s, s_{ij}, s_{jk}) = \kappa_E \left( s_{ij} \frac{\partial Q_E^2}{\partial s_{ij}} + s_{jk} \frac{\partial Q_E^2}{\partial s_{jk}} \right). \quad (40)$$

Rather than base our formalism on one particular choice of evolution variable, as is usually done, we shall therefore instead derive our formalism so that it applies to *any* evolution variable which satisfies eq. (40). Making only this requirement, the evolution integral simplifies to

$$\mathcal{A}_{\text{trial-emit}}(s, Q_{E1}^2, Q_{E2}^2) = \kappa_E \frac{C_A}{4\pi} \int_{Q_{E2}^2}^{Q_{E1}^2} \frac{dQ_E^2}{Q_E^2} \int_{\zeta_{\min}(Q_E^2)}^{\zeta_{\max}(Q_E^2)} d\zeta \frac{2\hat{\alpha}_s}{\zeta(1-\zeta)}, \quad (41)$$

which may be solved once and for all, independently of the choice of  $Q_E$ . (The explicit dependence on the form of  $Q_E$  will reemerge, as it should, when translating from a generated set of  $(Q_E, \zeta)$  back to the branching invariants,  $(s_{ij}, s_{jk})$ , but this is a separate step, to be treated below.) As explained later, we will take  $\hat{\alpha}_s$  to depend solely on  $Q_E^2$ , and to be independent of  $\zeta$ .

Though any symmetric power series in the branching invariants is a solution to eq. (40), for the purpose of this paper we shall impose two additional “reasonable” boundary conditions. Firstly, that an infinitely soft branching should always be classified as “unresolved” for any finite value of the evolution variable, i.e., the evolution variable must go to zero when both

invariants vanish,  $Q_E(0,0) = 0$ . We note that this apparently mild restriction will nonetheless prevent us from considering a specific class of variables, which in fact include angular ordering, since in an angular-ordered cascade, a large-angle emission may be resolved, even when soft. We shall also require that the evolution variable be symmetric in the two invariants,  $Q_E(y_{ij}, y_{jk}) = Q_E(y_{jk}, y_{ij})$ .

We can put the differential equation (40) in dimensionless form by dividing by  $s$ ,

$$Y_E(y_{ij}, y_{jk}) = \kappa_E \left( \frac{\partial Y_E}{\partial \ln y_{ij}} + \frac{\partial Y_E}{\partial \ln y_{jk}} \right), \quad (42)$$

where  $Y_E = Q_E^2/s$ ,  $y_{ij} = s_{ij}/s$ , and  $y_{jk} = s_{jk}/s$ .

If we define

$$L_+ = (\ln y_1 + \ln y_2)/2, \quad L_- = (\ln y_1 - \ln y_2)/2, \quad (43)$$

then eq. (42) takes the form,

$$Y_E(L_+, L_-) = \kappa_E \frac{\partial Y_E}{\partial L_+}, \quad (44)$$

which has the general solution,

$$\begin{aligned} Y_E(s_{ij}, s_{jk}) &= \hat{f}_0(L_-) \exp(L_+/\kappa_E) + c_0 \\ &= f_0(s_{ij}/s_{jk}) (s_{ij}s_{jk}/s^2)^{1/(2\kappa_E)} + c_0. \end{aligned} \quad (45)$$

where  $f_0$  is a dimensionless function satisfying  $f_0(x) = f_0(1/x)$  and the requirement that  $Y_E(0,0) = 0$ , and  $c_0$  is a constant (which we uniformly set to zero).

For illustrative purposes, it will be convenient to introduce additional parameters — a main shape parameter,  $a$ , and two auxiliary parameters  $b$  and  $p$  — and take

$$f_0(x) = \left( \left[ \left( \sqrt{x} + \sqrt{\frac{1}{x}} \right)^2 \right]^a - b \left[ \left( \sqrt{x} - \sqrt{\frac{1}{x}} \right)^2 \right]^a \right)^p. \quad (46)$$

This yields a continuously deformable class of evolution variables that fulfill eq. (40) subject to our two additional conditions; the corresponding expression for the evolution variable is,

$$Q_E^2(s, s_{ij}, s_{jk}) = s \left( \left[ \left( \frac{s_{ij} + s_{jk}}{s} \right)^2 \right]^a - b \left[ \left( \frac{s_{ij} - s_{jk}}{s} \right)^2 \right]^a \right)^p, \quad (47)$$

subject to the constraints,

$$a > 0, \quad b \leq 1, \quad p > 0, \quad 2ap = \frac{1}{\kappa_E}. \quad (48)$$

The overall normalization is fixed so that the maximum of the evolution variable is the invariant mass of the dipole:  $a$  sets the relative soft/collinear resolution power (to be explained further below);  $b \neq 1$  allows for variables which do not go to zero on the axes (i.e., for which purely collinear branchings may appear resolved, as is the case, e.g., for energy ordering), and thus requires an additional infrared regulator independent of the evolution variable; and  $p$  allows modifying the overall speed of the evolution over phase space.

The effect of varying  $a$  is illustrated in fig. 6, with  $b = 1$ . We increase  $a$  from left to right in the figure. Small values, toward the left, yield evolution variables that are “better” at resolving

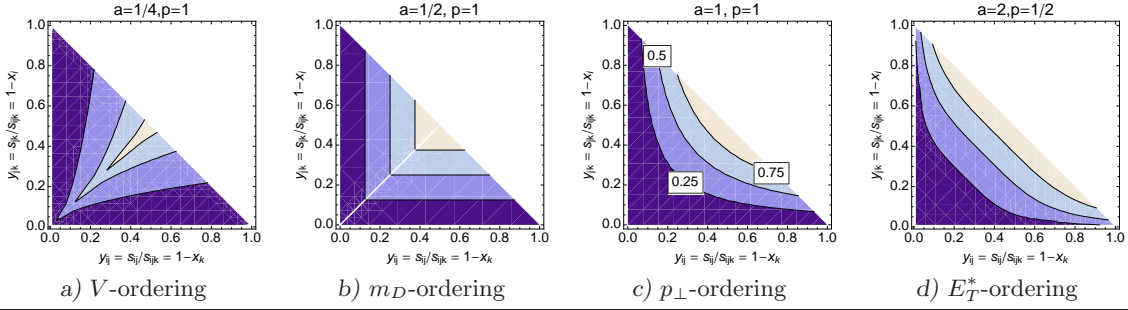


Figure 6: Illustration of the  $a$  parameter in eq. (47). Note that the second plot from the left corresponds to choosing the daughter antenna mass as the evolution variable, and the third pane corresponds to the ARIADNE definition of  $p_\perp$ . Contour labels indicate values of  $y_E = Q_E^2/s$ .

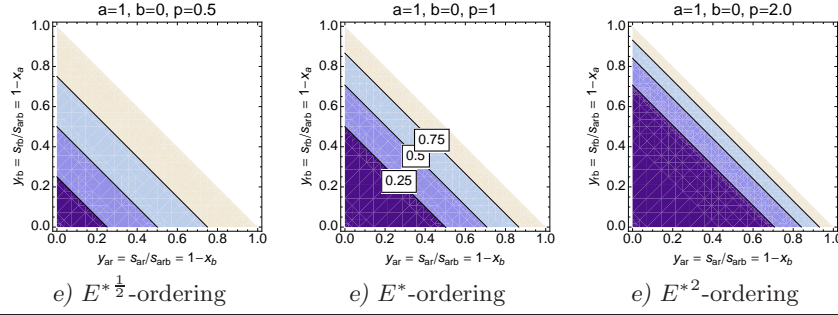


Figure 7: Illustration of the  $b$  and  $p$  parameters in eq. (47). Note that all of these variables are proportional to the energy of the emitted gluon (in the CM of the dipole-antenna) to some power. Contours indicate values of  $y_E = Q_E^2/s$ .

phase-space points towards the origin (corresponding to soft branchings) whereas large values of  $a$  yield variables that are “better” at resolving points near the axes (corresponding to purely collinear ones). A shower based on the evolution variable to the far left in the figure would generate soft branchings earlier in the shower than collinear ones, while a complementary ordering would result in a shower based on the variable illustrated on the far right. We stress that the leading limiting behavior in the soft and collinear regions are in all cases the same, but these differences will lead to *subleading* differences between the showers. The size of these differences may be estimated by varying the evolution variable used to generate the showers.

An illustration of the  $b$  parameter is obtained by comparing the plots in fig. 6 to those in fig. 7, where the former all have  $b = 1$  and the latter all  $b = 0$ . As mentioned above, choosing  $b \neq 1$  gives evolution variables that do not go to zero on the axes. Accordingly, the contours on the plots in fig. 7 intersect the axes, while the ones in fig. 6 do not. The corresponding showers would generally have greater sensitivity to the infrared region and thus to hadronization effects. These variables correspond to those that are used in some analytic resummation calculations [50]. Finally, going from left to right in fig. 7, we see that small

Name	$a$	$b$	$p$	Resulting form for $Q_E^2$	$\zeta_{\min}(Q_E^2)$	$\zeta_{\max}(Q_E^2)$
1 $p_{\perp}$ -ordering	1	1	1	$\frac{4s_{ij}s_{jk}}{s} = 4p_{\perp}^2 \text{Ariadne}$	$\frac{1 \mp \sqrt{1 - Q_E^2/s}}{2}$	
2 $m_D$ -ordering	$\frac{1}{2}$	1	1	$2\min(s_{ij}, s_{jk}) = 2m_D^2$	$\frac{Q_E^2}{2s}$	$1 - \frac{Q_E^2}{2s}$
3 $E^*$ -ordering	1	0	1	$\frac{(s_{ij}+s_{jk})^2}{s} = 4E_j^{*2}$	0	1
4 $V$ -ordering	$\frac{1}{4}$	1	1	$\sqrt{s(s_{ij}+s_{jk})} - \sqrt{s s_{ij}-s_{jk} }$	$\frac{1 \mp (1 - Q_E^2/s)^2}{2}$	
5 $E_{Tn}^*$ -ordering ( $n \geq 1$ )	$2n$	1	$\frac{1}{2n}$	$n = 1 : \frac{\sqrt{8s_{ij}s_{jk}(s_{ij}^2+s_{jk}^2)}}{s}$	$\frac{1 \mp (1 - (Q_E^2/s)^{2n})^{\frac{1}{4n}}}{2}$	

Table 1: Examples of evolution variables in the form of eq. (47) and corresponding to the illustrations in figs. 6 and 7. The nominal  $\zeta$  boundaries for  $E^*$  ordering would lead to infinities, so for practical applications the bounds implied by the hadronization cutoff should be used instead.

values of the speed parameter,  $p$ , correspond to a faster progress of the evolution variable over phase space, whereas large  $p$  values give the opposite. This speed has no effect on the generation of the first branching, but it does affect the value of the restart scale for subsequent branchings, which we will return to below.

Some specific examples of evolution variables of this form that could be useful for Monte Carlo purposes are given in table 1, where we also give the corresponding  $\zeta$  limit functions and show how the generic functional form, eq. (47), simplifies considerably in several cases. For instance, setting  $a = 1$ ,  $b = 1$ ,  $p = 1$  gives the  $p_{\perp}$ -ordering variable used both in ARIADNE as well as in more recent work [32, 33]. Contours of constant value of this variable are shown on the third pane of fig. 6. Contours illustrating the other variables in tab. 1 can also be found in figs. 6 and 7. ( $E_{Tn}^*$ -ordering is shown for  $n = 1$  only, for which case we leave out the explicit subscript  $n$ .) Note that the name  $E_{Tn}^*$  does not imply that this variable represents a physical transverse energy, but rather that it represents an interpolation between  $p_{\perp}$  and  $E^*$ , with lower values of the  $n$  parameter making it closer to  $p_{\perp}$  and higher values making it closer to  $E^*$ . The  $V$  variable is named simply for the shape it has over phase space, like a  $V$  pointing towards the soft region, cf. the leftmost pane in fig. 6.

For completeness, a few important examples of evolution variables that are *not* covered using our formalism are the traditional  $1 \rightarrow 2$  parton-shower ones in PYTHIA and HERWIG, illustrated in fig. 8. For the forms of the HERWIG and PYTHIA evolution variables, translated to our phase-space notation, we used the following (for evolution with parton  $I$  as the emitter):

$$\begin{aligned}
\text{PYTHIA} & : \quad m_{I^*}^2 = s_{ij} \\
\text{virtuality-} & \\
\text{ordering} & \\
\text{PYTHIA} & : \quad 4p_{\perp \text{evol}, I}^2 = 4 \frac{s_{ij}(s - s_{jk})(s_{ij} + s_{jk})}{(s + s_{ij})^2} \\
p_{\perp \text{evol}}\text{-ordering} & \\
\text{HERWIG++} & : \quad q_{\theta, I}^2 = 4s \left( \frac{ss_{ij}}{(s - s_{jk})(s_{ij} + s_{jk})} \right)^2 = 4s \left( \frac{1 - x_k}{x_i x_j} \right)^2, \\
\text{angular-ordering} &
\end{aligned} \tag{49}$$

where we used  $x_i = (1 - s_{jk}/s)$  in the last expression. For the PYTHIA  $p_{\perp \text{evol}}$  variable,  $j$  is

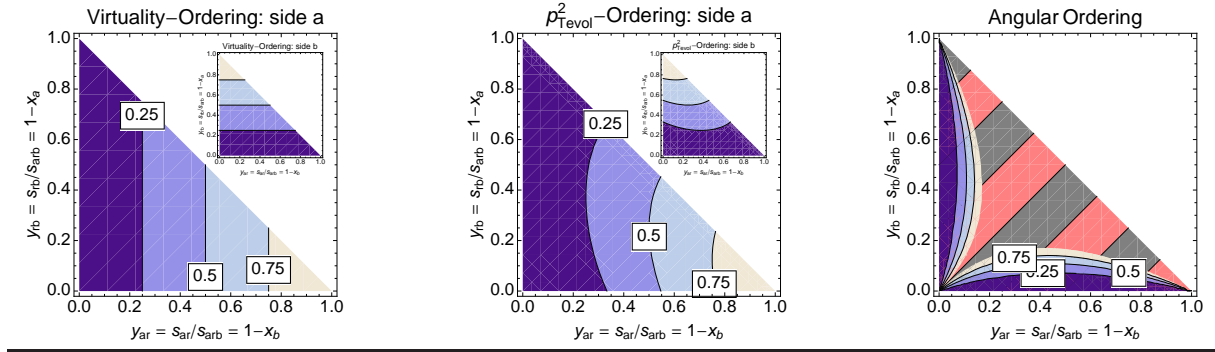


Figure 8: In an old-fashioned parton shower or partioned-dipole shower, the process  $\hat{a}\hat{b} \rightarrow arb$  is divided onto two terms, one representing emission off parton  $\hat{a}$  and the other emission off parton  $\hat{b}$ . *Left Pane*: contours of constant  $s_{ar}$ , i.e., the virtuality that corresponds to  $a^* \rightarrow ar$  in a virtuality-ordered parton shower. The inset shows the equivalent contours for emission off side  $b$ . *Middle Pane*: contours of constant  $p_{Tevol}^2$ , the variable used in the  $p_\perp$ -ordered PYTHIA shower. Note that for the virtuality-ordered shower, additional vetos on the emission angle, not shown here, must be imposed to enforce coherence, while in the  $p_\perp$ -ordered case, this is less crucial due to the use of dipole kinematics. In an *angular*-ordered parton shower (right pane), each parton is still evolved separately, but the potential for double counting has been removed by effectively restricting the emission from each parton to non-overlapping regions, here angular-ordered cones, and hence we can represent the two terms on one and the same plot. (Note: while the original HERWIG implementation of angular ordering did imply some overlap in the soft region, this has been removed in HERWIG++.) The price to pay is that this introduces an artificially unpopulated dead zone in the phase space, illustrated by the striped area. The contour labels denote values of  $y_E = Q_E^2/s$ .

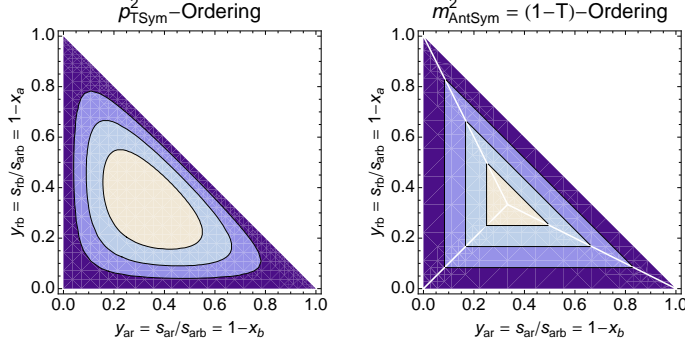


Figure 9: Examples of evolution variables for which our  $\zeta$  definition would be multi-valued for each value of  $Q_E$ . These particular ones were obtained by merely symmetrizing  $p_{\perp}$  (left) and  $m_D$  (right) in all three branching invariants.

the emitted parton, and  $k$  is the recoiling one. Analogous expressions hold when parton  $K$  is the emitter, with the substitutions  $s_{ij} \leftrightarrow s_{jk}$ .

Likewise, variables that do not have well-defined Jacobians with our  $\zeta$  definition, such as those in fig. 9, cannot be used without additional work. Examples include,

$$p_{\perp \text{Sym}}^2 = 27 \frac{s_{ij}s_{jk}s_{ik}}{s^2} \quad (50)$$

$$m_{D \text{Sym}}^2 = 3 \min(s_{ij}, s_{jk}, s_{ik}) = 3s(1 - T_3) , \quad (51)$$

where  $T_3$  is the Thrust event shape variable for a three-parton configuration. The  $p_{\perp \text{Sym}}$  variable is similar to the  $C$ -parameter for a 3-parton configuration,

$$C_3 = 6 \frac{s_{ij}s_{jk}s_{ki}}{(s - s_{ij})(s - s_{jk})(s - s_{ki})} \leq \frac{3}{4}, \quad (52)$$

which one could therefore also imagine using as the basis for an evolution variable, with  $Q_E^2 = \frac{4}{3}sC_3$ .

### 3.4 The $\zeta$ integral

In general, one might expect the running coupling  $\alpha_s$  to depend on  $\zeta$  as well as  $Q_E$  and  $s$ . If we simplify the dependence by taking it to depend only on  $Q_E$  and/or  $s$ , then the integral over  $\zeta$  is straightforward:

$$I_{\zeta}(\zeta_{\min}(Q_E^2), \zeta_{\max}(Q_E^2)) = \int_{\zeta_{\min}(Q_E^2)}^{\zeta_{\max}(Q_E^2)} d\zeta \frac{1}{\zeta(1 - \zeta)} = \ln \left[ \frac{\zeta_{\max}(Q_E^2)(1 - \zeta_{\min}(Q_E^2))}{\zeta_{\min}(Q_E^2)(1 - \zeta_{\max}(Q_E^2))} \right]. \quad (53)$$

One would expect any  $\zeta$  dependence in  $\alpha_s$  to be reduced by computing to higher orders in perturbation theory. At a fixed order, a  $\zeta$ -dependent  $\alpha_s$  could still be accommodated, for example, by choosing a  $\zeta$ -independent (large)  $\hat{\alpha}_s$  for trials and then applying the veto algorithm. The case of a  $Q_E$ -dependent  $\alpha_s$  will be treated explicitly below.



VINCIA EVOLUTION WINDOWS			
$i$	$[Q_{E\min}$	, $Q_{E\max}]$	$n_f$
0	[0	, $m_c]$	3
1	$[m_c$	, $m_b]$	4
2	$[m_b$	, $\sqrt{m_b m_t}]$	5
3	$[\sqrt{m_b m_t}$	, $m_t]$	5
4	$[m_t$	, $\infty]$	6

Table 2: The evolution windows used in VINCIA, with the  $Q_E$  boundaries and active number of flavors corresponding to each. The number of active flavors is the same for windows 2 and 3, but the  $\zeta$  boundaries for trials are different, due to the different  $Q_{E\min}$  values. This improves the efficiency of the generator. The first window will not actually extend down to zero in practice, but will instead be cut off by the hadronization scale.

### 3.5 Evolution Windows

To simplify the trial generation further we shall generate trial branchings in a larger phase-space region than the physically allowed one, again using the veto algorithm to avoid generating any actual branchings in the unphysical region. Specifically, we divide the generation of trial branchings into discrete windows in  $Q_E$  — given in table 2 — and, in each such window, replace the  $\zeta$  limits in the previous equation by constant ones,

$$\zeta_{\min}(Q_E^2) = \zeta_{\min}(Q_{E\min}^2) \quad , \quad \zeta_{\max}(Q_E^2) = \zeta_{\max}(Q_{E\min}^2) \quad (54)$$

where  $Q_{E\min}$  is the value of  $Q_E$  at the end of the current window (e.g., the next flavor threshold or, ultimately, the hadronization scale). If none of the generated trials fall within the current evolution window, the evolution should be restarted at  $Q_E = Q_{E\min}$ , upon which the  $Q_{E\min}$  and  $\zeta$  boundaries should be updated to correspond to those of the next evolution window. If the crossing corresponds to a flavor threshold, the normalization of the trial function for gluon splitting should be updated with the new number of active flavors, and if  $\alpha_s$  depends explicitly on  $Q_E$ , then  $\Lambda_{\text{QCD}}$  should, likewise, be updated.

### 3.6 $Q_E$ integral for $Q_E$ -independent $\alpha_s$

With the  $\zeta$  integral for trial branchings having now effectively become a constant depending only on the current “evolution window” (i.e., the current  $Q_{\min}$ ), we may perform the  $Q_E$  integration independently of the  $\zeta$  one. We do this first for the case where the renormalization scale in  $\alpha_s$  is constant over the branching phase space.

In this case, the evolution integral, eq. (41), becomes

$$\mathcal{A}_{\text{trial-emit}}(Q_{E1}^2, Q_{E2}^2) = 2\hat{\alpha}_s \kappa_E \frac{C_A}{4\pi} I_\zeta(\zeta_{\min}, \zeta_{\max}) \ln \left( \frac{Q_{E1}^2}{Q_{E2}^2} \right) \quad , \quad (55)$$

where  $\zeta_{\min, \max}$  are the ones appropriate to the current evolution window, as given in tabs. 1 & 2.

The equivalent expression for the trial function for gluon splitting,  $\mathcal{A}_{\text{trial-split}}$ , only differs by an overall normalization factor, cf. eqs. (32) & (33), and hence we do not reproduce it explicitly here.

In addition to a zeroth order (fixed)  $\alpha_s$  or a running  $\alpha_s$  that depends only on the parent dipole-antenna mass,  $\alpha_s(s)$ , these expression will be needed, for instance, to use  $\alpha_s(p_\perp)$  together with any non- $p_\perp$  evolution variable. Technically, we accomplish this by setting the trial  $\hat{\alpha}_s$  equal to unity (or some other relatively large number) in the above equation and then accepting the generated  $(Q_E, \zeta)$  pair with the probability  $\alpha_s(p_\perp)/\hat{\alpha}_s$ .

### 3.7 $Q_E$ integral for first-order $Q_E$ -dependent $\alpha_s$

We shall also allow for the possibility to use a first-order running  $\alpha_s$ , with a renormalization scale that depends explicitly on  $Q_E$ ,

$$\alpha_s(k_\mu^2 Q_E^2) = \frac{1}{b_0 \ln(k_\mu^2 Q_E^2 / \Lambda^2)} , \quad (56)$$

where

$$b_0 = \frac{11C_A - 2n_f \hat{T}_R}{12\pi} , \quad (57)$$

and where  $k_\mu$  is an overall scaling factor,  $n_f$  is the active number of flavors, and  $\Lambda$  is the appropriate ( $n_f$ -dependent) value of  $\Lambda_{\text{QCD}}$ .

The evolution integral then becomes

$$\begin{aligned} \mathcal{A}_{\text{trial-emit}}(s, Q_{E1}^2, Q_{E2}^2) &= 2\kappa_E \frac{C_A}{4\pi} I_\zeta(\zeta_{\min}, \zeta_{\max}) \frac{1}{b_0} \int_{Q_{E2}^2}^{Q_{E1}^2} \frac{dQ_E^2}{Q_E^2} \frac{1}{\ln(k_\mu^2 Q_E^2 / \Lambda^2)} \\ &= 2\kappa_E \frac{C_A}{4\pi} I_\zeta(\zeta_{\min}, \zeta_{\max}) \frac{1}{b_0} \int_{x_{E2}^2}^{x_{E1}^2} \frac{dx_E^2}{x_E^2} \frac{1}{\ln(x_E^2)} \\ &= 2\kappa_E \frac{C_A}{4\pi} I_\zeta(\zeta_{\min}, \zeta_{\max}) \frac{1}{b_0} \ln \left( \frac{\ln(x_{E1}^2)}{\ln(x_{E2}^2)} \right) , \end{aligned} \quad (58)$$

where

$$x_E^2 = \frac{k_\mu^2 Q_E^2}{\Lambda^2} . \quad (59)$$

### 3.8 $Q_E$ integral for $Q_E$ -dependent $\alpha_s$

More generally, we can incorporate a  $Q_E$ -dependent  $\alpha_s$  by changing variables using the  $\beta$  function,

$$\frac{d\alpha_s(Q_E^2)}{d \ln Q_E^2} = \beta(\alpha_s) . \quad (60)$$

This allows us to rewrite eq. (41) as follows,

$$\mathcal{A}_{\text{trial-emit}}(s, Q_{E1}^2, Q_{E2}^2) = \kappa_E \frac{C_A}{4\pi} \int_{\alpha_s(Q_{E1}^2)}^{\alpha_s(Q_{E2}^2)} \frac{d\alpha_s}{\beta(\alpha_s)} \int_{\zeta_{\min}(Q_E^2(\alpha_s))}^{\zeta_{\max}(Q_E^2(\alpha_s))} d\zeta \frac{2\alpha_s}{\zeta(1-\zeta)} \quad (61)$$

When we make the substitutions of eq. (54) here, the inner integral will be independent of  $\alpha_s$ . With the two-loop beta function,

$$\beta(\alpha_s) = -b_0 \alpha_s^2 - b_1 \alpha_s^3 , \quad (62)$$

where  $b_0$  is given by eq. (57) and

$$b_1 = \frac{17C_A^2 - n_f \hat{T}_R(5C_A + \frac{3}{2}\hat{C}_F)}{24\pi^2}, \quad (63)$$

the  $\alpha_s$  integral is simple,

$$\int_{\alpha_s(Q_{E1}^2)}^{\alpha_s(Q_{E2}^2)} \frac{d\alpha_s}{\beta(\alpha_s)} = \frac{1}{b_0} \ln\left(\frac{\alpha_s(Q_{E1}^2)}{\alpha_s(Q_{E2}^2)}\right) + \frac{1}{b_0} \ln\left(\frac{1 + b_1/b_0 \alpha_s(Q_{E2}^2)}{1 + b_1/b_0 \alpha_s(Q_{E1}^2)}\right). \quad (64)$$

This function can be inverted readily using a Newton-Raphson solver, which can likewise be used to obtain  $Q_E^2(\alpha_s)$ . It can be extended readily to higher loops because additional orders only introduce new denominator factors of the form  $(1 + c\alpha_s)$ .

### 3.9 The Evolution Equation

We now have all the pieces in hand to construct the evolution equation for a generic shower subject only to the conditions outlined in the preceding paragraphs; that the individual trial branchings be  $2 \rightarrow 3$  mappings from on-shell momenta to on-shell momenta, respecting the Lorentz-invariant phase-space decomposition, eq. (12), for any evolution variable that satisfies the differential equation, eq. (40).

The generating function for such a shower is the Sudakov form factor,

$$\Delta(Q_{E1}^2, Q_{E2}^2) = \exp\left(-\mathcal{A}(Q_{E1}^2, Q_{E2}^2)\right), \quad (65)$$

where we may substitute for  $\mathcal{A}$  either of the expressions eqs. (55) or (58).

In order to generate trial branchings according to this Sudakov, we must solve the equation

$$R = \Delta(Q_{E1}^2, Q_{E2}^2) \quad (66)$$

for  $Q_{E2}$ , where  $R$  is a random number distributed uniformly between zero and one and  $Q_{E1}$  is the “(re)starting scale”. The latter represents the scale the shower is being restarted at prior to the generation of the next trial branching. To give an idea, this can either be the full dipole center-of-mass energy,  $\sqrt{s}$ , which will usually be the case for the very first branching following a resonance decay, or, later on in the shower evolution, the scale of the preceding trial branching.

The solution of this equation is the paramount reason we chose to use a simplified antenna function for trial generations. It would have been possible to solve the evolution integral itself for more complicated trial functions, but the inversion of eq. (66) to solve for  $Q_{E2}$  as a function of  $R$  and  $Q_{E1}$  would then have been much more cumbersome.

Solving the evolution equation for a  $Q_E$ -independent  $\hat{\alpha}_s$ , using eq. (55), yields

$$Q_{E2}^2 = Q_{E1}^2 R^b, \quad (67)$$

with

$$b = \frac{4\pi}{2\hat{\alpha}_s \kappa_E C_A I_\zeta(\zeta_{\min}(Q_{E\min}^2), \zeta_{\max}(Q_{E\min}^2))}. \quad (68)$$

Solving the evolution for a first-order running  $Q_E$ -dependent  $\hat{\alpha}_s$ , using eq. (58), yields

$$Q_{E2}^2 = \frac{\Lambda^2}{k_\mu^2} \left( \frac{k_\mu^2 Q_{E1}^2}{\Lambda^2} \right)^{R^{b'}} , \quad (69)$$

with

$$b' = \frac{4\pi}{2\kappa_E C_A I_\zeta(\zeta_{\min}(Q_{E\min}^2), \zeta_{\max}(Q_{E\min}^2))} \frac{11C_A - 2n_f \hat{T}_R}{12\pi} . \quad (70)$$

As mentioned earlier, given any set of branching variables  $(Q_E^2, \zeta)$  we may obtain the invariants  $(s_{ij}, s_{jk})$  without ambiguity. Thus, the next step is to generate a  $\zeta$  value, given  $Q_{E2}$ . Since we defined  $\zeta$  independently of  $Q_E$ , we may do this once and for all, with the solution applicable to all evolution variables. To generate a random  $\zeta$  value distributed according to the integrand of the  $I_\zeta$  integral, eq. (53), we must solve the equation

$$R_\zeta = \frac{I_\zeta(\zeta_{\min}, \zeta)}{I_\zeta(\zeta_{\min}, \zeta_{\max})} \quad (71)$$

for  $\zeta$ , where  $R_\zeta$  is another random number uniformly distributed between zero and one, the  $I_\zeta$  integral given by eq. (53), and  $\zeta_{\min}(Q_{E\min})$  is given by the evolution windows (Table 2) and by the evolution-variable-dependent  $\zeta$  limits (Table 1).

We solve eq. (71) by first translating to the variable  $r$ ,

$$r_{\max} = \frac{\zeta_{\max}}{1 - \zeta_{\max}} \quad , \quad r_{\min} = \frac{\zeta_{\min}}{1 - \zeta_{\min}} \quad , \quad (72)$$

generating a random value for  $r$

$$r = r_{\min} \left( \frac{r_{\max}}{r_{\min}} \right)^{R_\zeta} , \quad (73)$$

and finally solving for  $\zeta$ ,

$$\zeta = \frac{r}{1 + r} . \quad (74)$$

If the  $\zeta$  generated in this way falls outside the physical phase space,

$$\zeta < \zeta_{\min}(Q_E^2) \quad \vee \quad \zeta > \zeta_{\max}(Q_E^2) \quad (75)$$

the branching is vetoed. This occurs some fraction of the time for the simple reason that we generated the trial branchings in a hull encompassing the physical phase space. That is, the trials are generated on a phase-space region bounded by  $\zeta_{\min, \max}(Q_{E\min}^2)$ , whereas the physical phase space at  $Q_E$  is bounded by  $\zeta_{\min, \max}(Q_E^2)$ . Since the physical branching probability outside the physical phase space is obviously zero, the probability to accept unphysical trial branchings should be zero as well. This is accomplished by the veto. After a failed trial branching, the evolution is restarted at the scale of the failed trial, as required by the veto algorithm.

The last step is to obtain values for the pair of phase-space invariants  $(s_{ij}, s_{jk})$  in terms of which we cast the original evolution equation, eq. (30). Since different forms of  $Q_E$  depend

in a different way on these invariants, this step is obviously  $Q_E$ -dependent. Here, we give the inversions relevant to the four evolution variables so far implemented in VINCIA.

$$s_{ij} = \zeta g_{\text{evolution}}(s, Q_E^2, \zeta) \quad ; \quad s_{jk} = (1 - \zeta) g_{\text{evolution}}(s, Q_E^2, \zeta) \quad (76)$$

with

$$\textbf{Type 1:} \quad g_{p_\perp} = \frac{Q_E \sqrt{s}}{2\sqrt{\zeta(1-\zeta)}} \quad , \quad (77)$$

$$\textbf{Type 2:} \quad g_{m_D} = \frac{Q_E^2}{\min(\zeta, 1-\zeta)} \quad , \quad (78)$$

$$\textbf{Type 3:} \quad g_{E^*} = Q_E \sqrt{s} \quad , \quad (79)$$

$$\textbf{Type 4:} \quad g_V = \frac{Q_E^4}{2s(\min(\zeta, 1-\zeta) + \sqrt{|1-2\zeta|})} \quad . \quad (80)$$

More generally, in terms of the function  $f_0$  that parametrizes the general solution (45), the inversion takes the following form,

$$g_{f_0} = \frac{s}{\sqrt{\zeta(1-\zeta)}} \left( \frac{Q_E^2}{s f_0} \right)^{\kappa_E} \quad . \quad (81)$$

### 3.10 The LL Shower

In the previous subsections, the ingredients for generating a single trial branching with a trial branching function  $a_{\text{trial}}$  were described. To obtain an LL shower, it suffices to accept each trial branching with a probability

$$P^{\text{LL}} = \frac{\alpha_s \mathcal{C}_{ijk}}{\hat{\alpha}_s \hat{\mathcal{C}}_{ijk}} \frac{\bar{a}_{\text{LL}}(s, s_{ij}, s_{jk})}{\bar{a}_{\text{trial}}(s, s_{ij}, s_{jk})} \quad , \quad (82)$$

where the  $\alpha_s/\hat{\alpha}_s$  ratio takes into account the possibility that the trial generator could be using a nominally larger  $\alpha_s$  than the physically desired one, the  $\mathcal{C}/\hat{\mathcal{C}}$  factor represents the same for color factors, and the antenna function ratio matches the trial function onto the desired physical splitting antenna for the relevant  $2 \rightarrow 3$  branching. Because we chose  $\bar{a}_{\text{trial}}$  to be larger than (or equal to) the true antenna function  $\bar{a}_{\text{LL}}$  everywhere in the dipole-antenna phase space, this probability is always less than (or equal to) 1. We must also require  $\bar{a}_{\text{LL}}$  to be non-negative in order that the ratio here be interpretable as probability.

We initiate the shower in electron-positron collisions with quark-pair creation from the intermediate vector boson. At each stage in the shower, a gluon will be emitted, or a gluon will split into a quark-antiquark pair. The shower itself evolves in the leading-color approximation, so after each emission, the number of different antennae grows by one, whereas each splitting leaves the number of antennae unchanged. We must allow all the different antennae to branch, of course; we do this by computing trial branchings for all of them, and picking the antenna with the highest trial branching scale. For that antenna, we then apply a veto with the probability given in eq. (82).

When a branching is accepted, the physical replacement of partons  $I$  and  $K$  by  $i$ ,  $j$ , and  $k$  in the event record next has to be performed. It is here that the dependence on the *kinematics map* enters. Our treatment of this point is identical to that described in detail in ref. [33], and the implementation in VINCIA retains the possibility to choose between the three different maps defined there. These maps all have identical limits in the LL singular regions, but differ from each other elsewhere.

For a pure strongly-ordered LL shower (i.e., a level of approximation comparable to all other currently existing shower Monte Carlo implementations), the evolution should then be restarted from the scale of the current trial (regardless of whether that trial was accepted or not, as per the veto algorithm; the phase space above that scale has already been probed, and hence — according to the strong-ordering condition — should not be probed again.)

To examine the quality of this type of approximation independently of the shower generator, we use RAMBO [51] (an implementation of which has been included in VINCIA) to generate a large number of evenly distributed 4-, 5-, and 6-parton phase-space points. For each phase-space point, we evaluate the  $Z \rightarrow n$  matrix element using MADGRAPH (suitably modified to be able to switch subleading color terms on and off). We then compute the tree-level LL antenna-shower approximation corresponding to the same phase-space point, based on nested products of  $2 \rightarrow 3$  branchings subjected to the condition of ordering in the chosen evolution variable. Finally, we form the ratio between this approximation and the full matrix element. This is similar to what was done in ref. [34]; where that study was limited to the emission of two partons, the addition of a new automated interface to MADGRAPH allows us here to extend the corresponding comparisons through four emissions, thus making it possible to illustrate in detail how the agreement or disagreement changes with increasing number of emissions.

Using a clustering algorithm that contains the exact inverses of the VINCIA  $2 \rightarrow 3$  kinematics maps [34], we may perform  $m$  clusterings of the type  $(i, j, k) \rightarrow (I, K)$  in a way that exactly reconstructs the intermediate  $(n - m)$ -parton configurations that would have been part of the shower history for each  $n$ -parton test configuration, for any of the three kinematics maps so far implemented in VINCIA. This gives us an exact reconstruction of how the antenna shower would have populated each path. The strong ordering condition corresponds to step functions in the shower approximation. E.g., for  $Z \rightarrow q_1 g_2 g_3 \bar{q}_4$ , we have [34],

$$R_4 = \frac{\left( \Theta(Q_{3A} - Q_{4A}) a_{q\bar{q}}(1, 2, 3) a_{q\bar{q}}(\widehat{12}, \widehat{23}, 4) + \Theta(Q_{3B} - Q_{4B}) a_{q\bar{q}}(2, 3, 4) a_{q\bar{q}}(1, \widehat{23}, \widehat{34}) \right) |M_2(s)|^2}{|M_4(1, 2, 3, 4)|^2}, \quad (83)$$

where hatted variables  $\widehat{ij}$  denote clustered momenta,  $a$  denote  $2 \rightarrow 3$  antenna functions,  $|M_n|^2$  denote the color-ordered  $n$ -parton matrix elements,  $s$  is the total invariant mass squared of the  $n$ -parton system, and the ordering conditions depend on

$$\begin{aligned} Q_{4A} &= Q_E(1, 2, 3) & ; & & Q_{3A} &= Q_E(\widehat{12}, \widehat{23}, 4) \\ Q_{4B} &= Q_E(2, 3, 4) & ; & & Q_{3B} &= Q_E(1, \widehat{23}, \widehat{34}) \end{aligned} \quad (84)$$

The numerator of eq. (83) thus reproduces the shower approximation expanded to tree level, phase-space point by phase-space point, for an arbitrary choice of kinematics map,  $(i, j, k) \rightarrow (\widehat{ij}, \widehat{jk})$ , and evolution variable,  $Q_E$ .  $R$  thus gives a direct tree-level measure of the amount of over- or under-counting by the shower approximation, with values greater than unity corresponding to over-counting and vice versa.

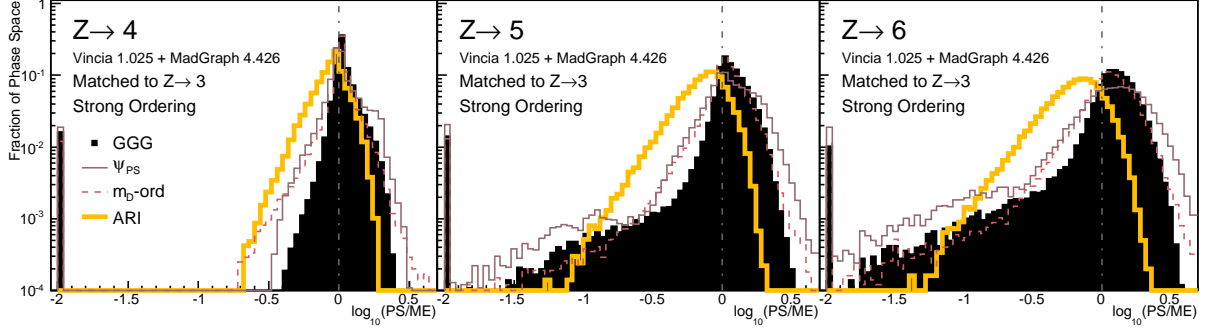


Figure 10: Strongly ordered parton showers compared to matrix elements. Distribution of  $\log_{10}(\text{PS}/\text{ME})$  in a flat phase-space scan. Contents normalized by the number of generated points. Spikes on the far left represent the underflow bin — dead zones in the shower approximations. Gluon emission only. Matrix-element weights from MADGRAPH [52, 53], leading color (no sum over color permutations).

We use the kinematics maps defined in ref. [33],

$$\psi_{\text{AR}} = \frac{E_k^2}{E_i^2 + E_k^2}(\pi - \theta_{ik}), \quad (85)$$

$$\psi_{\text{PS}} = \left\{ \begin{array}{ll} 0 & ; s_{ij} > s_{jk}, \\ \pi - \theta_{ik} & ; s_{ij} < s_{jk}. \end{array} \right\} \quad (86)$$

where  $\theta_{ik}$  is the angle between the after-branching parents in the CM frame of the branching. We show the results of these comparisons in fig. 10, for four different shower approximations:

- *GGG*:  $p_{\perp}$ -ordering using default VINCIA settings, i.e., the GGG antenna functions and the  $\psi_{\text{AR}}$  kinematics map for all branchings. I.e., the parents share the recoil in proportion to their energies in the CM of the dipole-antenna.
- $\psi_{\text{PS}}$   $p_{\perp}$ -ordering using the GGG antenna functions and the parton-shower-like (PS) longitudinal kinematics map. I.e., the parent with the largest invariant mass with respect to the emitted parton recoils only longitudinally.
- $m_D\text{-ord}$ :  $m_D$ -ordering using the GGG antenna functions and the  $\psi_{\text{AR}}$  kinematics map.
- *ARI*:  $p_{\perp}$ -ordering using our best imitation of the what the real ARIADNE program does. It uses  $p_{\perp}$ -ordering, but with the ARIADNE radiation functions instead of the GGG ones, and it also uses a special recoil strategy, as follows; for  $qg$  dipoles, the quark always takes the entire recoil (in the CM of the dipole), whereas for  $gg$  dipoles, the  $\psi_{\text{AR}}$  angle is used to distribute the recoil.

In all cases, we compare to one leading-color (LC) matrix element, i.e., before summing over colors, and with all color factors having been divided out. We present an extensive set of comparisons for different ordering variables in appendix A.

The two bins around zero correspond to the parton-shower approximation having less than a 10% deviation from the full matrix element. At four partons, on the left-hand pane,

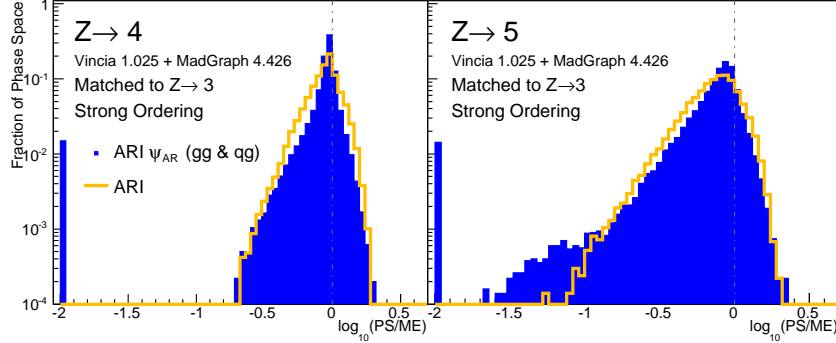


Figure 11: Strongly ordered parton showers, using the ARIADNE radiation functions and two different recoil strategies, compared to matrix elements. Distribution of  $\log_{10}(\text{PS}/\text{ME})$  in a flat phase-space scan. Contents normalized by the number of generated points. Gluon emission only. Matrix-element weights from MADGRAPH [52, 53], leading color (no sum over color permutations).

these two bins contain over 35-60% of the sampled phase-space points, depending on the approximation, with tails extending out towards larger deviations. The spikes at the extreme left edge of the plots represent the underflow bin, including  $-\infty$ , which corresponds to zones in which all of the possible shower histories have been removed by the strong-ordering condition. Such dead zones are characteristic of (ordered) LL parton showers, when the ordering variable is more restrictive than pure phase space. We shall later discuss how to remove them while simultaneously improving the approximation in the ordered region as well.

For all multiplicities, the default  $p_{\perp}$ -ordering with the antenna-like ARIADNE recoil map appears to generate the best overall agreement (narrowest distribution). The parton-shower-like longitudinal recoil map (thin solid line labeled  $\psi_{\text{PS}}$ ), following the spirit of PYTHIA 6 and showers based on CS partitioned dipoles and the dipole-mass ordering (dashed line labeled  $m_D\text{-ord}$ ) give slightly worse agreement (wider distributions).

The “ARI” case (thick solid line) has no dead zone for this process (due to the special kinematics map), but it also appears to generate a somewhat wider, and systematically softer (shifted to the left) distribution, than the GGG ones. To examine further whether this is an effect of the intrinsically softer radiation functions used in ARIADNE (as shown in ref. [44]), or of the special recoil strategy employed by it, we plot in fig. 11 the result for 4 and 5 partons using the ARIADNE radiation functions, either with the default ARIADNE recoil strategy (using  $\psi_{\text{AR}}$  for  $gg$  dipoles only, with the quark recoiling for  $qg$  ones — thick solid line, as above) or just using  $\psi_{\text{AR}}$  for all dipoles (solid histogram). From this comparison, we conclude that there is no significant advantage in assigning all the recoil to the quark in  $qg$  dipoles. Although it removes the dead zone, together with a tail of largely undercounted events, the peak is actually degraded slightly, which we interpret as indicating a worse agreement with the matrix elements close to the singular regions. Physically, this could be consistent with the quark direction having to remain unchanged when the gluon branches collinearly. The position of the peak, slightly to the left of zero, however, is unchanged. This is consistent with the overall “softness” of the approximation being driven mainly by the finite terms in the radiation functions, and not by the choice of kinematics map. It is therefore quite possible that one could find another



process in which the finite terms in the GGG functions would be too large, and the ones in the ARIADNE ones just right.

Returning to fig. 10, as the number of emissions grows, there remains a peak near ME/PS = 1 (note in particular the logarithmic  $y$  axis), but the width of the distribution grows progressively larger, indicating that there is a larger number of individual phase-space points in which the pure shower is not in agreement with the matrix element. These could be due either to subleading logs, or to finite terms in the higher-body matrix elements, not captured by the pure shower. Recall, however, that, since we are looking at a flat phase-space scan, we are biased towards the regions of phase space where matrix element corrections are important, with the strongly ordered regions occupying a progressively smaller volume of the total sampled space. Thus, we interpret this broadening of the weight distribution not so much as a sign of any breakdown in the shower approximation itself, but rather as illustrating why it is desirable to match to fixed-order matrix elements, a point to which we return below.

## 4 Improved Showering

### 4.1 Improving the Logarithmic Accuracy: $2 \rightarrow 3$

A complete set of second-order  $2 \rightarrow 3$  (one-loop) and  $2 \rightarrow 4$  (tree-level) dipole-antenna splitting functions is given in ref. [37]. Ultimately, a matching to these functions to all orders in the shower would be required to reach formal precision beyond LL, but we note that a simpler, partial matching can already be carried out at the  $2 \rightarrow 3$  level, to the terms generated purely by the running of the coupling.

These terms can be uniquely identified both in the shower expansion and in the fixed-order antenna functions by the fact that they are proportional to the QCD one-loop-running coefficient  $b_0$  (57), which appears in the expansion

$$\alpha_s(\mu_1^2) = \alpha_s(\mu_2^2) \left[ 1 - \alpha_s b_0 \ln \left( \frac{\mu_1^2}{\mu_2^2} \right) + \mathcal{O}(\alpha_s^2) + \dots \right]. \quad (87)$$

By matching the terms arising from the expansion of  $\alpha_s$  in the shower to the actual  $b_0$ -dependent pieces of the one-loop antenna functions, we obtain a set of universal corrections at the one-loop level which stabilize the scale dependence of the resulting calculation to next-to-leading logarithmic (NLL) accuracy.

In particular, we may extract the relevant terms of the one-loop antenna functions by isolating their  $n_f$ -dependent pieces, which are generated purely by quark loops. For gluon emission, the one-loop antennae in ref. [37] all contain the following  $n_f$ -dependent logarithms,

$$n_f \frac{1}{6} (\ln y_{ij} + \ln y_{jk}) a_{ijk}^0 = n_f \frac{1}{6} \ln \left( \frac{p_\perp^2}{s_{IK}} \right) a_{ijk}^0, \quad (88)$$

where  $a_{ijk}^0$  denotes the corresponding tree-level antenna function, and  $p_\perp$  is defined exactly as in ARIADNE and VINCIA, i.e.,

$$p_\perp^2 = \frac{s_{ij}s_{jk}}{s_{IK}}. \quad (89)$$

Because the default renormalization scale used in ref. [37] is

$$\mu_{\text{GGG}}^2 = s_{IK}, \quad (90)$$

a redefinition of the renormalization scale from  $s_{IK}$  to  $p_\perp^2$  would absorb the entire term, eq. (88), into the definition of the coupling at tree level. Simultaneously, the  $N_C$ -dependent logarithms generated by the same choice can easily be verified to cancel equivalent pieces in the one-loop function, however the latter cancellation is not exact due to the presence of additional terms in the one-loop function which do not originate from renormalization. (To absorb also these terms would require full one-loop matching.) We note that this is nothing but a “renormalization-group-improved” effective redefinition of the tree-level coupling which has been known for a long time [54] and is the reason why the default renormalization scale both in VINCIA and in virtually all other Monte Carlos<sup>4</sup> is  $p_\perp^2$ .

However, rather than just hardcoding one particular choice, we shall here instead interpret it in the context of a second-order matching condition, which will allow us the flexibility to estimate the remaining uncertainties by varying the scale freely and partly canceling the dependence on it via the matching condition. This effectively pushes the effects of the scale variation one order higher in QCD.

The relevant (partial) matching equation for gluon emission is

$$\alpha_s(p_\perp^2)a_{ijk}^0 = \alpha_s(\mu_{\text{PS}}^2)P_g^{\text{NLL}\mu}a_{ijk}^0, \quad (91)$$

which, expanded to first order, easily yields the following form for the scale-stabilizing multiplicative factor:

$$\text{gluon emission : } P_g^{\text{NLL}\mu} = \left( 1 + \alpha_s b_0 \ln \left( \frac{\mu_{\text{PS}}^2}{p_\perp^2} \right) \right), \quad (92)$$

where  $\mu_{\text{PS}}$  is the renormalization scale used by the shower evolution and the renormalization scale of  $\alpha_s$  in the correction term constitutes an ambiguity of yet higher order. In order to be conservative, we wish to make the effects of the scale cancellation produced by this term as small as possible. We therefore evaluate the  $\alpha_s$  in eq. (92) at the largest scale in the  $2 \rightarrow 3$  splitting,  $s_{IK}$ . Any further optimization would amount to a beyond-NLL effect.

Qualitatively, the scale stabilization works as follows. If  $\mu_{\text{PS}}$  is chosen large, then the correction factor, eq. (92), becomes greater than one, hence partly compensating for the lower  $\alpha_s$  value. Conversely, if a very large  $\alpha_s$  is used at the LL level, the logarithm in the correction term becomes negative, and again acts to stabilize the result. We note that, in extreme cases, the correction term could in fact become larger than unity. As this would imply a divergent perturbative expansion anyway, VINCIA therefore restricts the range of allowed values to  $0 < P^{\text{NLL}\mu} < 2$ .

For gluon splitting to quarks, the one-loop antenna functions do not contain universal logarithms in  $p_\perp$ . Instead, the universal  $n_f$ -dependent terms are [37]

$$n_f \frac{2}{3} \ln(y_{q\bar{q}}) = n_f \frac{2}{3} \ln \left( \frac{m_{q\bar{q}}^2}{s_{IK}} \right), \quad (93)$$

where  $m_{q\bar{q}}$  is the invariant mass of the quark-antiquark pair produced in the splitting. In this case, we see that the “optimal choice” of renormalization scale is not  $p_\perp^2$  but  $m_{q\bar{q}}^2$ . The

---

<sup>4</sup>Note, however, that eq. (89) is the only definition of  $p_\perp$  that *exactly* matches the actual  $b_0$ -dependent one-loop terms. Parton shower models not based on the dipole-antenna picture, which make approximations to this  $p_\perp$  definition, will therefore necessarily have small  $b_0$ -dependent remainders left uncanceled.

corresponding scale-stabilizing term for gluon splitting is therefore

$$\text{gluon splitting : } P_q^{\text{NLL}\mu} = \left( 1 + \alpha_s b_0 \ln \left( \frac{\mu_{\text{PS}}^2}{m_{q\bar{q}}^2} \right) \right) . \quad (94)$$

Again, one can easily verify that the  $N_C$ -dependent logarithms generated by this choice do partly cancel similar pieces in the same one-loop antenna functions, and again, the latter cancellation is not exact due to additional pieces unrelated to renormalization. Finally, we note that since

$$m_{q\bar{q}}^2 > p_\perp^2 \quad (95)$$

over all of phase space, the effect of this stabilization is to reduce the total number of gluon splittings slightly, as compared to what would be obtained without the stabilization terms and using  $\alpha_s(p_\perp^2)$  for both gluon emissions and gluon splittings, as is traditionally done in shower Monte Carlos.

These scale stabilizing terms have been implemented in the VINCIA code for all  $2 \rightarrow 3$  splittings since version 1.020, with an option to switch them on and off to investigate their effects. The default in the code is to leave them on.

Let us emphasize again that this is not a complete one-loop matching. With the scale variation, we seek only to evaluate — the scale variation. We do not make any assumption that this variation is representative of the entire remaining uncertainty, on which we have several other, independent, handles, to which we shall return below. The procedure of employing scale variation alone as a (poor man’s) estimate of the full uncertainty is obsolete in this framework.

## 4.2 Improving the Logarithmic Accuracy: $2 \rightarrow 4$

While parton emission using trial branchings can easily be made to cover the full phase space for a single emission, the same is not true for multiple emissions. Due to the requirement of strong ordering, some regions of phase space may be inaccessible, leading to so-called dead zones. This also happens in strongly ordered dipole-antenna showers, for example in regions where several emissions happen at closely similar emission scales, as shown in ref. [34, 55]. Since gluon emission and gluon splitting processes have different singularity structures and are treated slightly differently, we first consider the dominant case, that of gluon emission. We then give a few brief remarks about gluon splitting, although we defer most of the details of that discussion to another publication [56].

### 4.2.1 Gluon Emission

A plot from ref. [34], showing the dead zone for  $Z \rightarrow qgg\bar{q}$  in a  $p_\perp$ -ordered dipole-antenna shower, is reproduced in the left-hand pane of Fig. 12. Each bin of this 2D histogram shows the value of  $R_4$ , eq. (83), averaged over all 4-parton phase space points that populate that bin. The black zone above the strong-ordering line corresponds exactly to the spike on the left-hand edge of the plots in fig. 10 (the underflow bin).

If one simply removes the strong-ordering condition, equivalent to ordering the emissions only by the nesting of the factorized phase spaces, the dead zone obviously disappears. However, this comes at the price of introducing a substantial double counting, which also extends deep into the ordered region. We illustrate this on the plot in the right-hand pane of fig. 12,

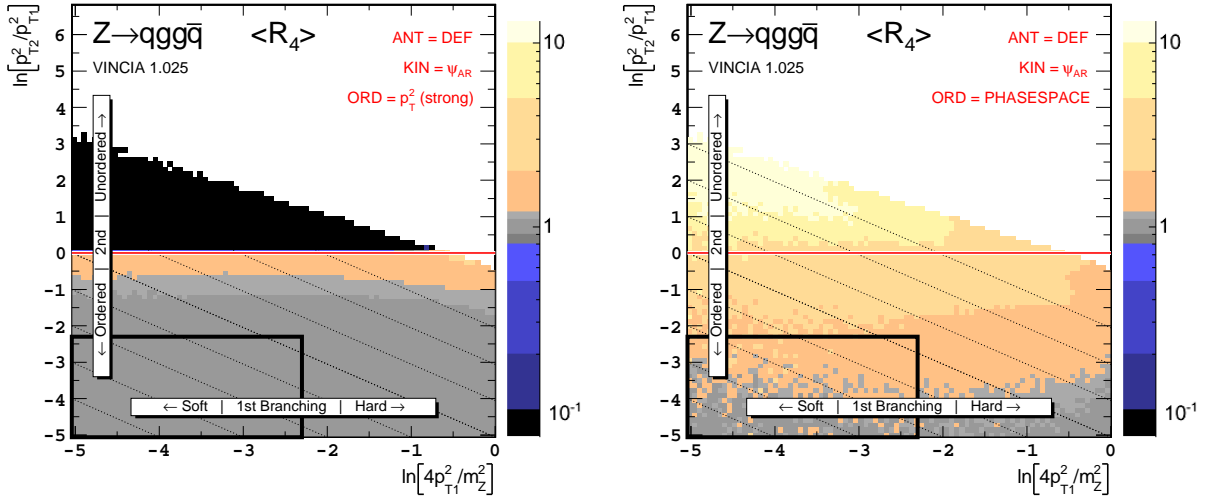


Figure 12: The value of  $\langle R_4 \rangle$  differentially over 4-parton phase space, with  $p_\perp$  ratios characterizing the first and second emissions on the  $x$  and  $y$  axes, respectively. Strong ordering in  $p_\perp$  (left) compared to no ordering (right). Gluon emission only. Matrix-element weights from MADGRAPH [52, 53], leading color (no sum over color permutations).

in which  $\langle R_4 \rangle \gg 1$  both in the unordered region as well as in parts of the ordered region where the agreement was previously good. Clearly, therefore, the ordered description, in the left-hand pane, is a better overall approximation to QCD, even if it does include a dead zone.

In order to go further, we must understand the physics behind the ordered and unordered approximations to the matrix elements. Why is ordering so important? The first exploration of this goes back to the early eighties. Then, it was realized that parton showers ordered only in parton virtuality (which is equivalent to a pure phase-space ordering in that language) represent an essentially incoherent addition of independently radiating monopoles. In phase-space regions where the contributions from each such monopole term are comparable, interference effects can become large. Without them, the pure phase-space ordered shower gives a substantial overcounting of those regions, as compared to matrix elements [28, 29]. As Marchesini and Webber showed [41], this double counting can be approximately identified with terms corresponding to non-angular-ordered emissions, and hence the procedure to impose coherence on traditional parton showers has since been to impose such an ordering, either implicitly by the choice of evolution variable, as in HERWIG, or explicitly as a veto on the generated trial emissions, as in PYTHIA.

In dipole-based shower models, soft coherence inside each dipole is guaranteed, regardless of the ordering variable, by using dipole-based radiation functions instead of the DGLAP ones, but the problem still exists; it has just been pushed one order higher in the number of interfering partons (see, e.g., refs. [34, 50]). With pure phase-space ordering, dipole-antenna showers essentially represent an incoherent addition of independently radiating *dipoles*. An independent addition of two such dipoles would result in a substantial overcounting in all regions where several such dipole terms contribute simultaneously at similar levels, i.e., in regions where dipole-dipole interference effects (or, equivalently, multipole effects) would be important. Again, it would be interesting to investigate whether some variant of angular

ordering could be used to restore a more coherent behavior, but in the context of the dipole-antenna formalism we develop here, we have not been able to find such a solution. In part, this owes to a strict ordering in angle having some disadvantages in our language; being frame-dependent, it would not respect the Lorentz-invariant dipole phase-space factorization we rely on, and it also classifies a subset of infinitely soft and/or collinear emissions as happening at finite values of the evolution variable, which would lead to ill-defined evolution integrals, see, e.g., ref. [34].

Instead, let us recall the basic motivation for angular ordering: to approximately remove the double counting caused by incoherent addition of interfering diagrams of similar magnitudes. In the parton shower language, each such term is associated with a divergence in the energy times angle of the emission. In the region where several terms would nominally be large, the angular ordering requirement forces at most one of them to contribute — approximating the destructive-interference effects by killing the non-ordered contributions. In dipole-based approaches, however, the leading divergence of the gluon radiation functions occurs unambiguously in the  $p_\perp$  of the emitted gluon. It therefore seems sensible to use  $p_\perp$  as the measure for the ordering, and thereby implicitly for the size of each of the contributing terms. As can be seen from the left-hand pane of fig. 12, an ordering in  $p_\perp$ , yields a quite good average approximation to the full  $2 \rightarrow 4$  matrix elements over most of phase space.

We included the above discussion to motivate that, while there is an important physics issue behind strong ordering and also behind the choice of functional form of the ordering variable, there is nothing particularly important about imposing it as a step function in that variable. On the contrary, the actual destructive-interference terms in the matrix elements exhibit a smooth behavior. To remove dead zones to all orders while simultaneously improving the shower approximation also in the ordered region, we therefore propose to change the condition of strong ordering to a smoother condition with the same limiting behaviors.

Specifically, while we retain strong ordering as an option in VINCIA, by default we replace the strong-ordering condition of conventional parton showers in gluon emission by the smooth suppression factor

$$\text{Gluon Emission} \quad : \quad \Theta_{\text{ord}} P^{\text{LL}} \rightarrow P_{\text{imp}} P^{\text{LL}} = \frac{\hat{p}_\perp^2}{\hat{p}_\perp^2 + p_\perp^2} P^{\text{LL}} , \quad (96)$$

where  $\hat{p}_\perp$  is the smallest  $p_\perp$  scale among all the color-connected parton triplets in the parent configuration (i.e., a global measure of the “current”  $p_\perp$  scale of that topology);  $p_\perp^2$  is the scale of the trial  $2 \rightarrow 3$  emission under consideration; and  $P^{\text{LL}}$  is defined in eq. (82). Note that if the trial emission is not accepted, the evolution continues starting at the scale of the failed trial, as required by the veto algorithm. Only after a branching has been accepted, when we change from the  $n$ - to the  $(n+1)$ -parton phase space, do we allow the evolution to be restarted from the full phase space of each dipole antenna.

Since the antenna function for the previous branching is proportional to  $1/\hat{p}_\perp^2$ , the net effect of this term, in the unordered region, is to replace that divergence by a damped factor,  $1/(\hat{p}_\perp^2 + p_\perp^2)$ . The correction is thus constructed such that  $P^{\text{LL}}$  remains unmodified in the strongly ordered limit  $p_\perp \ll \hat{p}_\perp$ , and therefore will not affect the leading-logarithmic behavior of the parton shower. It then drops off to  $\frac{1}{2}P^{\text{LL}}$  for  $p_\perp = \hat{p}_\perp$ , and finally tends smoothly to zero in the limit of extreme unordering,  $p_\perp \gg \hat{p}_\perp$ .

The ratio of the resulting shower to matrix elements is shown in the left-hand pane of fig. 13. Comparing this distribution with those in fig. 12, we indeed see that not only has the

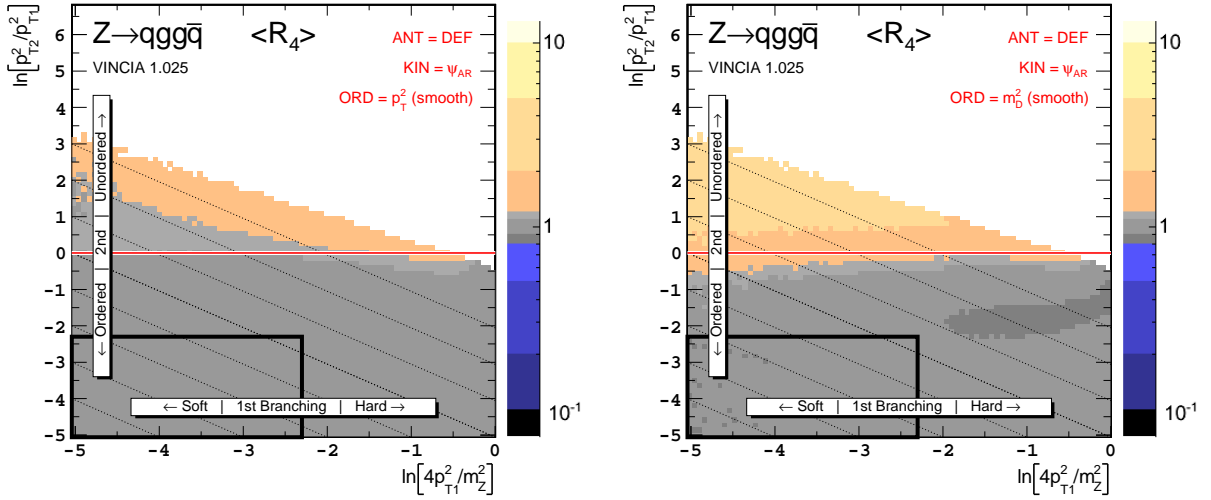


Figure 13: The value of  $\langle R_4 \rangle$  differentially over 4-parton phase space, with  $p_\perp$  ratios characterizing the first and second emissions on the  $x$  and  $y$  axes, respectively. Smooth ordering in  $p_\perp$  (left) compared to smooth ordering in  $m_D$  (right). Gluon emission only. Matrix-element weights from MADGRAPH [52, 53], leading color (no sum over color permutations).

dead zone been removed, without introducing any serious overcounting of it, but the quality of the approximation has also been improved inside the ordered region.

For completeness, in the right-hand pane of fig. (13), we also show how the approximation would have looked if the alternative measure  $m_D^2 = 2 \min(m_{ij}^2, m_{jk}^2)$  had been used instead of  $p_\perp$  in the suppression factor eq. (96). Although there is still clearly an improvement over the pure phase-space-ordered case — the dead zone has been eliminated — it is much less convincing than for  $p_\perp$ , as the weights are larger in the region above the thin horizontal red line.

To illustrate how this approximation evolves with parton multiplicity, we show the distribution of the log of the PS/ME ratio with this modification, in fig. 14, for  $Z \rightarrow 4, 5$ , and 6 partons, including only leading-color gluon emission. One observes a marked improvement with respect to the strongly ordered approximations, fig. 10, for all multiplicities. In particular, not only the dead zones but also the large tails towards low PS/ME ratios visible in the higher-multiplicity plots in fig. 10 have disappeared, which we interpret as a confirmation that the logarithmic accuracy of the approximation has indeed been improved. Notice, however, that the ARIADNE functions (where we have here used the  $\psi_{AR}$  kinematics map for both  $qg$  and  $gg$  antennae, hence the explicit label on the plot) still tend to shift the shower approximations systematically towards softer values, whereas the GGG ones remain closer to the matrix elements.

#### 4.2.2 Gluon Splitting

For gluon splitting, there is no soft singularity, only a collinear one. This means there is now only a single log-enhancement (instead of a double log) driving the approximation and competing with the (uncontrolled) finite terms. It is therefore to be expected that the LL

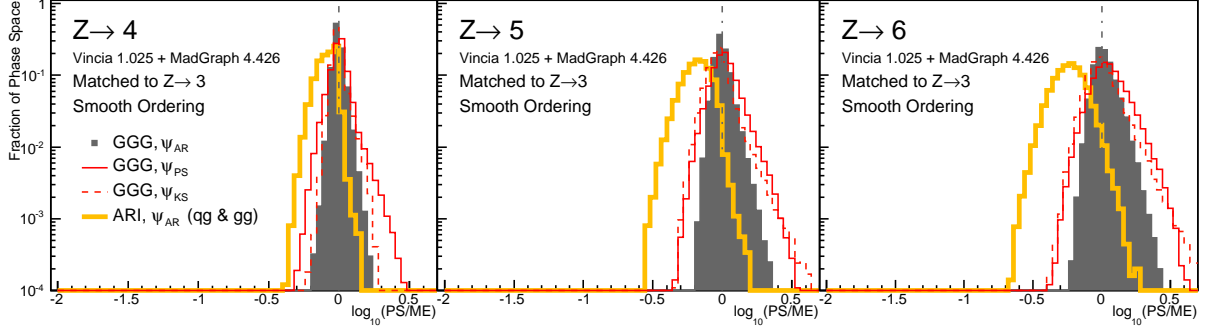


Figure 14: Smoothly ordered parton showers compared to matrix elements. Distribution of  $\log_{10}(\text{PS}/\text{ME})$  in a flat phase-space scan. Contents normalized by the number of generated points. Gluon emission only. Matrix-element weights from MADGRAPH [52,53], leading color (no sum over color permutations). Compare to fig. 10 for strong ordering.

approximation to gluon splitting is significantly worse, over more of phase space, than is the case for gluon emission.

Furthermore, if the two neighboring dipole-antennae that share the splitting gluon are very *unequal* in size, e.g., as a result of a preceding close-to-collinear branching, then higher-order matrix elements and splitting functions unambiguously indicate that the total gluon splitting probability is significantly suppressed. This is not taken into account when treating the two antennae as independent radiators. This effect was already noted by the authors of ARIADNE, and a first attempt at including it approximately was made by applying the following additional factor to gluon splittings in ARIADNE, in addition to the strong-ordering condition,

$$\text{Gluon Splitting (ARIADNE)} : \Theta_{\text{ord}} P^{LL} \rightarrow \Theta_{\text{ord}} P_{\text{Ari}} P^{LL} = \Theta_{\text{ord}} \frac{2s_N}{s_{IK} + s_N} P^{LL} , \quad (97)$$

where  $s_N$  is the invariant mass squared of the neighboring dipole-antenna that shares the gluon splitting, and  $s_{IK}$  is the invariant mass squared of the dipole-antenna in which the splitting occurs. The additional factor reduces to unity when the two neighboring invariants are similar; it suppresses splittings in an antenna whose neighbor has a very small invariant mass; and it slightly enhances splittings in dipole-antennae whose neighbors have very large invariant masses. This modification is *ad hoc*, but formally is beyond LL, and thus does not spoil the shower's properties at this order. In practice, it greatly improves the shower's approximation to matrix elements.

For our purposes here, we first replace the  $\Theta$  function in ARIADNE by the same smooth unordering suppression factor we used above,

$$\text{Gluon Splitting} : \Theta_{\text{ord}} P_{LL} \rightarrow P_{\text{imp}} P_{\text{Ari}} P_{LL} , \quad (98)$$

which gives an overall approximation at least as good as that of ARIADNE, without any dead zones. The overall agreement between even this improved gluon splitting and explicit matrix elements is still far from perfect, however, due to the intrinsically smaller relative size of the logs driving the approximation. We are in the process of preparing a more dedicated study of this issue, including quark mass effects [56], and hence defer further discussion of this topic



for the time being. For later convenience, we define this adjustment factor to be unity for gluon emission,

$$\text{Gluon Emission : } P_{\text{Ari}} = 1, \quad (99)$$

$$\text{Gluon Splitting : } P_{\text{Ari}} = \frac{2s_N}{s_{IK} + s_N}. \quad (100)$$

### 4.3 Subleading Color

In the dipole-antenna formalism, a general result [57] is that the subleading-colour effects in a single  $qgg\dots g\bar{q}$  chain can be taken into account by including a subleading antenna spanned directly between the  $q$  and  $\bar{q}$  associated with a color factor  $-1/N_C^2$  relative to the leading-color antennae (which are proportional to  $C_A$ ).

However, in the context of a probabilistic framework, such as shower Monte Carlo algorithms, the negative sign of this antenna means it cannot be treated on the same footing as the (positive-definite) LC ones<sup>5</sup>. Moreover, it is not possible to define a unique LC color assignment to the emissions generated by it, and hence the subsequent shower evolution (and the infinite-order approximations generated by it) would be ill-defined.

Instead, in traditional parton-shower applications, this correction is partly treated by associating quark emission terms with  $C_F$  instead of  $C_A$ , thereby correctly absorbing the collinear singularities of the correction term into the LC ones, at the price of introducing a subleading-color ambiguity in the soft singularity structure. To improve on this, one could imagine, e.g., trying to be more clever about in which phase-space regions to use  $C_F$  and in which  $C_A$  even for emissions off gluons [58]. But in both cases the simplicity of the correction term would then be less explicit.

Instead, we here attempt to reabsorb the subleading-color correction systematically into the leading-color antennae, using a smooth partitioning, which integrates to reproduce the double poles of the corresponding subleading-color one-loop antenna functions.

Consider the evolution integral off an  $n$ -parton configuration in the massless approximation:

$$\sum_{IK \in LC} \int ds_{ij} ds_{jk} \frac{\tilde{a}_{IK}(y_{ij}, y_{jk})}{s_{IK}^2}, \quad (101)$$

where  $\tilde{a}$  is a dimensionless antenna function, and the scaled invariants are defined by  $y_{ij} = s_{ij}/s_{ijk} = s_{ij}/s_{IK}$ , and where the sum is over all color-connected pairs, that is all LC antennae. Changing integration variables to dimensionless quantities, the integration measure becomes independent of the size of the antenna phase spaces and we may replace the sum of integrals by the integral of a sum, to which we can add a subleading-color piece,

$$\int dy_{ij} dy_{jk} \left[ \sum_{IK \in LC} \tilde{a}_{IK}(y_{ij}, y_{jk}) - \frac{1}{N_C^2} \tilde{a}_{NLC}(y_{ij}, y_{jk}) \right]. \quad (102)$$

---

<sup>5</sup>One could in principle imagine flipping the sign of the event weight when generating emissions with it, but such a procedure would drive the convergence rate of the resulting algorithm to become infinitely slow at asymptotically large energies.

Finally, we may partition the correction term among the LC pieces by introducing a partitioning function,  $f$ ,

$$= \int dy_{ij} dy_{jk} \left[ \sum_{IK \in LC} \tilde{a}_{IK}(y_{ij}, y_{jk}) \underbrace{\left( 1 - \frac{f_{IK} \tilde{a}_{NLC}(y_{ij}, y_{jk})}{N_C^2 \tilde{a}_{IK}(y_{ij}, y_{jk})} \right)}_{P_{NLC}} \right], \quad (103)$$

where the underbraced term can now be implemented straightforwardly as a veto probability,  $P_{NLC}$ , in the shower evolution.

For  $f$  to be a consistent partitioning, it must give unity when summed over all the LC antennae. The prescription we use is to absorb corrections into each term in proportion to the relative size of that term, i.e.,

$$f_{IK} = \frac{\tilde{a}_{IK}(y_{ij}, y_{jk})}{\sum_{AB \in LC} \tilde{a}_{AB}(y_{ar}, y_{rb})}. \quad (104)$$

For the functional form of  $\tilde{a}$ , we give two options,

1. Only the Eikonal part of the  $q\bar{q}$  antenna function is included in  $\tilde{a}_{NLC}$ , corresponding to

$$\tilde{a}_{NLC}(y_{ij}, y_{jk}) = \frac{2(1 - y_{ij} - y_{jk})}{y_{ij}y_{jk}} \quad (105)$$

This integrates to give the correct  $1/\varepsilon^2$  poles of the  $1/N_C^2$  piece of the one-loop antenna function (called  $\tilde{A}_3^1$  in ref. [37]).

2. The full  $q\bar{q}$  antenna function (called  $A_3^0$  in [37]) is included in  $\tilde{a}_{NLC}$ , corresponding to

$$\tilde{a}_{NLC}(y_{ij}, y_{jk}) = \frac{2(1 - y_{ij} - y_{jk})}{y_{ij}y_{jk}} + \frac{y_{ij}}{y_{jk}} + \frac{y_{jk}}{y_{ij}} \quad (106)$$

This integrates to give the correct  $1/\varepsilon^2$  and  $1/\varepsilon$  poles of the  $1/N_C^2$  piece of the one-loop antenna function (called  $\tilde{A}_3^1$  in ref. [37]).

For the corrected emission probability to be positive definite, the condition

$$\tilde{a}_{NLC} < \frac{N_C^2}{f_{IK}} \tilde{a}_{IK} \quad (107)$$

must be fulfilled. The Eikonal terms are guaranteed to respect this by a wide margin, but there can in principle be subleading differences between  $\tilde{a}_{IK}$  and  $\tilde{a}_{NLC}$  at the level of single poles and/or finite terms, both of which can be influenced to some extent by user-controlled settings in VINCIA. Although we have not encountered any problems with such corrections becoming large in our own studies so far, we have inserted a numerical safeguard in the code, limiting the size of each NLC correction to be at most half of the corresponding LC term.

We compare the shower expansion corrected as in eq. (103), using the definition of  $\tilde{a}_{NLC}$  given by eq. (106), to color-summed matrix elements in Fig. 15, for  $Z \rightarrow 5$  and  $Z \rightarrow 6$  partons (gluon emission only), for both the strong- and smooth-ordering options. For reference, we show the pure LC shower expansions as well, as in figs. 10 and 14, although we here set both

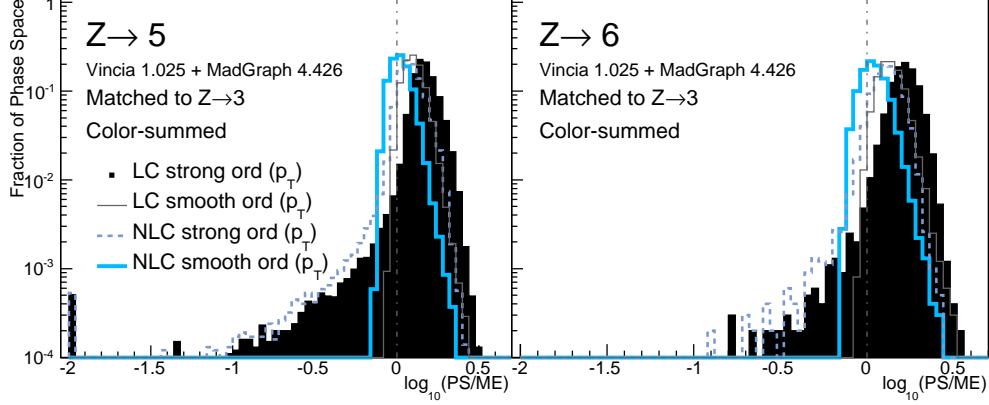


Figure 15: LC and NLC parton showers compared to matrix elements. Distribution of  $\log_{10}(\text{PS}/\text{ME})$  in a flat phase-space scan. Contents normalized by the number of generated points. Gluon emission only. Matrix-element weights from MADGRAPH [52, 53], full color (summed over color permutations). Compare to figs. 10 and 14. Note: the black histogram here does not look identical to the one in fig. 10; this is because the distribution shown here is after summation over all color-permutations. Also, the shower expansion here uses  $C_A$  for both  $qg$  and  $gg$  emission antennae. The same is true for the thin solid line, as compared to the solid histogram in fig. 14.

the  $qg$  and  $gg$  color factors equal to  $C_A$ , to better illustrate what happens when only the NLC correction is switched on and off. Note also that the previous comparisons in this paper were made to leading-color matrix elements for each individual color structure separately. Such a comparison is not meaningful once color interference effects are taken into account, and hence we are here using the full color-summed matrix elements, and are likewise summing over permutations of the gluon momenta in the shower expansion.

Firstly, we notice that the LC shower expansions do indeed overcount the matrix elements if we just use  $C_A$  for both  $qg$  and  $gg$  antennae, as expected (the solid filled histogram and thin solid lines are shifted to the right of the vertical dot-dashed line that represents perfect agreement). When we switch on the NLC correction in the manner described above, both the strongly and smoothly ordered approximations are noticeably improved, cf. the blue dashed and thick solid curve, respectively. The NLC correction is therefore switched on by default in the VINCIA code.

The procedure described above is correct for the case of a single  $qgg\dots g\bar{q}$  chain and then correctly takes into account the infrared singularities arising from the first subleading-color term, which is proportional to  $1/N_C^2$ . We refer to this modification as “next-to-leading color” or NLC. (Strictly speaking, there are also corrections proportional to  $1/N_C$ , but these are already taken into account in leading-color showers by including  $g \rightarrow q\bar{q}$  splittings.) However, due to the inherent ambiguity in assigning a color flow to these corrections even in the soft limit, we cannot be certain that further subleading terms are also correctly described. I.e., we do not expect to reproduce the correct  $1/N_C^4$  terms in all singular limits.

When there are several colour chains, such as after a  $g \rightarrow q\bar{q}$  splitting (and hence already suppressed by at least  $1/N_C$ ), we generalize the treatment to each chain separately. That is,

we do not at this point attempt to include interference effects *between* different color-singlet systems.

## 5 Matching

In this section, we describe our strategy for incorporating a detailed matching to tree-level matrix elements. The philosophy is similar to that pioneered by Sjöstrand in refs. [28,29], and hence also to the POWHEG formalism, but we here generalize the method to include arbitrary-multiplicity tree-level matrix elements. The inclusion of the NLO virtual corrections to the lowest multiplicity was treated in ref. [33] for an arbitrary tree-level matching strategy.

### 5.1 Matching Strategies

Given a parton shower and a matrix-element generator, there are fundamentally three different ways in which we can consider matching the two:

1. *Unitarity*: The oldest approach [28, 29] consists of working out the shower approximation to a given fixed order, and correcting the shower splitting functions at that order by a multiplicative factor given by the ratio of the matrix element to the shower approximation, phase-space point by phase-space point. We may sketch this as

$$\text{Matched} = \text{Approximate} \frac{\text{Exact}}{\text{Approximate}} . \quad (108)$$

That is, the shower approximation is essentially used as a pre-weighted (stratified) all-orders phase-space generator, on which a more exact answer can subsequently be imprinted order by order in perturbation theory. In our notation [33], this translates to applying the following correction factor to each antenna function  $a_i$  (or any other kind of shower splitting kernel)

$$a_i \rightarrow a_i P_n^{\text{ME}} \quad , \quad P_n^{\text{ME}} = \frac{|M_n|^2}{\sum_j a_j |M_{n-1}|^2} , \quad (109)$$

where the sum over  $j$  runs over all possible ways the shower could have generated the  $n$ -parton state from  $n-1$  partons<sup>6</sup>. So long as the adjustment factors  $P^{\text{ME}}$  are less than or equal to one, they can be interpreted as probabilities, and the adjustment can be accomplished by means of the veto algorithm Monte-Carlo technique. This constraint can essentially always be satisfied through appropriate choice of the finite terms in the antenna functions  $a_i$ .

When these correction factors are inserted back into the shower evolution, they guarantee that the shower evolution off  $n-1$  partons correctly reproduces the  $n$ -parton matrix elements, without the need to generate any separate  $n$ -parton samples. Moreover, since the corrections modify the actual shower evolution kernels, the corrections are *resummed* in the Sudakov exponential, and finally, since the shower is *unitary*, an initially unweighted sample of  $(n-1)$ -parton configurations remains unweighted, with no need for a separate event-unweighting or event-rejection step. (Technically, the

---

<sup>6</sup>Note, however, that this gets substantially more complicated if the shower process is not completely Markovian, a point we shall return to.

exponentiation allows beyond-LL corrections to be resummed, thus improving the logarithmic accuracy of the result, while the explicit constraint of unitarity ensures that the additional non-logarithmic terms that are also exponentiated by this procedure do not lead to disasters.) There are thus several quite desirable features to this kind of matching strategy, which is currently employed by PYTHIA, POWHEG, and VINCIA. However, since traditional shower expansions quickly get more complicated as a function of the number of emissions, this strategy had only been worked out for a single additional emission prior to this paper (although the MENLOPS strategy [26] does allow to combine a unitary matching of the first emission with traditional non-unitary methods for multi-jet matching). Below, we shall generalize the unitarity method to arbitrary multiplicities and, as a proof of concept, present a concrete implementation spanning four successive emissions, including all subleading color terms.

2. *Subtraction*: Another way of matching two calculations is by subtracting one from the other and correcting by the difference, schematically

$$\text{Matched} = \text{Approximate} + (\text{Exact} - \text{Approximate}) . \quad (110)$$

This looks very much like the structure of an NLO fixed-order calculation, in which the shower approximation plays the role of subtraction terms, and indeed this is what is used in strategies like MC@NLO [22, 59, 60]. In particular since eq. (110) appears much simpler to the fixed-order community than eq. (108), this type of approach has received much more attention than the unitarity-based one above (though, to be fair, the POWHEG [30] approach represents a kind of hybrid between the two). In this approach, the corrections are *not resummed*; the events are *not unweighted* — we can even have negative weights, at phase-space points where the approximation is larger than the exact answer; and we need a *separate phase-space generator* for the  $n$ -parton correction events. And finally, like for the unitarity-based case above, a systematic way of extending this strategy beyond the first additional emission was not previously available. All these issues are, however, less severe than in ordinary NLO approaches, and hence they are not viewed as disadvantages if the point of reference is an NLO computation. Since the correction terms are applied by adding (or subtracting, depending on the sign of the weight) events, we refer to this type of matching strategy as *subtraction*.

3. *Slicing*: The last matching type is based on separating phase space into two regions, one of which is supposed to be mainly described by hard matrix elements and the other of which is supposed to be described by the shower. Basically, this amounts to a subtractive approach in which the shower approximation is set to zero above some scale (effectively a dead zone is forced on the shower by vetoing any emissions above a certain *matching scale*), causing the matched result to be the unsubtracted matrix element in that region, modulo higher-order corrections,

$$\text{Matched (above matching scale)} \sim \text{Exact} (1 + \mathcal{O}(\alpha_s)) , \quad (111)$$

and since the leading behavior of the matrix elements and the shower approximation are assumed to be the same below the matching scale, the small difference between them can be dropped, yielding the pure shower answer in that region,

$$\text{Matched (below matching scale)} = \text{Approximate} + (\text{Exact} - \text{Approximate}) \sim \text{Approximate} . \quad (112)$$

Since this strategy is discontinuous across phase space, a main point here is to ensure that the behavior across the matching scale be as smooth as possible. CKKW showed [6] that it is possible to remove any dependence on the matching scale through NLL precision by careful choices of all ingredients in the matching; technical details of the implementation (affecting the  $\mathcal{O}(\alpha_s)$  terms in eq. (111)) are important [13]. The MLM [4, 18] approach is also an example of this type of matching. However, we note that the slicing strategy inherits almost all of the problems that pure subtraction has; the corrections are *not resummed*, the events are *not unweighted* (but at least we avoid the negative-weight issue), and we need a *separate phase-space generator* for the  $n$ -parton correction events. In addition, the dependence on the unphysical matching scale has appeared, which in general is non-vanishing and may be larger than NLL unless the implementation matches the theoretical algorithm precisely [13]. However, due to the work of CKKW and others [6, 13, 14, 18], a systematic way of extending this strategy beyond the first additional emission *is* available, and a strategy has even been proposed whereby this matching type could be extended to NLO precision [61]. The MENLOPS approach [26] is also available to combine it with POWHEG. Since this type is already well developed, therefore, we shall not consider it further in this paper, but note that one could still obtain it from our formulae for subtractive matching (eq. (22) of ref. [33]), by inserting the appropriate phase-space cutoffs at the matching scale. For this reason, we refer to this strategy as *scale-based* or *slicing*.

To summarize, in this paper, we focus on the extension of the *unitary* matching strategy to arbitrary numbers of emissions at tree level. We shall also include an NLO matching to the Born multiplicity using the prescription from ref. [33].

## 5.2 Matching to Tree-Level Matrix Elements: Leading Color

The formalism we shall describe here represents a generalization of the one presented in ref. [33]. It is based on using the trial generator described in the previous section as a phase-space generator, whose phase-space weights can be expanded to the required order and compared to the matrix-element answer at the same order. A correction can then be imposed before generating the next trial emission. For comparison, most other approaches are currently based on generating separate event samples for different jet multiplicities and then post facto attempting to remove the overlaps (“double counting”) between them. Here, we generate one sample *ab initio*, where every event starts at the lowest multiplicity and is then successively matched up to the desired orders.

Compared to shower evolution, matrix-element (ME) evaluations are computationally intensive. It is therefore desirable that the matching algorithm involve as few ME evaluations as possible. In an ordinary shower approach, the effective weight of each phase-space point depends on all the possible shower histories that could contribute to it, resulting in a factorially increasing dependence on the multiplicity (for each color configuration). In CKKW-type approaches, this is partly circumvented by always selecting only one history, the “most singular one” according to the  $k_t$  algorithm. Since this does not exactly correspond to an inversion of the parton shower, the matching only really addresses the LL overlaps, and the higher-order discrepancies are “removed” by introducing an explicit cut on the phase-space region in which matching is applied, by the so-called “matching scale”, which limits the numerical size that any subleading divergence could attain.

In contrast, since we match at each successive order, each emission (up to the matched orders) will necessitate at least one matrix-element evaluation as well as the corresponding shower weight, which in turn will involve matrix-element evaluations at the preceding orders. At first sight, this may sound extremely expensive. Note, however, that we are doing the matching of “all the samples” once and for all, so that only one “run” will be necessary, rather than a separate one for each multiplicity. (Separate “runs” for different multiplicities would then spread a comparable number of matrix-element evaluations across the different “runs”.) In that context, the scheme should not be more expensive than current ones, provided that a formalism can be found that minimizes the number of matrix-element evaluations that are still necessary to determine the trial weight.

One sufficient condition for minimizing the number of required matrix-element evaluations is the Markov condition: each shower step should depend only on the current  $n$ -parton configuration and not on its previous history. This in turn implies that, in order to compute the trial weight, only the histories one step back have to be considered, rather than all possible clusterings all the way to the Born. As mentioned above, this would not be true of ordinary strongly-ordered parton showers, where the *restart* scale for each configuration would depend on *which* parton was the last emitted one.

A simple prescription that *does* obey the Markov condition is to generate trial emissions for every antenna in the  $n$ -parton configuration over their full phase space, irrespective of the current ordering scale. Without matching, this would lead to a large overcounting, as was illustrated in fig. 12, but with matching, the total shower weight can be calculated and the corresponding matrix-element correction made, with two added benefits: 1) the removal of the strong-ordering condition explicitly prevents any dead zones from appearing in the trial space, and 2) since the trial weight generated this way will represent an overestimate, it will be possible to impose the matching by multiplying by a factor smaller than unity, which can be translated into a probabilistic veto of the trial branching. The net effect is to exponentiate the whole squared matrix element into a Sudakov-like factor. (As before, if the trial emission is not accepted, the evolution continues starting from the scale of the failed trial, as required by the veto algorithm. Only after a branching has been accepted do we allow the evolution to be restarted from the full phase space of each dipole antenna.)

Expanded to tree level (all Sudakovs set equal to unity, fixed  $\alpha_s$ ), the trial generator will produce the following total weight for a specific color-ordered point in  $(n + 1)$ -parton phase space when summed over possible contributing  $n$ -parton ones,

$$w_{n+1}^{\text{trial}}(\{p\}_{n+1}) = \sum_j a_{\text{trial}-j}(\{\hat{p}_n\}^{[j]} \leftarrow \{p\}_{n+1}) |M_{n\text{LC}}^{(0)}(\{\hat{p}_n\}^{[j]})|^2, \quad (113)$$

where  $\{p\}_{n+1}$  represents the color-ordered momenta of the  $(n + 1)$ -parton state,  $j$  runs over the possible  $n + 1 \rightarrow n$  clusterings, and  $\{\hat{p}_n\}^{[j]}$  represents the color-ordered set of  $n$  momenta obtained by the  $j$ 'th  $3 \rightarrow 2$  clustering of the  $(n + 1)$ -parton state according to the selected kinematics map. It is important to note that  $|M_{n\text{LC}}^{(0)}|^2$  here represents the tree-level squared amplitude for the particular color configuration under consideration, i.e., without any color averaging performed.

The improved matching to smoothly ordered LL antenna functions described in sec. 4.2.2 merely consisted of multiplying  $a_{\text{trial}-j}$  in eq. (113) by the LL smooth-ordering accept probability, thus replacing the trial factors by their LL counterparts,

$$\text{LL Matching} : a_{\text{trial}-j} \rightarrow a_j^{\text{PS}} = P_{\text{accept}-j}^{\text{PS}} a_{\text{trial}-j}, \quad (114)$$



where  $P_{\text{accept-j}}^{\text{PS}}$  expresses the unmatched shower accept probability, including the LL acceptance probability,  $P^{\text{LL}}$ , of eq. (82) and the improvement factors  $P_{\text{imp}}$  of eq. (96) and  $P_{\text{Ari}}$  of eq. (97),

$$P_{\text{accept-j}}^{\text{PS}} = P_{\text{imp}} P_{\text{Ari}} P^{\text{LL}}. \quad (115)$$

We shall now apply a final multiplicative accept probability,  $P_{n+1}^{\text{ME}}$ , defined such that it takes us from the approximation that would have been generated by  $P_{\text{accept-j}}^{\text{PS}}$  alone to the full matrix element. It has the simple definition

$$P_{n+1}^{\text{ME}} = \frac{|M_{n+1}(\{p\}_{n+1})|^2}{\sum_k a_k^{\text{PS}}(\{\hat{p}\}_n^{[k]} \leftarrow \{p\}_{n+1}) |M_n(\{\hat{p}\}_n^{[k]})|^2}, \quad (116)$$

where  $a_k^{\text{PS}}$  was defined in eq. (114). By summing over all shower histories, this can easily be verified to generate the correct total weight. Note also that, the ME accept probability does not have any dependence on  $j$  and is thus the same for all contributing  $n \rightarrow (n+1)$  branchings.

Note that  $P_{n+1}^{\text{ME}}$  involves one evaluation of  $|M_{n+1}(\{p\}_{n+1})|^2$  and one evaluation of each of the reclustered configurations,  $|M_n(\{\hat{p}\}_n^{[k]})|^2$  (one for each possibility for  $[k]$ , of which one has already been evaluated as part of the current matched shower history), and hence the total number of matrix-element evaluations required at each order grows linearly with the multiplicity, rather than factorially as would have been the case for a non-Markov evolution.

Note also that, since we make no distinction between “shower events” and “correction events”, we may use the shower  $\alpha_s$  as a common prefactor on all the accept probabilities. There is thus only one  $\alpha_s$  for each history. Due to the scale-canceling partial one-loop matching discussed in sec. 4.2.2, the default, to one-loop accuracy, is thus to use  $\alpha_s(p_\perp)$  for all the terms, regardless of other scale choices made in the generator.

Another convenient way of writing  $P_{n+1}^{\text{ME}}$  is the following,

$$P_{n+1}^{\text{ME}} = 1 + \frac{|M_{n+1}(\{p\}_{n+1})|^2 - \sum_k a_k^{\text{PS}}(\{\hat{p}\}_n^{[k]} \rightarrow \{p\}_{n+1}) |M_n(\{\hat{p}\}_n^{[k]})|^2}{\sum_k a_k^{\text{PS}}(\{\hat{p}\}_n^{[k]} \rightarrow \{p\}_{n+1}) |M_n(\{\hat{p}\}_n^{[k]})|^2}, \quad (117)$$

where the connection to the subtraction approach described in ref. [33] (as well as to other subtraction schemes) becomes readily apparent, since the numerator in eq. (117) is nothing but a shower-subtracted matrix element.

In order to transform the unitary strategy described here to a non-unitary subtractive one, it would therefore suffice to apply the factor, eq. (117), as an event reweighting, rather than as a branch-accept probability. The events then do not have unit weights any more, and a subsequent unweighting step would be necessary, as in other subtractive approaches. The fact that we are here doing the matching phase-space point by phase-space point, however, means that we here have the ‘1+’ in front, which should mean that even the subtraction-based version could never generate negative weights. In current subtraction approaches such as MC@NLO, the ‘1+’ is generated as a separate sample, and in that case, the correction term by itself can of course yield negative correction events. The cancellation here is more elegant and not only yields positive-weight events but is also better protected from fluctuations; in MC@NLO and POWHEG, each event sample is uncorrelated and therefore the phase-space point of an event will never be hit exactly by the counter-events. In limited-statistics samples, it is

therefore events with slightly different momenta that have to compensate each other, whereas the proposal here achieves an exact cancellation in one and the same phase-space point, event by event. Thus, instead of having one event with weight +3 and one with weight -1, we would here simply get one event with a total weight of +2.

A final technical note is that the MADGRAPH matrix elements must be evaluated on-shell, and hence one must first set the value of the MADGRAPH  $Z$  mass equal to  $\sqrt{s}$ , even if this is not equal to the physical  $Z$  mass; the important thing is that the incoming momentum be on-shell. We also set the value of the strong coupling  $g_s = 1$  in MADGRAPH, equivalent to factoring it out of the problem.

### 5.3 Matching to Tree-Level Matrix Elements: Subleading Color

When summing over all events, the full answer contains an averaging over all permutations of color orderings in every phase-space point. In event generators, two different color structures in one and the same phase-space point are viewed as two different events with the *same* color structure, but in two different phase-space points. Via the matching above, this sum now reproduces the leading-color tree-level color-averaged matrix element squared. We wish to extend this to include the subleading-color contributions as well. Obviously, these cannot be associated with any particular color structure, and we must therefore here match across events in different phase-space points (or, equivalently, the same momentum configuration, but different color orderings).

When matching to subleading color, we shall use the specific structure of matrix elements generated with MADGRAPH and imported into the VINCIA code. The color structure of these matrix elements is cast as a color matrix whose diagonal entries form the leading-color contributions. Each diagonal entry corresponds to one particular color ordering, hence summing over all the diagonal terms and dividing by the number of rows (= number of permutations) is equivalent to averaging over colors, in the leading-color limit. The leading-color matching described above thus corresponds to matching to a MADGRAPH matrix element with only one diagonal term being non-zero in the entire color matrix, representing the particular color structure used in the matching.

In order to include subleading color, a simple and sufficient prescription is to compute also the full color-summed matrix element and include a fraction of it in the matching to each color structure, by modifying the LC matrix elements in eqs. (116) and (117) as follows,

$$|M_i|^2 \rightarrow |M_i|^2 + \frac{|M_i|^2}{\sum_j |M_j|^2} \sum_{j \neq k} M_j M_k^* \quad (118)$$

$$= |M_i|^2 \left( 1 + \frac{\sum_{j \neq k} M_j M_k^*}{\sum_j |M_j|^2} \right) \quad (119)$$

$$= |M_i|^2 \left( \frac{\sum_{j,k} M_j M_k^*}{\sum_j |M_j|^2} \right), \quad (120)$$

where  $M_i$  is the amplitude for one specific color ordering. The numerator in the last parenthesis is just the full color-summed matrix element squared, and the denominator is the corresponding leading-color one. Since both of these are well-defined leading-order physical matrix elements, the term in parenthesis is positive definite and hence cannot generate negative weights.

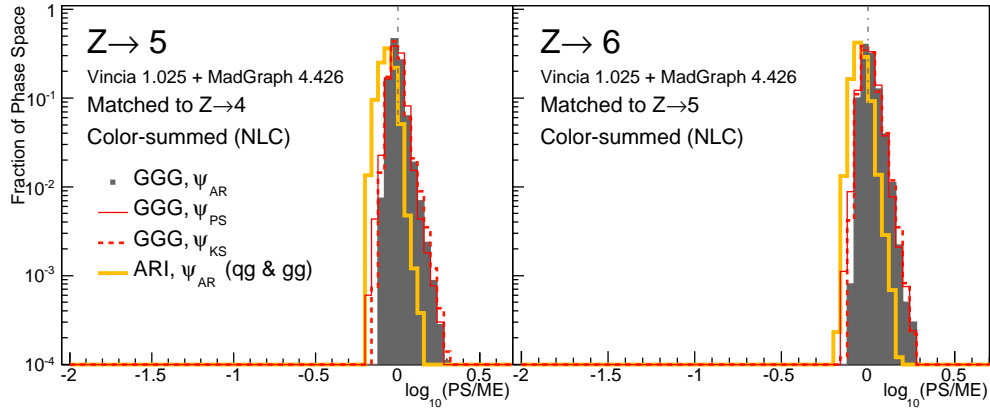


Figure 16: Smoothly ordered matched parton showers (unordered showers using the improvement factors  $P_{\text{imp}}$  and  $P_{\text{Ari}}$ ) compared to matrix elements. Distribution of  $\log_{10}(\text{PS}/\text{ME})$  in a flat phase-space scan. Contents normalized by the number of generated points. Gluon emission only. Matrix-element weights from MADGRAPH [52, 53], full color (summed over color permutations). Compare to the unmatched shower distributions in figs. 10, 14, and 15.

Note that, in VINCIA’s interface to MADGRAPH, we have so far been using the form in eq. (118), since this is the fastest in the context of that particular implementation. In order to compare between the leading- and full-color cases, we have implemented an option to switch the subleading corrections off, although they are on by default in the program.

In fig. 16, we show the weight ratios discussed earlier (which are essentially just the inverses of  $P_n^{\text{ME}}$ ), for  $Z \rightarrow 5$  and  $Z \rightarrow 6$  partons, now including matching at each preceding order. For the shower approximations, we use the default smoothly ordered NLC-improved GGG antennae, with three different kinematics maps (solid histogram, thin solid line, and dashed lines, respectively). We also compare to the same settings as the solid histogram but using the ARIADNE radiation functions instead of the GGG ones (thick solid lines). Comparing these distributions to those in fig. 14, we see that all the shower models reproduce the matrix elements very well, and hence the differences between the shower models are largely canceled by the matching to the preceding orders, as expected. At each order, now only a relatively well-controlled and stable matching correction remains, which does not appear to exhibit any significant deterioration order by order. Note that we have not applied *any* phase-space cuts here, and hence we find no evidence for any remaining subleading divergences in the matrix elements. This is in sharp contrast to slicing- or subtraction-based approaches, where a non-zero matching scale is obligatory beyond the first matched order.

#### 5.4 A note on MadGraph and GGG color factor normalizations

As a final remark, we note that the subleading-color terms are not uniquely defined. Obviously, if the leading-color pieces are not normalized the same way in two different approaches, the subleading terms must likewise appear different. This, e.g., leads to some apparent differences between MADGRAPH and the GGG antennae. With color and coupling factors, the

MADGRAPH-GGG correspondence for the  $Z \rightarrow qgg\bar{q}$  antenna is:

$$g_s^4 A_4^{\text{GGG}}(0, 1, 2, 3) = \frac{2|M_{4\text{LC}}(0, 1, 2, 3)|^2}{\hat{C}_F^2 |M_2(s)|^2}, \quad (121)$$

where the factor 2 on the MADGRAPH matrix element cancels the color averaging factor which is already present in  $|M_{4\text{LC}}|^2$ , which represents a MADGRAPH matrix element with only one element non-zero in the color matrix, the one corresponding to the  $(0, 1, 2, 3)$  color flow squared. In particular, note that the LC coefficient in MADGRAPH comes with  $\hat{C}_F^2$ , whereas, in order to construct the full answer, i.e., including subleading color, the GGG antennae should be combined in the following way,

$$\frac{|M_4|^2}{|M_2|^2} = g_s^4 \hat{C}_F C_A \left( \frac{1}{2} a_4(0, 1, 2, 3) + \frac{1}{2} a_4(0, 2, 1, 3) - \frac{1}{N_C^2} \tilde{A}_4(0, 1, 2, 3) \right). \quad (122)$$

A direct comparison between what would be called subleading color by GGG and by MADGRAPH, respectively, would thus yield a different answer, simply because the piece called LC is normalized to  $C_A \hat{C}_F$  in the former and to  $\hat{C}_F^2$  in the latter. To verify these normalizations, the validity of eqs. (121) and (122) was tested numerically on a large number of phase-space points.

## 6 Uncertainty Bands

A calculation is only as good as the trustworthiness of its uncertainty bands. Traditional methods for evaluating shower uncertainties range from simple comparisons between different models to more elaborate variations of salient model parameters within some theoretically or phenomenologically justified ranges.

The former kind is, at best, indicative, but can also be grossly misleading. As a classic example, consider two different parton showers with a cutoff at some factorization scale. They would both agree there are no jets above that scale, even though a matrix-element-based calculation would certainly produce jets in that phase-space region. Comparisons of the HERWIG – PYTHIA kind are therefore of little value when pursuing rigorous uncertainty estimates.

Systematic variation of salient model parameters obviously gives a more trustworthy idea of the overall uncertainty, and can also give information about which particular sources dominate. However, it requires more careful preparation and more expert input to set up: which parameters to vary, within what ranges, and how to make sure the variations are done consistently when combining many tools in a long chain of event generation. It also requires substantially more time and resources: for each variation, a new set of events must be generated, matched, unweighted, and possibly passed through detector simulation. Finally, the ability of a single model to span all possible variations is often limited — similarly to above, you still cannot use a strongly ordered shower to estimate what the uncertainty associated with the strong-ordering condition itself might be. There is also no way that, for instance, PYTHIA’s shower model could be varied to obtain an estimate of what an angular-ordered shower would give.

Here, we propose to combine the flexibility of the VINCIA formalism to take into account different ordering variables, radiation functions, etc., with a treatment of uncertainties that

only involves the generation of a *single* event sample, with a time requirement that is not greatly increased compared to the case without uncertainty variations. We shall also automate the expert input to some extent, reducing the number of choices the user must make.

The key question to ask is: if we use (matched) parton shower model A to generate a set of unweighted events, what would the weight of each of those events have been if we had instead used parton shower model B to generate them? By answering this question, we can essentially use any parton shower model as a “phase space primer”, provided it is still reasonably physical and that it does not have any dead zones, and then compute alternative weights *for the same events* for any other set of assumptions.

The most trivial part is to note that, if a particular shower model uses  $\alpha_{s1}a_1$  as its radiation function for a particular branching, the same branching would have happened with the relative probability

$$P_2 = \frac{\alpha_{s2}a_2}{\alpha_{s1}a_1} P_1 , \quad (123)$$

in a different model that uses  $\alpha_{s2}$  as its coupling (e.g., with a different renormalization scale or scheme) and  $a_2$  as its radiation function (e.g., with different finite terms, different partitioning of shared poles, different subleading or higher-order corrections, or even a different ordering criterion).

This, however, is not quite sufficient. Effectively, only the tree-level expansion of the shower would be affected by keeping track of such relative probabilities down along the shower chain; the Sudakov factors would remain unmodified. Such a procedure would therefore explicitly break the unitarity that is essential to resummation applications, leading to possibly exponentially different weights between the sets, which would be hard to interpret<sup>7</sup>. More intuitively, a big uncertainty on a very soft branching happening late in the shower should not be able to significantly change the entire event weight, jets and all. In the normal shower approach, it is the property of unitarity which keeps such things from happening; as soon as any correction grows large, its associated Sudakov factor must necessarily become small soon thereafter, keeping the total size of any correction inside a unit-probability integral.

The main part of our proposal therefore concerns a simple way to restore unitarity explicitly also for the uncertainty variations, as follows. For each accepted branching, a number of trial branchings have usually first been generated and discarded, to eliminate the overcounting done by the trial function. In VINCIA, we have so far not been particularly careful to optimize the choice of trial function (see sec. 3.2), and hence we have quite many failed trials. These are relatively cheap to generate, however, so the code is not significantly slowed by this inefficiency. Moreover, these failed trials actually turn out to be useful, even essential, in the present context.

Just as eq. (123) expresses the relative probability for a branching to be accepted under two different sets of model parameters, 1 and 2, with 1 playing the role of phase-space generator and 2 the role of uncertainty variation, it is also possible to ask what the probability of a *failed* trial to have failed under different circumstances would have been. Thus each failed trial can actually be used to compute variations on the no-emission probability, i.e., the Sudakov factors.

Specifically, for each trial, the no-emission probability for the model we use as our phase-space generator (which corresponds to the settings chosen by the user in VINCIA, including

---

<sup>7</sup>For example, two models that differ systematically by only a small amount on each branching, say 25%, would, after 20 such branchings, differ by a factor  $1.25^{20} = 100$ . If they differ by a factor of 2 instead, the result would be a million, clearly not a reasonable correction to the total event rate.

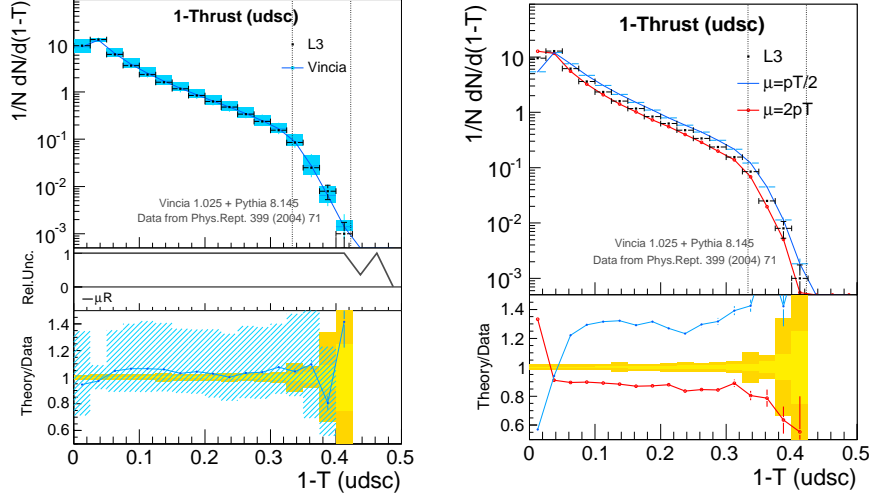


Figure 17: Comparison of *unmatched* results from VINCIA’s automatic uncertainty variations in the Thrust observable around the default parameter set (left) with those from running the generator for each variation separately (right), for variation of the renormalization scale. The L3 data taken from ref. [62] is shown for comparison. The yellow band in the lower plots represents the experimental uncertainties on the thrust measurement.

matching, subleading corrections, etc.) is

$$P_{1;\text{no}} = 1 - P_1 , \quad (124)$$

whereas the one for the alternative model should be

$$P_{2;\text{no}} = 1 - P_2 = 1 - \frac{\alpha_{s2} a_2}{\alpha_{s1} a_1} P_1 . \quad (125)$$

Thus, by multiplying the relative event weight  $w_2/w_1$  by  $P_2/P_1$  for each accepted branching and by  $P_{2;\text{no}}/P_{1;\text{no}}$  for each failed one, we explicitly restore the unitarity of the set of weights  $\{w_2\}$ . In order to prevent extreme outliers from substantially degrading the statistical precision of the variation samples, however, we limit the resulting weight adjustments to at most a factor of 2 *per branching* in the code (in either direction). The adjustment of the weights for the failed branchings takes the place of ‘unfailing’ those which should have succeeded with model 2.

The accuracy of the approach obviously depends on the abundance of failed branchings. If the trial function is completely exact, and no branching ever fails, then the tree-level problem above will still occur. However, since VINCIA typically generates significantly higher numbers of failed branchings than accepted ones, its effective numerical mapping of the changes in the Sudakov factors during the no-branching evolution periods should be reasonably accurate.

To test whether the uncertainty bands produced in this way really reproduce what the shower model would have generated with different settings, we show a few distributions in Figs. 17 and 18, with default VINCIA (thin blue line) plus an uncertainty variation (light blue band) on the left-hand side, and VINCIA run with the actual settings corresponding to that variation on the right, for variations of the renormalization scale (Fig. 17) and of the antenna function finite terms (Fig.18). In order to maximize the result of the variations, all

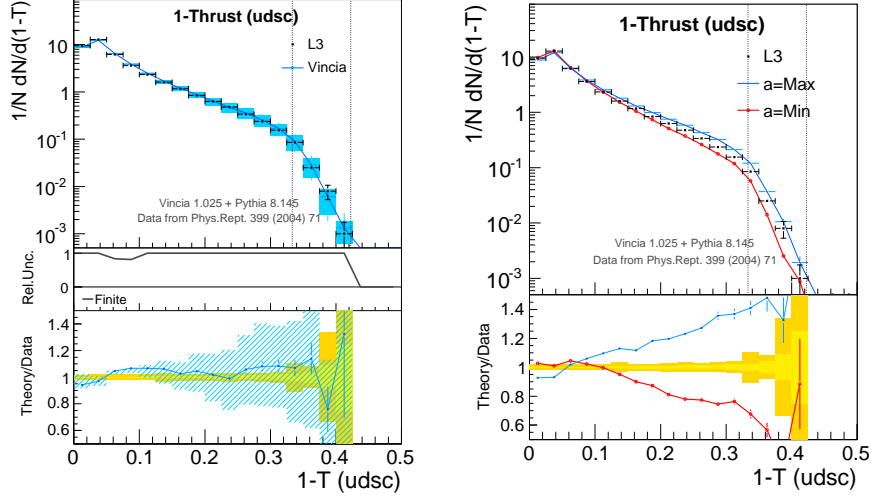


Figure 18: Comparison of *unmatched* results from VINCIA’s automatic uncertainty variations in the Thrust observable around the default parameter set (left) with those from running the generator for each variation separately (right), for variation of the antenna-function finite terms. The L3 data taken from ref. [62] is shown for comparison. The yellow band in the lower plots represents the experimental uncertainties on the thrust measurement.

matching is switched off, and hence the uncertainty bands are rather larger than would be the case for default VINCIA settings. The L3 data (black points) [62] are included mostly to provide a constant reference across the plots; we postpone the discussion of the data comparison to sec. 8, where we discuss LEP observables. The top panels of each the plots shows MC compared to data, with both normalized to unity. The bottom panels show the ratio MC/data, with the uncertainties on the data shown as yellow shaded bands, the inner (lighter) one corresponding to the statistical component only and the outer (darker) shade corresponding to statistical plus systematic errors (added linearly, to be conservative).

Comparing Figs. 17 and 18, one observes that the two different variations lead to qualitatively different shapes on the uncertainty predictions. The renormalization scale uncertainty, Fig. 17, produces an uncertainty band of relatively constant size over the whole range of Thrust, whereas the finite terms, Fig. 18, only contribute to the uncertainty for large values of  $1 - T$ , as expected. Comparing left to right in both figures, we conclude that both the features and the magnitude of the full uncertainty bands on the right are well reproduced by the weight variations on the left.

**Available Variations:** So far, five types of automatic variations have been included in the VINCIA code, starting from version 1.025, via a simple on/off switch. These uncertainty variations are:

- VINCIA’s default settings. This is obviously not a true uncertainty variation, but is provided as a useful comparison reference when the user has changed one or more parameters.
- MAX and MIN variations of the renormalization scale. The default variation is by a factor of 2 around  $p_{\perp}$ .



- MAX and MIN variations of the antenna function finite terms, as described in the online documentation of the code<sup>8</sup>.
- Two variations in the ordering variable, one being closer to strong ordering in  $p_\perp$  and the other to ordering in the  $m_D$  variable.
- MAX and MIN variations of the subleading color corrections. The specific nature of the variation depends on whether subleading corrections are switched on in the shower or not. If not, the MAX variation uses  $C_A$  for all gluon emission antennae and the MIN one  $\hat{C}_F$ . If switched on, the correction described in Section 4.3 is applied, but the correction itself is then modified by  $\pm 50\%$  for the MAX and MIN variations here.

These variations are provided as alternative weight sets for the generated events, which are available through methods described in the program’s online manual. Limited user control over the variations is also included, such as the ability to change the factor of variation of the renormalization scale.

When combining several variations to compute the total uncertainty, we advise to take just the largest bin-by-bin deviations (in either direction) as representing the uncertainty. We believe this is better than adding the individual terms together either linearly or quadratically, since the latter would have to be supplemented by a treatment of unknown correlations. With the maximal-deviation approach, we are free to add as many uncertainty variations as we like, without the number of variations by itself leading to an inflation of the error.

We should also note that, in the VINCIA code, matching coefficients etc. are calculated for each uncertainty variation separately. The size of each band is therefore properly reduced, as expected, when switching on corrections that impact that particular source of uncertainty.

Finally, we note that, though the speed of the calculation is typically not significantly affected by adding uncertainty variations, the code does run slightly faster without them. We therefore advise to keep them switched off whenever they are not going to be used.

## 7 Hadronization

Since the VINCIA code is a plug-in to PYTHIA, it is (almost) trivial to use PYTHIA’s string hadronization model with VINCIA, as long as one takes into account a few basic points:

- The matching of parton showers to hadronization models.
- The “tuning” of the resulting shower+hadronization framework.

Concerning the matching of parton showers to hadronization models, the main issue to keep in mind is that this matching is performed at a specific scale, the hadronization scale, which is implemented as a lower cutoff in the perturbative shower evolution, usually at a scale of order 1 GeV. Since no perturbative evolution is carried out below that scale, the job of the hadronization model is then to give as good a representation as possible of *all* the physics that takes place at lower scales. Since the hadronization model is inherently non-perturbative, this means that the cutoff cannot be taken too high, or else it would become apparent that the hadronization model does not include a good description of the perturbative parts. Vice versa, the cutoff cannot be taken too low, or else it would become apparent that the perturbative

---

<sup>8</sup>Available at <http://projects.hepforge.org/vincia/>.

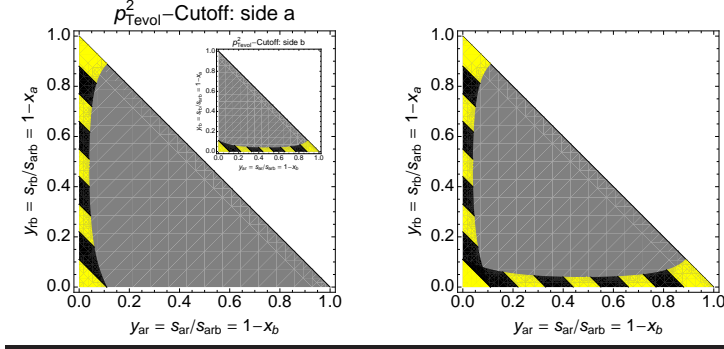


Figure 19: *Left*: the hadronization cutoff in  $p_{\perp\text{evol}}$  as it is imposed in PYTHIA, with the main plot showing one side of the evolving dipole and the inset the other. *Right*: in VINCIA, the whole dipole-antenna evolves as one entity, and therefore the cutoff must be placed likewise. The remaining difference only contains non-singular contributions from branchings in PYTHIA that accidentally throw the radiated parton close to the recoiling one.

modeling does not include a good description of the non-perturbative parts. This is how one ends up with scales of order 1 GeV as the matching point.

In principle, if the cutoff is varied around that point, both the perturbative shower and the non-perturbative modeling parameters should obey evolution equations that tell how each should scale, so that the end result would be approximatively independent of the cutoff. These evolution equations are nothing but an inclusive version of the shower evolution equations, which the shower obviously respects by definition.

But there is so far no formalism for the non-perturbative modeling that allows us to take parameters “tuned” with one value of the cutoff and translate them for use with another value for the cutoff. Hence each setting of the parameters of the hadronization model are only valid for the exact cutoff value that they were tuned with. If one uses a lower cutoff, then there would be double counting between the shower, which now extends to lower scales, and the hadronization model, whose tuning attempted to absorb those same corrections as well as possible. Conversely, if one used a higher cutoff, there would be a kind of “dead zone” unreachable by evolution, and where also the hadronization model tuning did not attempt to absorb the corrections.

To use PYTHIA’s hadronization model directly with VINCIA, we must therefore take the infrared cutoff to be at the same scale as the one used for the PYTHIA tuning, and since phase space is not one-dimensional, we also need to make sure it is in a variable which is as close to the one used by PYTHIA as possible. Contours corresponding to constant values of the PYTHIA 8 evolution variable were already illustrated in the discussion of evolution variables, fig. 8, and is reproduced in the left-hand pane of fig. 19 with an explicit cut showing the hadronization scale.

In the dipole-antenna framework, it is not possible to work with exactly the same variable; since we do not keep the two sides of the dipole-antenna,  $a$  and  $b$ , separate, it is not possible to use a different form for the cutoff for the two sides, which is effectively what is done in PYTHIA. The closest we can come is to apply the cutoff if the smallest of the two scales,  $p_{\perp\text{evol},a}$  and  $p_{\perp\text{evol},b}$ , is below the chosen cutoff scale, illustrated on the right pane of fig. 19.

This will veto some branchings in VINCIA that would have been allowed in PYTHIA, but since the PYTHIA radiation functions are not singular in those regions, and since the kinematics of the corresponding phase-space points are near-collinear, we do not expect this slight difference to have significant practical consequences.

In addition to the possibility of using VINCIA’s own variables,  $2p_{\perp}$  or  $m_D$ , as cutoffs, the option to use this emulation of the PYTHIA cutoff has therefore also been implemented in VINCIA and should allow, to a first approximation, to use the PYTHIA hadronization model with any of the VINCIA evolution settings, without retuning the non-perturbative parameters, as long as one accepts that the resulting answer will only be good up to perturbative uncertainties. That is, as long as the full VINCIA uncertainty is estimated, the data should still be compatible with the resulting uncertainty bands.

We note that, in order to obtain a *central* VINCIA tune, one would still have to perform a dedicated tuning of the PYTHIA 8 hadronization parameters using the particular VINCIA shower model for which the tuning is desired. This would also be necessary at the point when VINCIA’s formal level of precision is higher than that of PYTHIA, in which case using hadronization settings tuned with PYTHIA’s showers might actually result in incompatibility with the data, beyond the allowed perturbative uncertainty bands.

A first step towards getting a dedicated VINCIA tuning of the hadronization parameters was taken in April 2010 when one of the authors acted as host for a 1-week “industry internship” at CERN. Through the use of a specially developed runtime display for VINCIA, and given some basic explanations about the effect of the different hadronization parameters on the LEP distributions, M. Jeppsson, a Danish middle-school student, succeeded in making a tune of VINCIA to LEP data, including Thrust, the  $C$  and  $D$  parameters, jet rates, identified particle production rates, and the inclusive fractional momentum distribution,

$$x_{\text{particle}} = \frac{2E_{\text{particle}}}{\sqrt{s}} . \quad (126)$$

The final parameters he settled on appeared well motivated and physical, and now constitute the default in VINCIA. They are given in appendix B for reference. The runtime display, which is based on ROOT, has subsequently been made publicly available as part of the VINCIA package. To our knowledge, this study represents the first time “citizen science” has been used for event generator tuning.

## 8 Comparison to LEP Data

In the following, we have used version 1.025 of the VINCIA plug-in and version 8.145 of the PYTHIA 8 generator, using default settings unless otherwise specified. Note that for VINCIA, the default settings include a matching to tree-level matrix elements through third order in QCD (via its MADGRAPH interface), while PYTHIA only formally includes a first-order matching.

To keep questions of mass effects separate (the implementation of which will be reported on in a separate paper [56]), we shall here mainly compare to a useful data set presented by the L3 collaboration [62], in which the contributions from light flavors (defined as  $u, d, s, c$ ) has been separated from that of events containing  $b$  quarks.

Unfortunately, however, the L3 light-flavor data set does not contain jet observables. We therefore include comparisons also to ALEPH and DELPHI jet observables that include

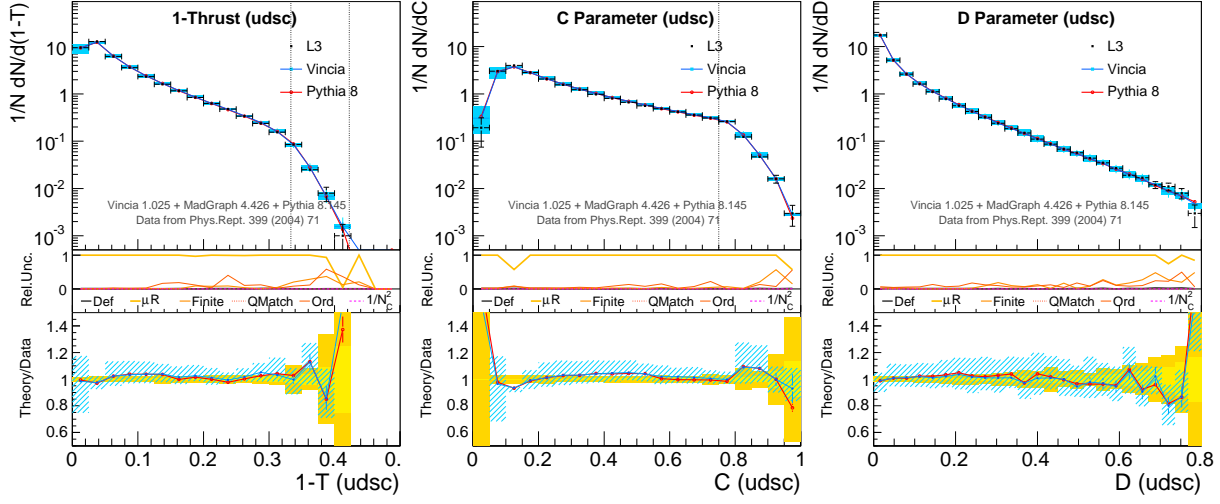


Figure 20: Comparison to the L3 light-flavor data set [62] (black points) at the  $Z$  pole for the  $1 - T$  (left),  $C$  (middle), and  $D$  (right) event shape variables. VINCIA is shown in thin blue lines, with shaded light-blue bands representing the perturbative uncertainty estimate. The middle pane on each plot illustrates the relative composition of the VINCIA uncertainty band. For comparison, the PYTHIA8 result is shown with a thick red line with open circles. The yellow bands in the bottom panels represent the experimental uncertainties on the measurement.

all flavors, using a preliminary implementation of mass effects in VINCIA [56]. Since the largest correction specific to  $b$  quarks is simply the  $B$  meson decay, for which we rely on PYTHIA’s string hadronization and hadron decay model, we believe these comparisons are still meaningful, even if we must postpone a full discussion of them to the follow-up study in ref. [56].

In Fig. 20, we compare default VINCIA and PYTHIA to the L3 light-flavor data for the Thrust (left) and the  $C$  (middle) and  $D$  (right) event shape parameters [62]. Dashed vertical lines indicate the boundaries between the 3- and 4-jet regions for the Thrust and  $C$  parameter (the right-most dashed line on the Thrust plot indicates the boundary with the 5-jet region). The  $D$  parameter measures the deviation from planar events and is a 4-jet observable over its entire range. Despite substantial differences in the shower modeling, matching level, and hadronization tune parameters, the two models give almost identical results. Further, since PYTHIA is already giving a very good description of this data, there is little for the additional matching in VINCIA to improve on here.

Still on Fig. 20, VINCIA’s uncertainty bands give about a  $\pm 10\%$  uncertainty over most of the observable ranges, with larger uncertainties near the edges of the distributions. The middle panels of the plots show the relative composition of the uncertainty estimates, and inform us that the renormalization scale variation is the dominant source of uncertainty for all the observables, with other sources only becoming competitive towards the right-hand extremes of the plots. This is an explicit consequence of the tree-level matching in VINCIA (by default imposed through third order), which significantly reduces the allowed range of finite-term, ordering-variable, and subleading-color uncertainty. The renormalization-scale

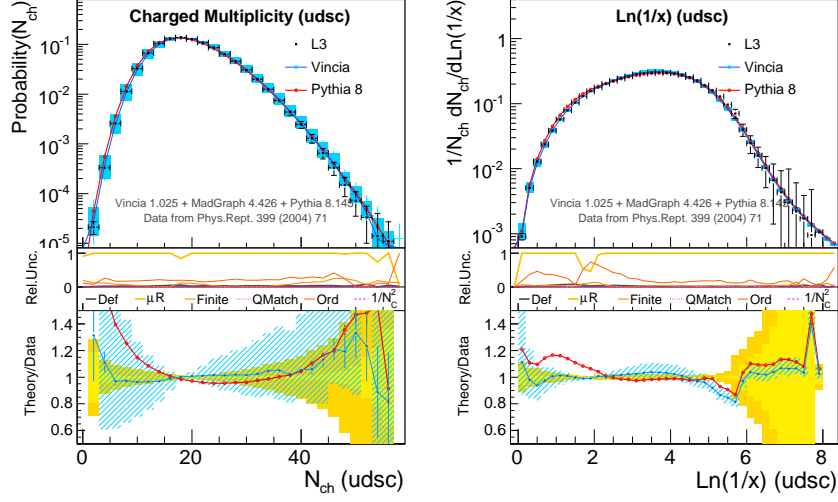


Figure 21: Comparison to the L3 light-flavor data set [62] (black points) at the  $Z$  pole for the charged track multiplicity (left) and fractional momentum (right) spectra. VINCIA is shown in thin blue lines, with shaded light-blue bands representing the perturbative uncertainty estimate. The middle pane on each plot illustrates the relative composition of the VINCIA uncertainty band. For comparison, the PYTHIA8 result is shown with a thick red line with open circles. The yellow bands in the bottom panels represent the experimental uncertainties on the measurement.

uncertainty, however, is unaffected by tree-level matching. Although the scale-dependence-reducing correction described in Section 4.1 is acting to reduce this dependence, the residual uncertainty from scale variation is still larger than that from any of the other sources.

In Fig. 21, we compare to two infrared-sensitive observables also measured by L3 with light-flavor tagging, the charged track multiplicity (left) and the fractional momentum distribution (right), with the latter given by eq. (126). (Note that ref. [62] uses the notation  $\xi = -\ln x$ .) We conclude that PYTHIA 8 was probably tuned on slightly different observables, and hence the agreement obtained with VINCIA is here improved both by giving a slightly narrower multiplicity distribution, with fewer low-multiplicity events and a slightly softer fragmentation spectrum, with fewer particles carrying  $x$  fractions very close to unity. One also notes that VINCIA’s estimated uncertainty on the individual bins of the charged-track multiplicity distribution is much larger than the estimated uncertainty on the fragmentation spectrum. Recall, however, that VINCIA is only able to vary the perturbative parameters — variations of the string fragmentation parameters would have to be included here to gain a better understanding of the full uncertainties. All we can say at this level is that the charged-multiplicity distribution appears to suffer from a larger perturbative uncertainty than the fragmentation spectrum.

A further set of variables that is interesting in the context of differential multi-jet production are the so-called four-jet angles, which were also measured at LEP. Not having found a public data repository containing this particular data, however, we instead resorted to extracting the data point values from the HERWIG++ source code [40], where it is encoded for validation and tuning purposes. A comparison between this data and default VINCIA and

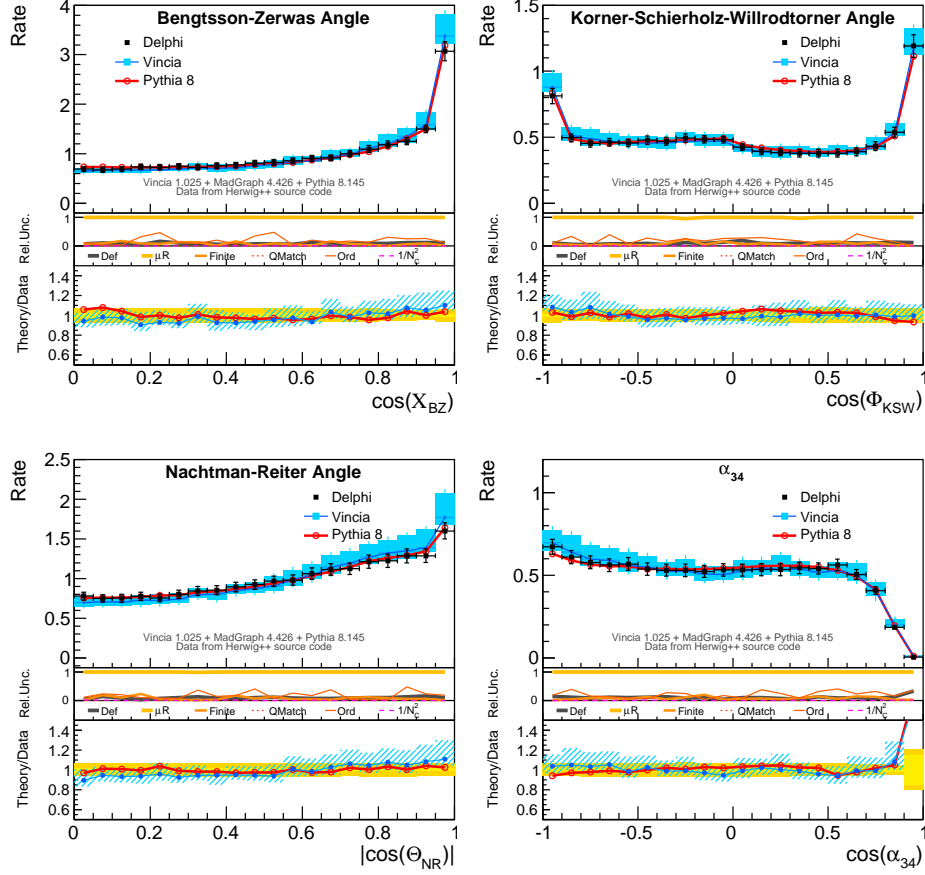


Figure 22: Comparison to DELPHI 4-jet angle measurements (black points) at the  $Z$  pole. VINCIA is shown in thin blue lines, with shaded light-blue bands representing the perturbative uncertainty estimate. The middle pane on each plot illustrates the relative composition of the VINCIA uncertainty band. For comparison, the PYTHIA8 result is shown with a thick red line with open circles. The yellow bands in the bottom panels represent the experimental uncertainties on the measurement.

PYTHIA is shown in Fig. 22. Again, it is clear that PYTHIA itself is already doing a very good job. Since PYTHIA is not matched to 4-jet matrix elements and also does not contain explicit spin correlations in the shower, this may at first be surprising. However, PYTHIA does correlate the production and decay planes of gluons in the shower, and thereby includes the leading effect of gluon polarization. The VINCIA shower, on the other hand, contains no polarization effects a priori. In VINCIA's case, the effective correlations of the four-jet angles are instead coming from matching to the 4-parton matrix elements, and both codes are able to describe the 4-jet angles within a roughly 5% margin, which is comparable to the experimental precision.

Finally, in Fig. 23, we compare to the jet resolutions measured by the ALEPH experiment [63]. Firstly, note that pure PYTHIA is basically able to describe all the distributions, within the experimental accuracy, despite its being matched only to  $Z \rightarrow 3$  partons. On the one hand, this is good, since it implies that the PYTHIA 8 shower is delivering a quite good



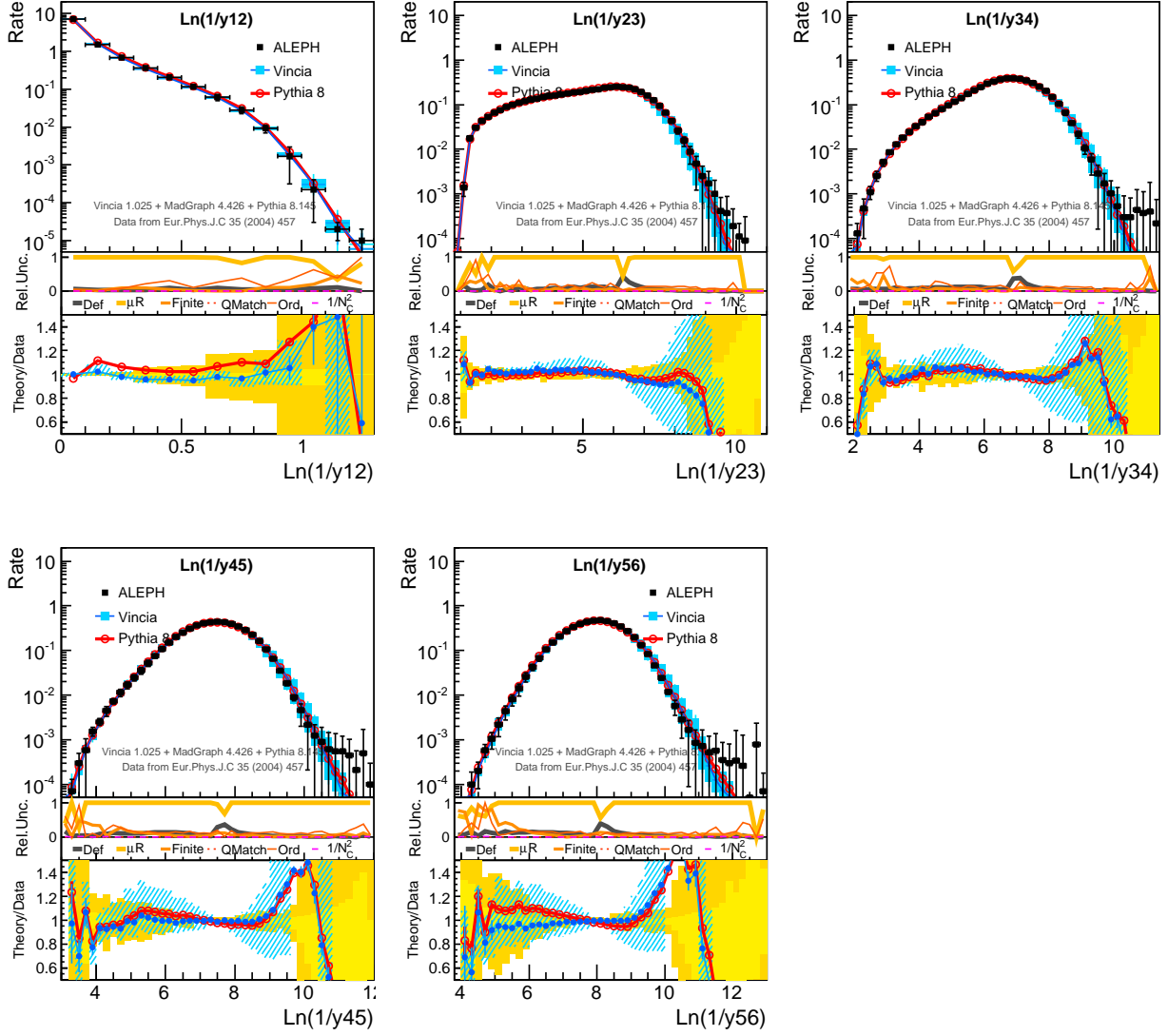


Figure 23: Comparison to ALEPH jet resolution measurements [63] (black points) at the  $Z$  pole. VINCIA is shown in thin blue lines, with shaded light-blue bands representing the perturbative uncertainty estimate. The middle pane on each plot illustrates the relative composition of the VINCIA uncertainty band. For comparison, the PYTHIA8 result is shown with a thick red line with open circles. The yellow bands in the bottom panels represent the experimental uncertainties on the measurement.



approximation to QCD also beyond the matched orders. On the other hand, it also means that we are not really able to quantify any significant improvement by matching using this data alone. This may partly be due to the data having quite large uncertainties for hard multi-jet configurations; at least  $\pm 20\%$  for jet resolutions  $\ln(y_{45}) > -4$ , which corresponds to  $p_\perp$  scales of order 10 GeV. Thus, this data does not really have enough power to make precision tests in the hard multi-jet region. This relatively low discriminating power of the hard multi-jet data will likely be an even greater problem for testing any future one-loop matched schemes.

We see four possible avenues to improve on this situation, requiring various levels of additional experimental effort. One, combine the hard multi-jet data from the four LEP experiments to increase the overall discriminating power. Two, re-process the data focussing on observables more specifically tailored to project out regions not dominated by leading logs, e.g., by measuring  $y_{nn+1}$  while imposing specific constraints on the resolutions of the other  $(n-1)$  harder jets in the event. Three, increased statistics from a future facility such as GigaZ. Four, measurements of hard jet rates and resolutions outside the  $e^+e^-$  environment, i.e., at hadron colliders, again possibly placing more exclusive restrictions on the multi-jet structure of the events. Especially the latter looks promising now in the dawn of the LHC era, but of course comes at the price of introducing additional uncertainties due to the colored initial states. LEP is therefore likely to retain its position as our main jet fragmentation laboratory for the foreseeable future, and with the official closing of the LEP experiments this year, we wish to encourage those in a position to do so to keep the LEP data ‘alive and well’ for future analysis studies that are likely to involve tests of models far more sophisticated than those that were available ten or twenty years ago. This makes it necessary to look at data much more differentially and/or exclusively than is possible with, e.g., with the observables that were included in our comparisons here.

## 9 Conclusions

We have taken the next step in developing the formalism, started in ref. [33], for generic parton showers based on the dipole-antenna formalism. Evolution equations for a wide class of evolution variables, kinematics maps, and radiation functions, have been presented, including all the necessary steps to construct an explicit stochastic Markov-chain Monte Carlo code.

The basic ideas behind this shower model are similar to those behind the existing ARIADNE program [17], to whose properties we make some comparisons. Aside from the more generic formalism, we also propose some systematic improvements, including suppressed unordered branchings to cover the hard region of phase space and systematic “next-to-leading-color” (NLC) corrections. We compare explicitly to matrix elements at both leading and subleading color for  $Z \rightarrow 4, 5$ , and 6 partons, to check the validity of our approximations.

We have also presented a new method for matching parton showers to tree-level matrix elements at the multi-jet level, formulated in a language appropriate to our shower framework. At lowest order, it is similar to an older scheme by Sjöstrand and collaborators [28, 29], which has recently been reformulated in a more generic NLO context called POWHEG [30]. Though our scheme is therefore similar to, and compatible with, these existing methods, we here extend the method to tree-level matching involving more than one emission. As such, the method is at the same formal level of precision as the MENLOPS approach [26], but with the difference that the multi-parton matrix element corrections are here exponentiated, which

should both improve the logarithmic accuracy of our Sudakov factors at the same time as making the approach much less sensitive to so-called matching scales (scales below which the matrix-element corrections are switched off). We do still advocate imposing *some* matching scale at high multiplicities, mostly to avoid spending lots of time computing matrix elements for very soft emissions that the unmatched shower is describing correctly anyway. For the results reported on in this paper, a matching scale of 5 GeV (above the hadronization scale but well below typical jet  $p_T$ s) was therefore imposed starting from third order in QCD (corresponding to  $Z \rightarrow 5$  partons).

By default, the generated events form one continuous sample with no specific separation between jet multiplicities and with all events having unit weight.

The matched shower algorithm is implemented in the VINCIA plug-in to the PYTHIA 8 Monte Carlo generator. Apart from its dependence on PYTHIA 8, the plug-in is self-contained with its own documentation and user-definable parameters. It also includes facilities for linking to the FASTJET [64] and ROOT packages. In the latter case, a run-time interface has been developed that allows to display ROOT histograms in real time during the generator run, which can be useful both to give an immediate sanity check that histograms are being filled correctly, and also to visualize the gradual improvement in MC statistics over the run. The generated events have similar physical properties as those generated by standard PYTHIA 8 and can be passed through the latter’s string model for hadronization, and, e.g., to HEPMC [65] for further processing, e.g., by analysis tools like RIVET [66] or detector simulation packages.

Finally, we have presented a new efficient and automatable method for the evaluation of uncertainty bands by parton shower generators. The method draws on the unitarity property of shower calculations to compute several sets of weights for a single generated event sample. This sample can then be subjected to cuts, hadronized, passed through detector simulations, etc., and the uncertainty variations can be obtained by filling histograms with each of the different weight sets separately at any stage during the processing. We have implemented this method in VINCIA, to provide an option for automatic evaluation of renormalization-scale, finite-term, ordering, and subleading-color uncertainties.

## Acknowledgments

We thank L. Dixon, A. Gehrmann-de-Ridder, L. Lönnblad, and M. Ritzmann, for many useful comments on the manuscript. We also gratefully acknowledge the contributions of M. Jeppsson to the optimization of PYTHIA’s hadronization parameters for use with VINCIA, by performing a first hadron-level tune to LEP data. We thank the HERWIG++ collaboration for help with extracting the DELPHI 4-jet angle data from their source code. This work was supported in part by the Marie Curie FP6 research training network “MCnet” (contract number MRTN-CT-2006-035606), by the U.S. Department of Energy under contract No. DE-AC02-07CH11359, and by the European Research Council under Advanced Investigator Grant ERC-AdG-228301.

## A Comparisons to 2nd Order QCD Matrix Elements

In the following, we present a series of figures comparing dipole-antenna showers — ordered in various different evolution variables — to matrix elements, on the  $R_4$  ratio defined in eq. (83). As in sec. 3, these plots were made on 20M random points in a flat phase-space scan, using RAMBO [51]. We use the default VINCIA antenna functions and kinematics maps in all cases and only vary the evolution variable.

On each plot, the quantity on the  $x$  axis is a scale characterizing the first emission ( $2 \rightarrow 3$ ), while the quantity on the  $y$  axis is a scale characterizing the second ( $3 \rightarrow 4$ ). Further, the quantity on the  $y$  axis has been normalized to the one on the  $x$  axis, so that it really represents the ordering of the second emission, relative to the first. Thus, phase-space points with hard initial  $2 \rightarrow 3$  branchings will lie to the right in the figures, while soft (strongly ordered) initial emissions lie to the left. On the  $y$  axis, points where the second scale is much smaller than the first (i.e., strongly ordered relative to the first) will be towards the bottom of the plot, while unordered points will be towards the top of the plot.

To help the eye, we have added a horizontal red line at  $\ln(y) = 0$  on the plots, dividing the phase space for the 2nd emission into an ordered part (below the line) and an unordered one. Similarly, the emphasized black box highlights the region where  $x$  is more than an order of magnitude below  $M_Z$ , and  $y$  more than an order of magnitude below  $x$ , i.e., the doubly-ordered region. Finally, the dotted lines show contours of constant  $\ln(y/M_Z^2)$ , or equivalently constant  $y$ .

For each evolution variable, we show 4 plots, all with logarithmic  $x$  and  $y$  scales:

- *Top Left:* Average PS/ME ratio  $\langle R_4 \rangle$  vs. the  $p_\perp$  scales of the two emissions. On the  $y$  axis, the smallest of the two possible  $p_\perp$  scales in the 4-parton configuration. On the  $x$  axis, the  $p_\perp$  scale of the corresponding 3-parton configuration.
- *Top Right:* The RMS width of the left-hand ratio, counting dead zones as having a factor 10 difference (otherwise the log of the ratio would be undefined). This helps illustrate whether a good average agreement on the left-hand side is just an accident of a wide distribution centered around unity, or whether the distribution itself is really narrow.
- *Bottom Left:* Same as top left, but with the  $y$  axis showing the invariant mass of the two gluons. This projection is interesting since it allows us to isolate a particular double-collinear limit, as follows. If  $m_{gg}^2 \sim m_Z^2$ , then the two gluons are well separated and carry all the energy of the original partons. This energy can only have been transferred to them by two successive extreme collinear branchings, one where the quark gives all its energy to the first gluon, and a second where the antiquark gives all its energy to the other gluon. To check if we get this non-trivial limit right, the upper edge of this distribution is therefore especially interesting.
- *Bottom Right:* Same as top left, but with the ordering measure being invariant mass instead of  $p_\perp$ . This distribution is complementary to the top left one, showing the same ratio in a slightly different projection, versus a measure of invariant masses, again in order to check whether any agreement observed in the above variables persists when doing a different cut through phase space.

Note that, since we use the default VINCIA antenna functions, which reproduce the  $Z \rightarrow 3$  matrix elements, we expect a good agreement even when the first emission is not strongly ordered. It is therefore mainly the ordering of the second emission with respect to the first that is interesting.

## B Jeppsson Tune Parameters

The following table gives an overview of the parameters used for VINCIA and PYTHIA for the results obtained in this paper. The default settings in PYTHIA 8.145 were obtained by a fit to a large amount of LEP data, using the RIVET+PROFESSOR framework [66,67]. The VINCIA 1.025 parameters were tuned manually, as reported on in sec. 7. The latter included the total charged particle multiplicity and  $\xi = -\log(x)$  distributions, mean multiplicities of light mesons and baryons, event shapes ( $1 - T$ , Major, Minor,  $C$ ,  $D$ , Oblateness), and jet resolution scales ( $y_{23}$ ,  $y_{34}$ ,  $y_{45}$ ,  $y_{56}$ ) extracted from the measurements contained in the HEPDATA [68] repository.

Parameter	PYTHIA 8.145 Default	VINCIA 1.025
Shower Parameters		
Evolution Variable	$p_{\perp \text{evol}}$	$p_{\perp}$
Renormalization Scale	$p_{\perp \text{evol}}$	$p_{\perp}$
$\alpha_s(M_Z)$	0.1383	0.139
$\alpha_s$ loop order	1	1
Shower Cutoff Variable	$p_{\perp \text{evol}}$	$2p_{\perp}$
Shower Cutoff Scale in GeV	0.5	1.0
String Breakup Parameters		
StringZ:aLund	0.30	0.28
StringZ:bLund	0.80	0.55
StringPT:sigma	0.304	0.275
StringPT:enhancedFraction	0.01	0.01
StringPT:enhancedWidth	2.0	2.0
Flavor Parameters		
StringFlav:probStoUD	0.19	0.21
StringFlav:mesonUDvector	0.62	0.40
StringFlav:mesonSvector	0.725	0.6
StringFlav:probQQtoQ	0.09	0.079
StringFlav:probSQtoQQ	1.0	1.0
StringFlav:probQQ1toQQ0	0.027	0.035
StringFlav:decupletSup	1.0	1.0
StringFlav:etaSup	0.63	0.60
StringFlav:etaPrimeSup	0.12	0.075

## Phase-Space Ordering

$$Q_E^2 = \max(s_{ij}, s_{jk})$$

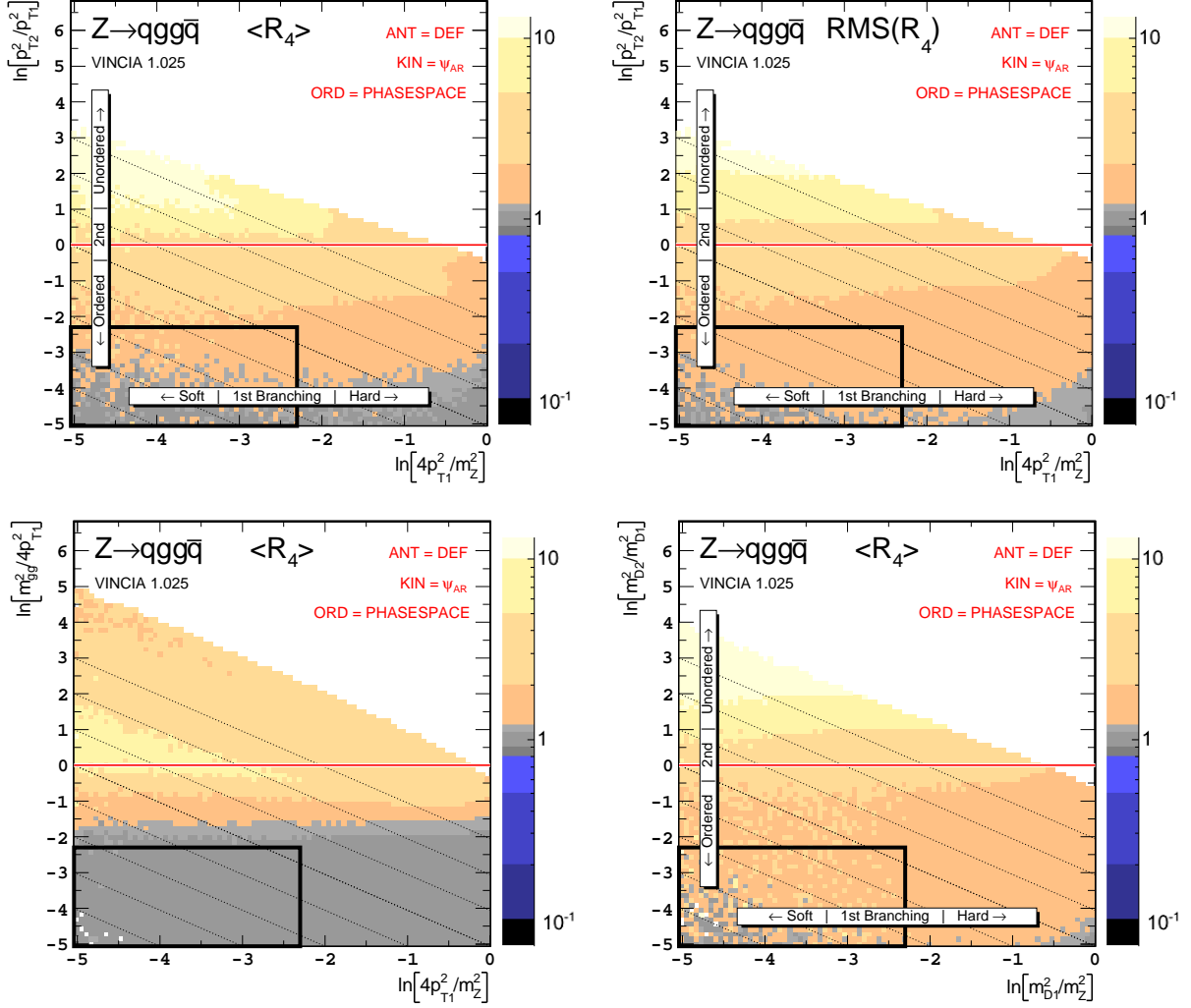


Figure 24: Phase-space-ordered antenna approximation compared to 2nd order QCD matrix elements. Note: this roughly corresponds to a mass-ordered parton shower without coherence. Although the double-soft limit is eventually reached, there is a large overcounting over most of phase space, reflecting a lack of coherence. Also, the double counting extends into the double-collinear region at the top of the lower left-hand plot. This ordering, therefore, does not lead to the correct multiple-collinear singular limit.

# Transverse-Momentum Ordering (ARIADNE)

$$p_{\perp}^2 = \frac{s_{ij}s_{jk}}{s}$$

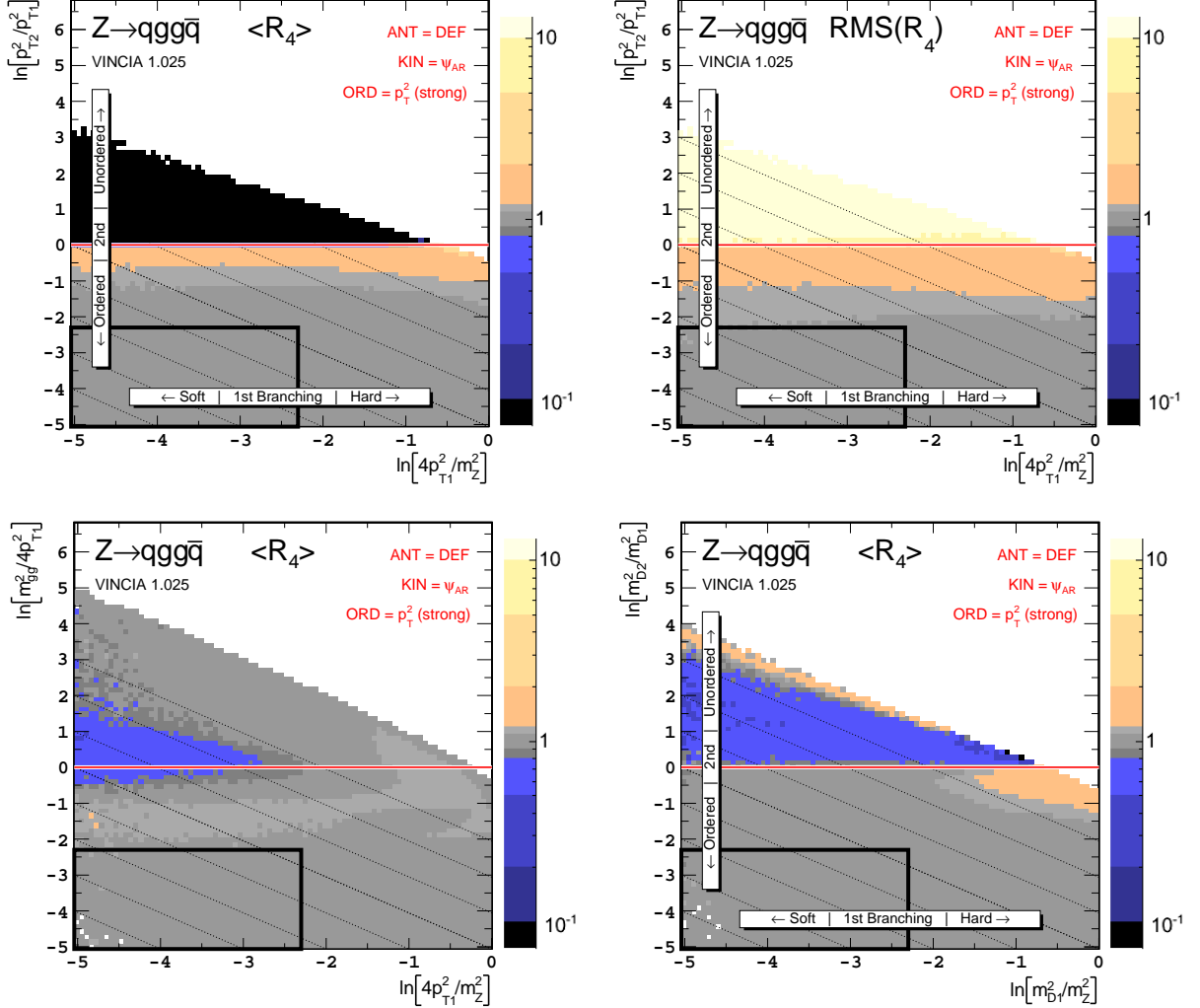


Figure 25: Transverse-Momentum-Ordered antenna approximation compared to 2nd order QCD matrix elements, using the ARIADNE definition of  $p_{\perp}$ , which is also the default evolution variable in VINICIA. Most of the double-counting evident for phase-space ordering has been removed, and the shower approximation now also gives the correct answer in the double-collinear region at the top of the lower left-hand plot. The price is the introduction of a dead zone, visible at the top of the upper left-hand plot. The size of the dead zone in the flat phase-space scan amounts to about 2% of all sampled points.

## Transverse-Momentum Ordering (PYTHIA)

$$4p_{\perp\text{evol},I}^2 = 4 \frac{s_{ij}(s - s_{jk})(s_{ij} + s_{jk})}{(s + s_{ij})^2}$$

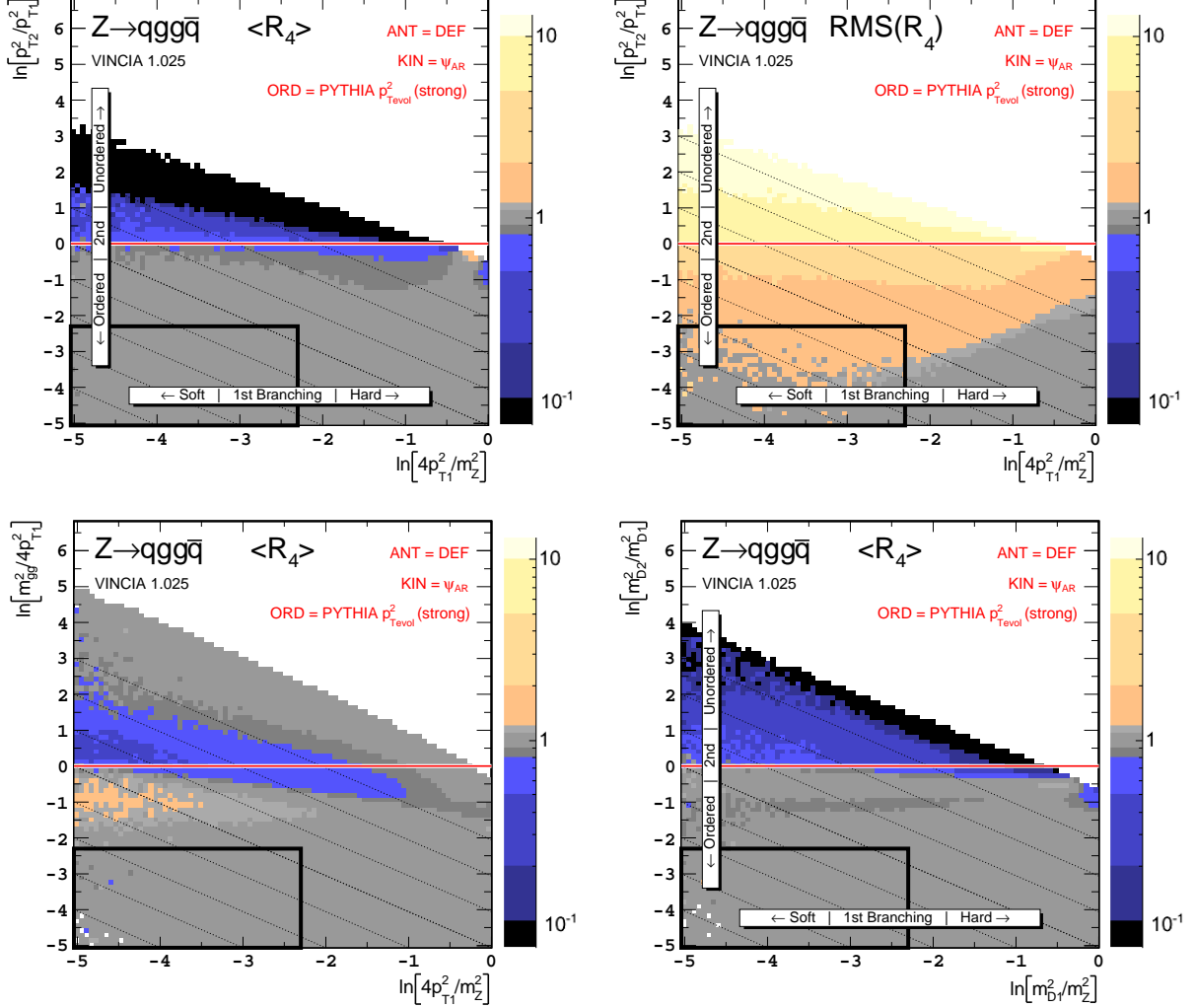


Figure 26: Transverse-Momentum-Ordered antenna approximation compared to 2nd order QCD matrix elements, using PYTHIA’s definition of Transverse Momentum,  $p_{\perp\text{evol}}$ . Note: the antenna functions and kinematics maps are still the default VINCIA ones, hence these results do not directly correspond to what would be obtained with the PYTHIA program. The PYTHIA  $p_{\perp}$ -definition is a bit more restrictive and increases the size of the dead zone to 5% of the sampled points. This in turn leads to a lower average ratio in some regions. The fact that the RMS distribution indicates a large spread of weights even on the edges of the strongly-ordered region (black box) reflects the migration of a few dead-zone points to this region, due to the mismatch between the ordering variable and the  $p_{\perp}$  definition on the axes.



## Mass-Ordering (VINCIA)

$$m_D^2 = 2\min(s_{ij}, s_{jk})$$

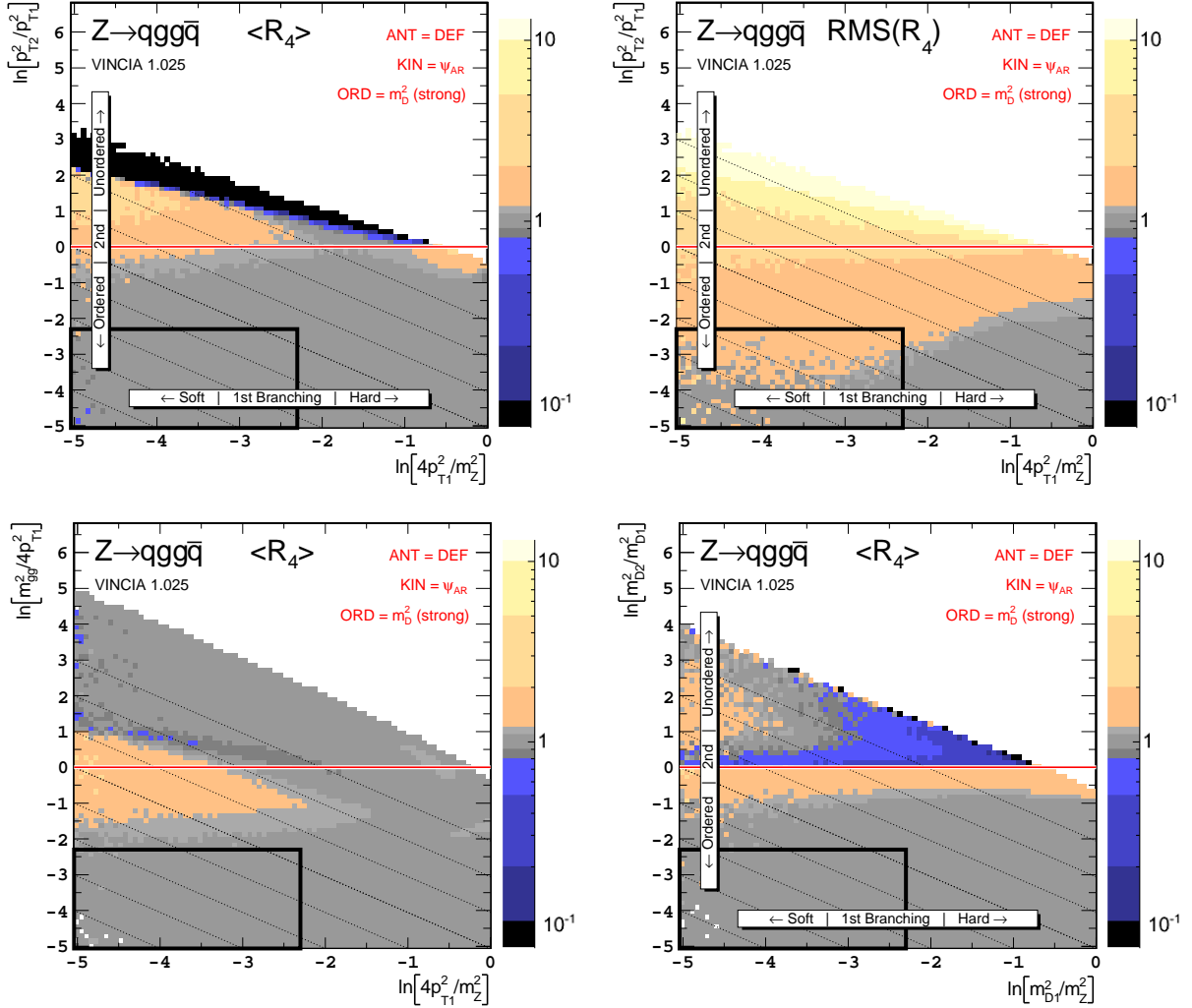


Figure 27: Mass-Ordered antenna approximation compared to 2nd order QCD matrix elements, using VINCIA's definition of Daughter Dipole Mass,  $m_D$ . This ordering is a bit less restrictive than  $p_\perp$ , hence the size of the dead zone shrinks to about 1% of the sampled points. The tradeoff is that some overcounting remains over some parts of phase space. As for the PYTHIA  $p_\perp$ -ordering, the RMS distribution indicates a quite wide distribution extending inside the doubly-ordered box, which we interpret as being due to the mapping of some dead-zone points to this region.

## Energy-Ordering (DM)

$$4E_j^{*2} = \frac{(s_{ij} + s_{jk})^2}{s}$$

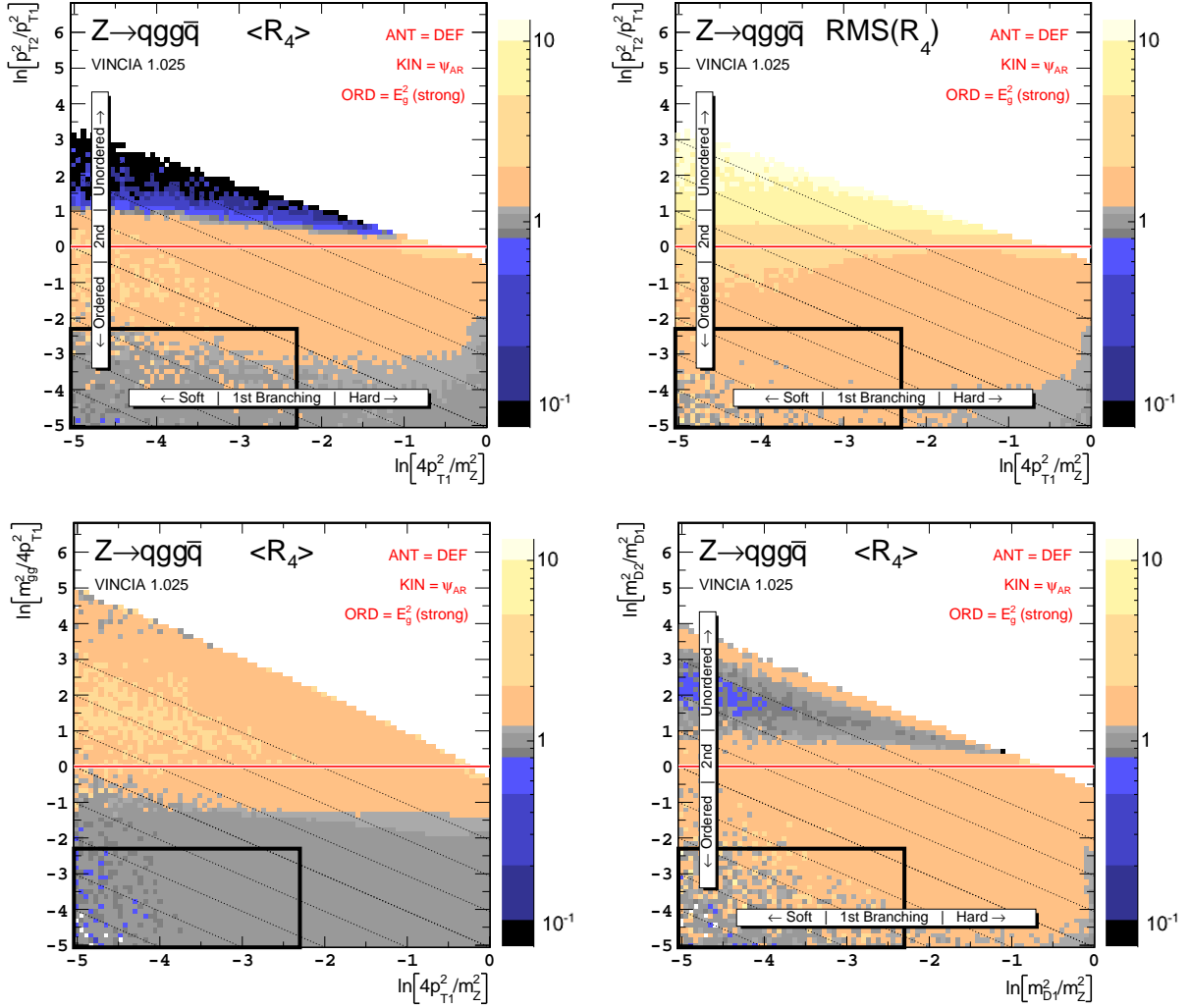


Figure 28: Energy-Ordered antenna approximation compared to 2nd order QCD matrix elements, using a definition of energy a la Dokshitzer-Marchesini (DM). Although a small dead zone in the unordered region still exists (0.6% of the sampled points), there remains a very large overcounting over significant parts of phase space, including the double-collinear region mentioned before, at the top of the lower left-hand plot. We conclude that this variable does not lead to the correct multiple-collinear singular limit.

## Modified Energy-Ordering (VINCIA)

$$E_{T1}^{*2} = \frac{\sqrt{8s_{ij}s_{jk}(s_{ij}^2 + s_{jk}^2)}}{s}$$

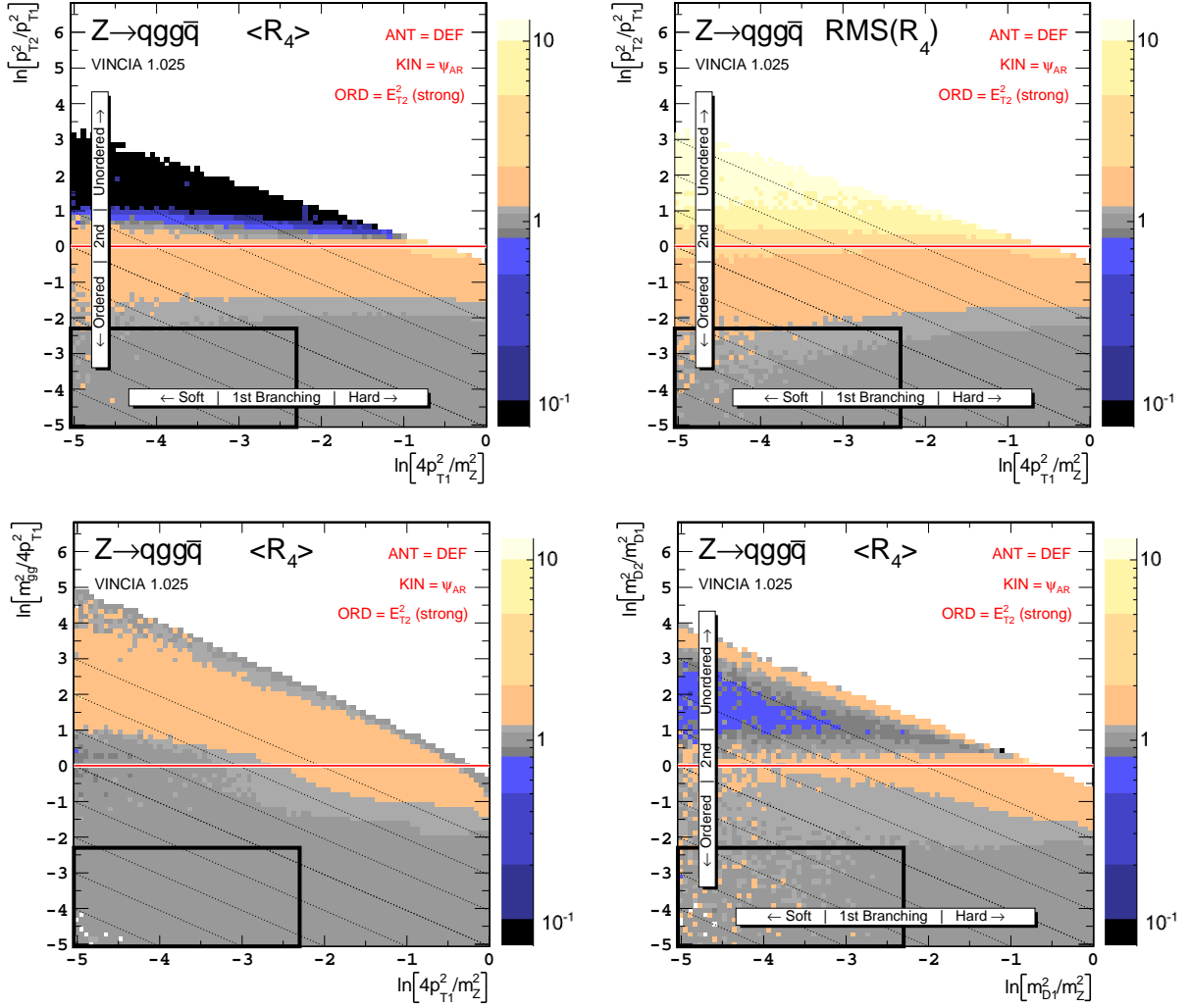


Figure 29: Energy-Ordered antenna approximation compared to 2nd order QCD matrix elements, using a modified definition of energy that makes it explicitly sensitive to collinear emissions. The dead zone is still quite small, ca. 0.7% of the sampled points, but the approximation is improved with respect to energy ordering over most of phase space, including the double-collinear region at the top of the lower left-hand plot.

## Angular-Ordering (HERWIG++)

$$q_{\theta,I}^2 = 4s \left( \frac{ss_{ij}}{(s - s_{jk})(s_{ij} + s_{jk})} \right)^2 = 4s \left( \frac{1 - x_k}{x_i x_j} \right)^2$$

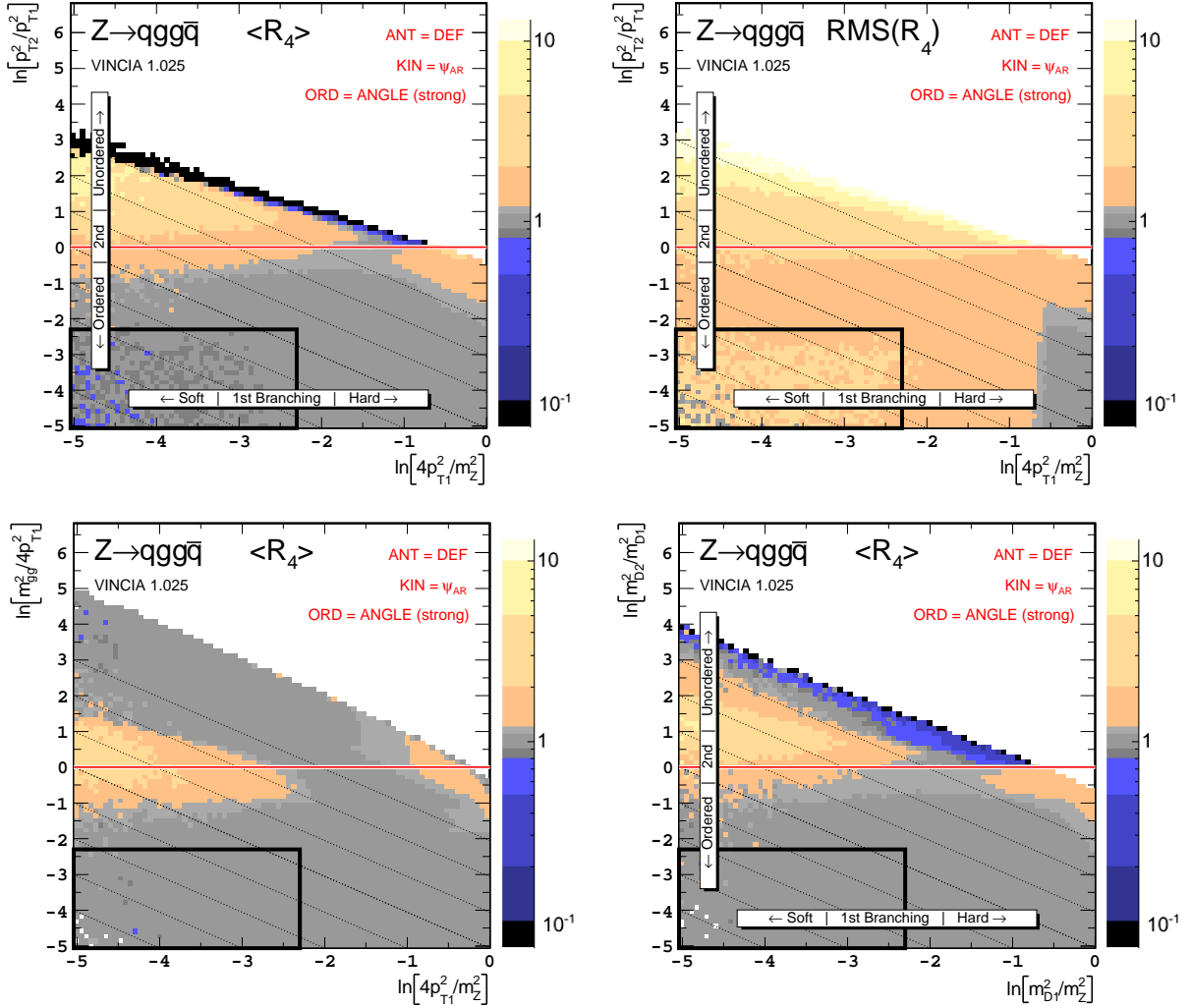


Figure 30: Angular-Ordered antenna approximation compared to 2nd order QCD matrix elements, using the HERWIG++ definition of angles. Note: the antenna functions and kinematics maps are still the default VINCIA ones, hence these results do not directly correspond to what would be obtained with the HERWIG++ program. The dead zone in this variable amounts to 1% of the sampled points. Although the double-collinear region appears to be well approximated (see top of lower left-hand plot), there appears to be a tendency toward undercounting of the double-soft region (box in top left plot). The RMS spread is also very large over substantial regions of phase space (top right plot), extending well beyond the region affected by the dead zone.

## V-Ordering (VINCIA)

$$V^2 = s \left( \sqrt{\frac{s_{ij} + s_{jk}}{s}} - \sqrt{\frac{|s_{ij} - s_{jk}|}{s}} \right)$$

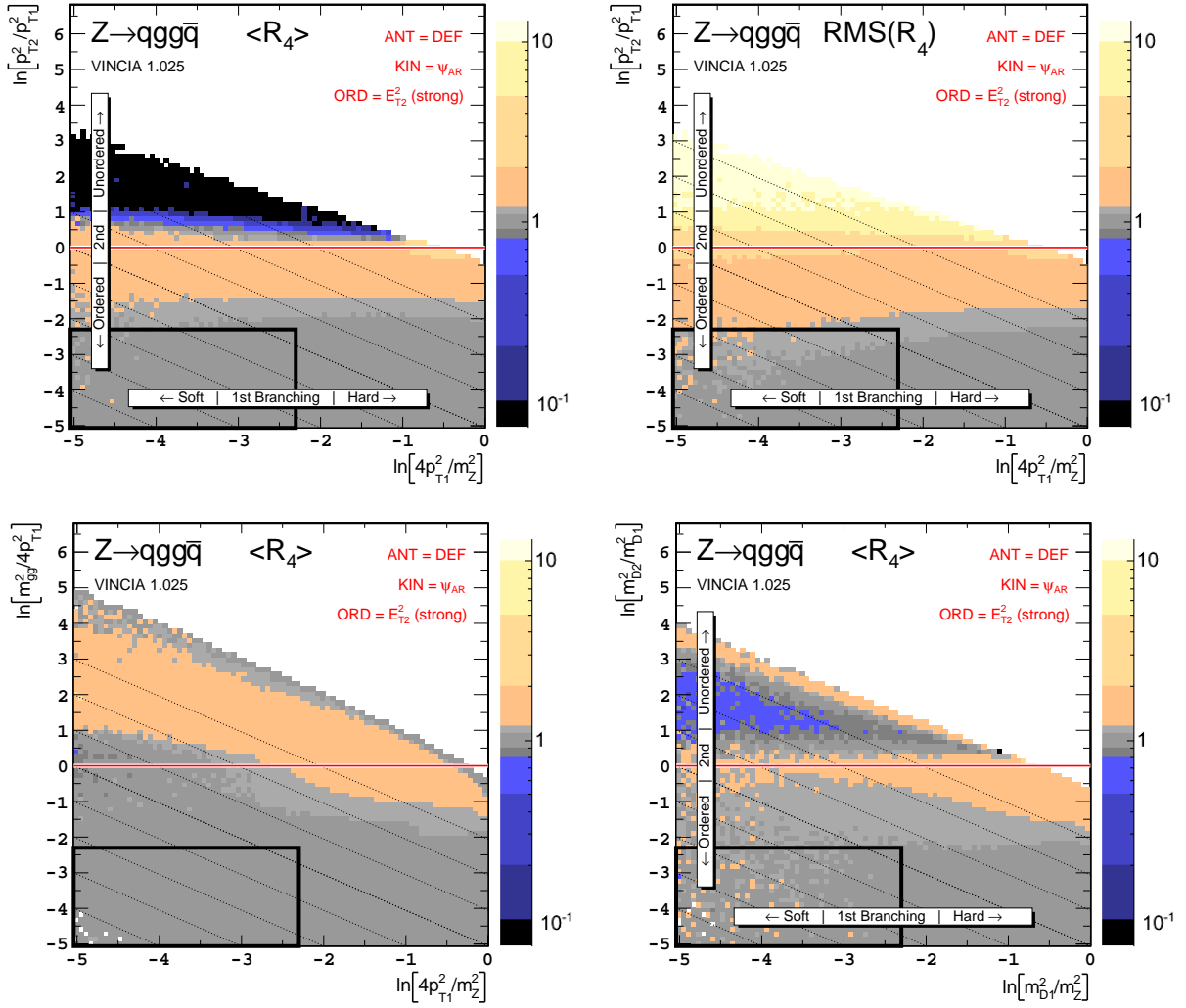


Figure 31: Angular-Ordered antenna approximation compared to 2nd order QCD matrix elements, using VINCIA's modified angular ordering,  $V_S$ , which is explicitly sensitive to soft and collinear emissions. The overall picture is quite similar to that for the HERWIG++ definition of angular-ordering.

## Smooth Transverse-Momentum Ordering (VINCIA)

$$p_{\perp}^2 = \frac{s_{ij}s_{jk}}{s}$$

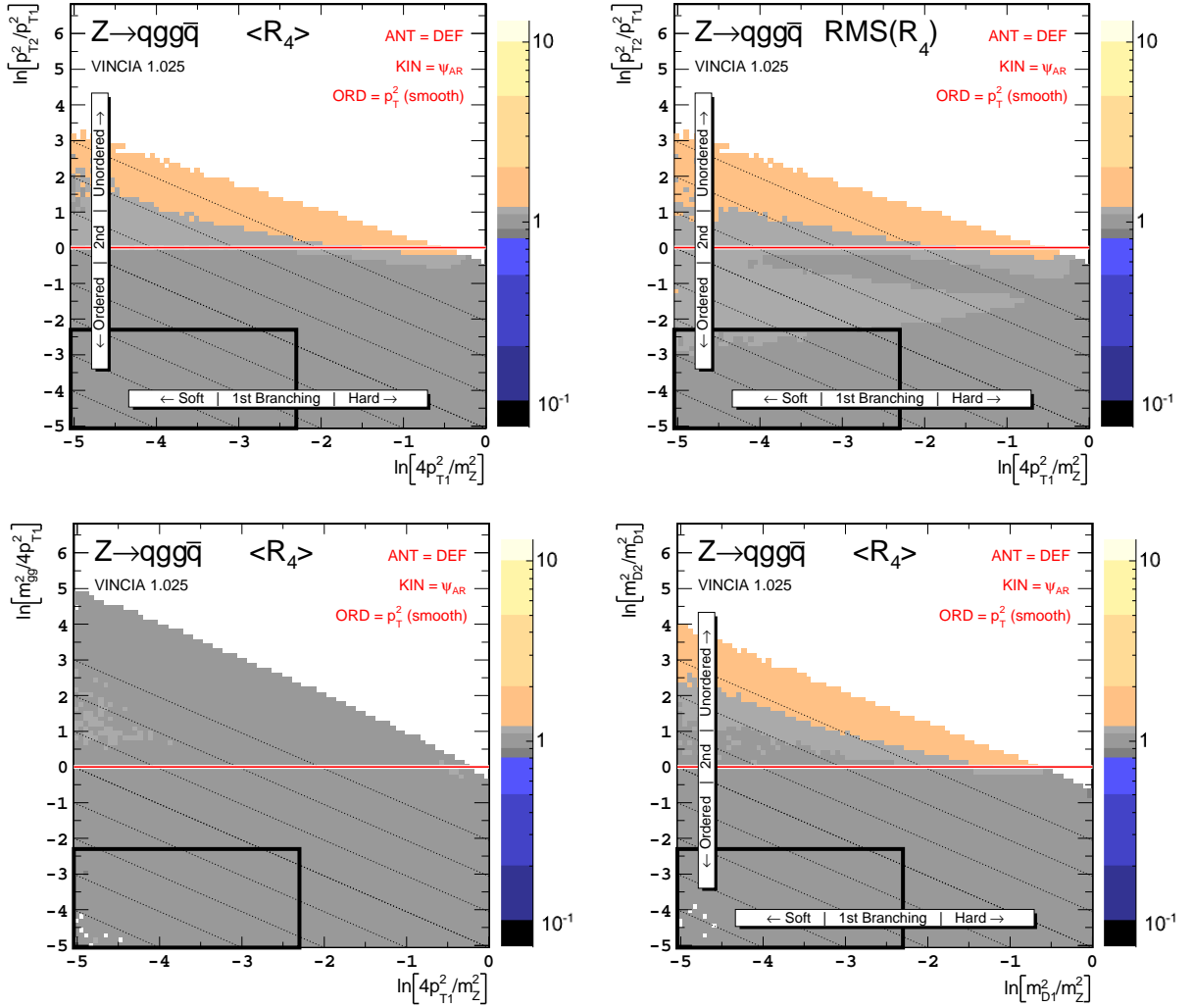


Figure 32: Transverse-momentum-ordered antenna approximation compared to 2nd order QCD matrix elements, using ARIADNE's definition of  $p_{\perp}$  and VINCIA's smooth suppression factor instead of the usual strong ordering condition. This corresponds to the default in VINCIA without matching. (Note: by default, matching to  $Z \rightarrow 4$  is on in VINCIA, over all of phase space, and hence these ratios are all equal unity).

## Smooth Mass-Ordering (VINCIA)

$$m_D^2 = 2\min(s_{ij}, s_{jk})$$

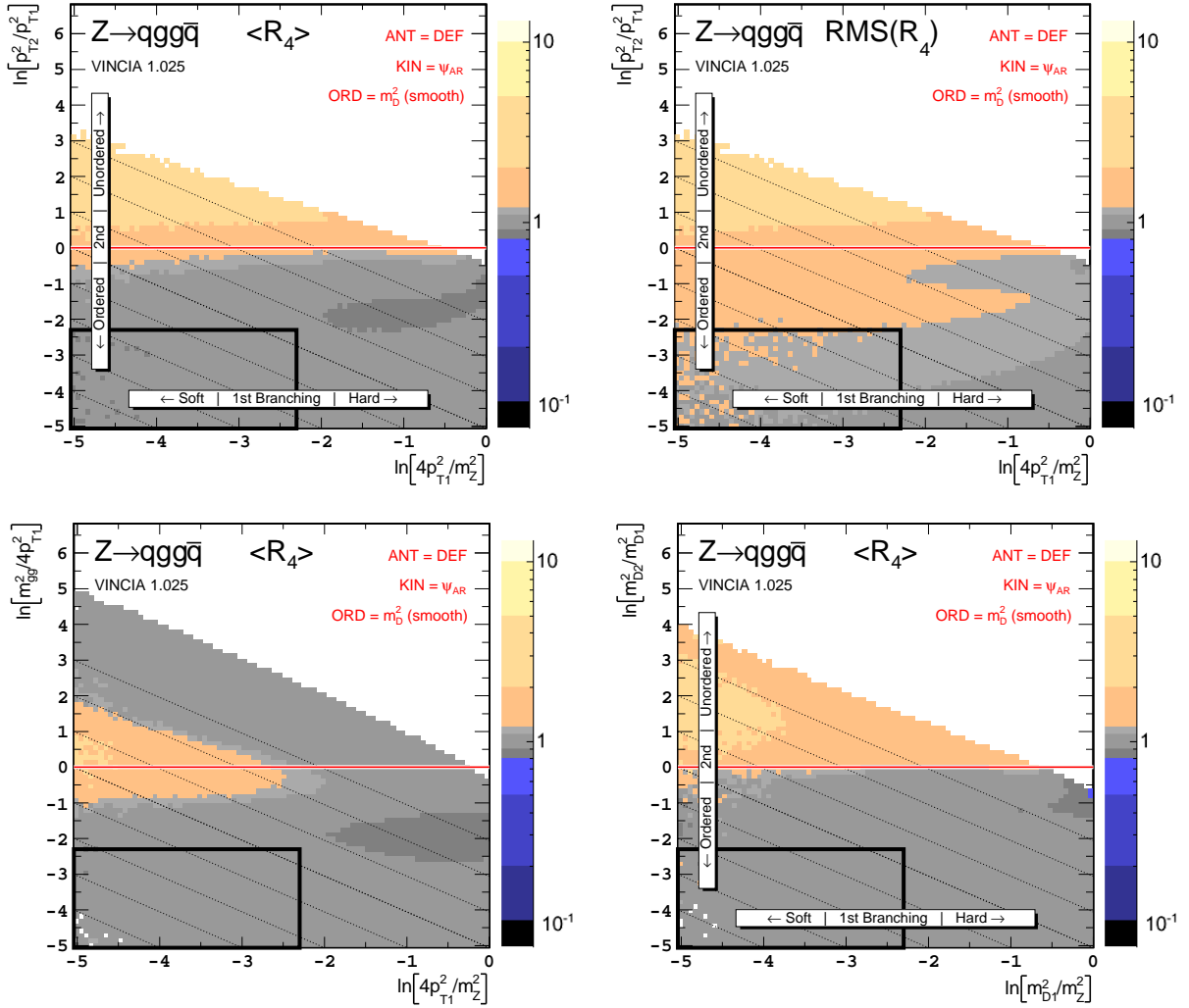


Figure 33: Mass-ordered antenna approximation compared to 2nd order QCD matrix elements, using VINCIA's definition of  $M_D$  applied as a smooth suppression factor instead of the usual strong ordering condition. Although the dead zone has been removed without introducing a catastrophic over-counting, the results are less impressive than for  $p_\perp$ -ordering. Note: the default in VINCIA is therefore to apply the smooth suppression factor in  $p_\perp$  regardless of the actual choice of evolution variable.



## References

- [1] J. Butterworth, J. R. Ellis, and A. Raklev, *JHEP* **0705**, 033 (2007), hep-ph/0702150.
- [2] A. Abdesselam *et al.*, (2010), arXiv:1012.5412.
- [3] A. Buckley *et al.*, (2011), arXiv:1101.2599.
- [4] M. L. Mangano, M. Moretti, F. Piccinini, and M. Treccani, *JHEP* **01**, 013 (2007), hep-ph/0611129.
- [5] S. Höche *et al.*, (2006), hep-ph/0602031.
- [6] S. Catani, F. Krauss, R. Kuhn, and B. R. Webber, *JHEP* **11**, 063 (2001), hep-ph/0109231.
- [7] T. Gleisberg *et al.*, *JHEP* **02**, 007 (2009), arXiv:0811.4622.
- [8] M. L. Mangano, M. Moretti, F. Piccinini, R. Pittau, and A. D. Polosa, *JHEP* **07**, 001 (2003), hep-ph/0206293.
- [9] E. Boos *et al.*, (2001), hep-ph/0109068.
- [10] J. Alwall *et al.*, *Comput. Phys. Commun.* **176**, 300 (2007), hep-ph/0609017.
- [11] T. Sjöstrand, S. Mrenna, and P. Z. Skands, *JHEP* **05**, 026 (2006), hep-ph/0603175.
- [12] G. Corcella *et al.*, *JHEP* **01**, 010 (2001), hep-ph/0011363.
- [13] L. Lönnblad, *JHEP* **05**, 046 (2002), hep-ph/0112284.
- [14] N. Lavesson and L. Lönnblad, *JHEP* **07**, 054 (2005), hep-ph/0503293.
- [15] G. Gustafson, *Phys. Lett.* **B175**, 453 (1986).
- [16] G. Gustafson and U. Pettersson, *Nucl. Phys.* **B306**, 746 (1988).
- [17] L. Lönnblad, *Comput. Phys. Commun.* **71**, 15 (1992).
- [18] S. Mrenna and P. Richardson, *JHEP* **05**, 040 (2004), hep-ph/0312274.
- [19] F. Maltoni and T. Stelzer, *JHEP* **02**, 027 (2003), hep-ph/0208156.
- [20] M. H. Seymour, *Nucl. Phys.* **B436**, 443 (1995), hep-ph/9410244.
- [21] M. H. Seymour, *Comp. Phys. Commun.* **90**, 95 (1995), hep-ph/9410414.
- [22] S. Frixione and B. R. Webber, *JHEP* **06**, 029 (2002), hep-ph/0204244.
- [23] S. Schumann and F. Krauss, *JHEP* **03**, 038 (2008), arXiv:0709.1027.
- [24] M. Dinsdale, M. Ternick, and S. Weinzierl, *Phys. Rev.* **D76**, 094003 (2007), arXiv:0709.1026.
- [25] S. Catani and M. H. Seymour, *Nucl. Phys.* **B485**, 291 (1997), hep-ph/9605323.

- [26] K. Hamilton and P. Nason, *JHEP* **1006**, 039 (2010), arXiv:1004.1764.
- [27] L. G. Almeida, S. J. Lee, G. Perez, G. Sterman, and I. Sung, *Phys. Rev.* **D82**, 054034 (2010), arXiv:1006.2035.
- [28] M. Bengtsson and T. Sjöstrand, *Nucl. Phys.* **B289**, 810 (1987).
- [29] M. Bengtsson and T. Sjöstrand, *Phys. Lett.* **B185**, 435 (1987).
- [30] S. Frixione, P. Nason, and C. Oleari, *JHEP* **11**, 070 (2007), arXiv:0709.2092.
- [31] Z. Nagy and D. E. Soper, (2006), hep-ph/0601021.
- [32] J.-C. Winter and F. Krauss, *JHEP* **07**, 040 (2008), arXiv:0712.3913.
- [33] W. T. Giele, D. A. Kosower, and P. Z. Skands, *Phys. Rev.* **D78**, 014026 (2008), arXiv:0707.3652.
- [34] P. Skands and S. Weinzierl, (2009), arXiv:0903.2150.
- [35] T. Kinoshita, *J. Math. Phys.* **3**, 650 (1962).
- [36] T. D. Lee and M. Nauenberg, *Phys. Rev.* **133**, B1549 (1964).
- [37] A. Gehrmann-De Ridder, T. Gehrmann, and E. W. N. Glover, *JHEP* **09**, 056 (2005), arXiv:hep-ph/0505111.
- [38] G. Altarelli and G. Parisi, *Nucl. Phys.* **B126**, 298 (1977).
- [39] T. Sjöstrand, S. Mrenna, and P. Z. Skands, *Comput. Phys. Commun.* **178**, 852 (2008), arXiv:0710.3820 [hep-ph].
- [40] M. Bähr *et al.*, *Eur. Phys. J.* **C58**, 639 (2008), arXiv:0803.0883.
- [41] G. Marchesini and B. R. Webber, *Nucl. Phys.* **B238**, 1 (1984).
- [42] A. J. Larkoski and M. E. Peskin, *Phys. Rev.* **D81**, 054010 (2010), arXiv:0908.2450.
- [43] Z. Nagy and D. E. Soper, *JHEP* **09**, 114 (2007), arXiv:0706.0017.
- [44] NLO Multileg Working Group, Z. Bern *et al.*, (2008), arXiv:0803.0494.
- [45] S. Catani and M. H. Seymour, *Phys. Lett.* **B378**, 287 (1996), hep-ph/9602277.
- [46] Z. Nagy and D. E. Soper, *JHEP* **10**, 024 (2005), hep-ph/0503053.
- [47] T. Sjöstrand and P. Z. Skands, *Eur. Phys. J.* **C39**, 129 (2005), hep-ph/0408302.
- [48] D. A. Kosower, *Phys. Rev.* **D71**, 045016 (2005), hep-ph/0311272.
- [49] A. Gehrmann-De Ridder, T. Gehrmann, and G. Heinrich, *Nucl. Phys.* **B682**, 265 (2004), hep-ph/0311276.
- [50] Y. Dokshitzer and G. Marchesini, *JHEP* **0903**, 117 (2009), arXiv:0809.1749.
- [51] R. Kleiss, W. J. Stirling, and S. D. Ellis, *Comput. Phys. Commun.* **40**, 359 (1986).

- [52] J. Alwall *et al.*, JHEP **09**, 028 (2007), arXiv:0706.2334.
- [53] H. Murayama, I. Watanabe, and K. Hagiwara, (1992), KEK-91-11.
- [54] S. Catani, B. Webber, and G. Marchesini, Nucl.Phys. **B349**, 635 (1991).
- [55] B. Andersson, G. Gustafson, and C. Sjögren, Nucl. Phys. **B380**, 391 (1992).
- [56] A. Gehrmann-de Ridder, M. Ritzmann, and P. Skands, A study of quark mass effects in antenna showers, in preparation, 2011.
- [57] F. A. Berends and W. T. Giele, Nucl. Phys. **B313**, 595 (1989).
- [58] P. Eden, JHEP **9809**, 015 (1998), hep-ph/9805228.
- [59] S. Frixione, P. Nason, and B. R. Webber, JHEP **08**, 007 (2003), hep-ph/0305252.
- [60] S. Frixione and B. R. Webber, (2008), arXiv:0812.0770.
- [61] N. Lavesson and L. Lönnblad, JHEP **0812**, 070 (2008), arXiv:0811.2912.
- [62] L3 Collaboration, P. Achard *et al.*, Phys. Rept. **399**, 71 (2004), arXiv:hep-ex/0406049.
- [63] ALEPH, A. Heister *et al.*, Eur. Phys. J. **C35**, 457 (2004).
- [64] M. Cacciari and G. P. Salam, Phys. Lett. **B641**, 57 (2006), hep-ph/0512210, <http://www.lpthe.jussieu.fr/~salam/fastjet/>.
- [65] M. Dobbs and J. B. Hansen, Comput. Phys. Commun. **134**, 41 (2001).
- [66] A. Buckley *et al.*, (2010), arXiv:1003.0694.
- [67] A. Buckley, H. Hoeth, H. Lacker, H. Schulz, and J. E. von Seggern, Eur.Phys.J. **C65**, 331 (2010), arXiv:0907.2973.
- [68] G. Lafferty, P. Reeves, and M. Whalley, J.Phys.G **G21**, A1 (1995).